DOCTORAL THESIS

Anna KULIŚ-KAPUŚCIŃSKA

Characterization of surface properties of low dimensional zinc oxide ZnO nanostructures for potential microelectronics application

FACULTY:
AUTOMATIC CONTROL, ELECTRONICS AND COMPUTER SCIENCE

FIELD:
ENGINEERING AND TECHNICAL SCIENCES

DISCIPLINE:
AUTOMATION, ELECTRONIC, ELECTRICAL ENGINEERING AND SPACE TECHNOLOGIES

SUPERVISOR:
dr hab. inż. Monika Kwoka, prof. PŚ

Gliwice 2023

Acknowledgements

This work was partially financed by the research grant of National Science Centre, Poland - OPUS 11, No. 2016/21/B/ST7/02244.

I would like to express my deepest appreciation to my supervisor, **Prof. Monika Kwoka**, for many years of her scientific care, unceasing support and invaluable commitment to the development of my scientific career, as well as for her openness, understanding and the opportunity to complete my doctoral thesis in the Department of Cybernetics, Nanotechnology and Data Processing at the Silesian University of Technology, Gliwice, Poland. My thesis and the research behind it would not have been possible without her helpful advice, many hours of interesting and knowledge-related conversations, heartfelt patience and exacting attention to detail.

I am most thankful to **Prof. Jacek Szuber**, who has always provided his unflagging support, invaluable assistance and useful tips during my scientific research, and followed my scientific career with keen interest – with true kindness and openness.

My thanks go to **Prof. Jacek Łęski** for his support and guidance in various aspects of my doctoral studies and scientific work in the Department of Cybernetics, Nanotechnology and Data Processing at the Silesian University of Technology, Gliwice, Poland.

I would like to thank my coordinators during my internship in Dresden – **Dr Nadia Licciardello, Dr Massimo Sgarzi** and **Prof. Gianaurelio Cuniberti** – for giving me a warm welcome at the new place, introducing me to the operation of the Chair of Materials Science and Nanotechnology, for the opportunity to learn new methods, to work in the laboratory and to have a wonderful time. Their enthusiasm and expertise have been an inspiration and have kept my work on track since our first encounter.

It is with true pleasure that I acknowledge the contributions of my **colleagues** from the Silesian University of Technology in Gliwice and Technical University in Dresden, their support, friendly atmosphere during work and beyond, kindness and a powerful incentive to get my thesis done.

Last but not least, I want to express my profound gratitude to my **husband**, **parents**, **sisters** and all other **family** members; this journey would not have been possible without their dedicated support. I very much appreciate their love shown every day, understanding, patience, help, their believing in me and their unassuming, yet very much felt presence in my life. In addition, I would like to thank my **aunt Teresa Czogała-Koczy** for her linguistic help and guidance in writing the thesis.

Abstract

The aim of the doctoral thesis was to determine the basic surface properties of selected zinc oxide ZnO nanostructures in terms of their potential application in microelectronics.

The studied objects were low dimensional: two dimensional ZnO nanostructures in the form of nanolayers deposited on a silicon (Si) substrate by Direct Current Magnetron Sputtering (DCMS), and one dimensional ZnO nanostructures in the form of nanowires, fabricated on a silicon (Si) substrate by Physical Vapour Deposition (PVD).

The goal of the experiments was to characterize the surface properties of the above-mentioned ZnO nanostructures in view of their application in microelectronics, especially for the protection of the environment, health and even human life, with nanostructured ZnO thin films verified as an active material in photocatalytic water purification; ZnO nanowires were used as a sensor material in a toxic gas sensor based on the surface photovoltage effect (SPV).

Series of different studies using complementary research methods in a proper order were carried out. Owing to the usage of Atomic Force Microscope (AFM) and Scanning Electron Microscope (SEM), it was possible to obtain the key information on the surface morphology of the objects under study, including the structure of the samples, grain size, and the changes occurring on their surface before and after subsequent application experiments. By means of the X-ray Photoelectron Spectroscopy (XPS) the key information could be obtained about the surface chemical properties of the studied objects, including their surface non-stoichiometry, and the type of chemical bonds, as well as the presence of surface impurities, mainly carbon (C), resulting from the uncontrolled contact of the used selected ZnO nanostructures with impurities present in the atmosphere or water. Moreover, in case of ZnO nanowires, the behaviour of C impurities could be determined, including, in particular, the possibility of their removal by thermal desorption in very high vacuum by using a combination of Thermal Desorption Spectroscopy (TDS) combined with XPS studies.

The purpose of the work was to identify the possible applications of DCMS nanostructured ZnO thin films as photocatalytic material for water purification (using methylene blue) and ZnO nanowires as the sensing material for toxic gas sensors, based on the effect of surface photovoltage (SPV) for the detection of the dangerous toxic gas nitrogen dioxide NO_2.

The information resulting from the doctoral thesis is crucial, as on the one hand the basic surface properties of the selected ZnO nanostructures were obtained, which is of great cognitive importance, and on the other hand, the application opportunities of the objects in microelectronics were confirmed, including the potential application in water treatment for the photocatalytic process (nanostructured ZnO thin films) and for toxic gas detection (ZnO nanowires).

Streszczenie

Przedmiotem pracy doktorskiej było określenie podstawowych właściwości powierzchniowych wybranych nanostruktur tlenku cynku (ZnO) w aspekcie ich potencjalnego zastosowania w mikroelektronice.

Obiektem badań były niskowymiarowe: dwuwymiarowe nanostruktury ZnO w formie nanowarstw osadzonych na podłożu krzemowym (Si) metodą stałoprądowego reaktywnego rozpylania jonowego (DCMS) oraz jednowymiarowe nanostruktury ZnO w formie nanodrutów wytworzonych na podłożu krzemowym (Si) metodą fizycznego osadzania z fazy pary (VPD).

Podstawowym celem przeprowadzonych badań była charakteryzacja właściwości powierzchniowych w/w nanostruktur tlenku cynku (ZnO) w aspekcie ich potencjalnego zastosowania w mikroelektronice, w tym zwłaszcza w aspekcie ochrony środowiska naturalnego, zdrowia, a nawet życia ludzkiego, przy czym nanowarstwy ZnO sprawdzono jako materiał czynny w procesie fotokatalitycznego oczyszczania wód, natomiast nanodruty ZnO wykorzystano jako materiał sensorowy w czujniku gazów toksycznych na bazie efektu fotonapięcia powierzchniowego (SPV).

Do realizacji zamierzonego celu wykonano szereg badań doświadczalnych właściwości powierzchniowych w/w nanostruktur tlenku cynku (ZnO), z wykorzystaniem komplementarnych metod badawczych w ściśle określonej sekwencji kolejności. Przez wykorzystanie metod Mikroskopii Sił Atomowych (AFM) oraz Skaningowej Mikroskopii Elektronowej (SEM) udało się uzyskać kluczowe informacje dotyczące powierzchniowej morfologii badanych obiektów, w tym struktury próbek, wielkości ziaren, zmian występujących na ich powierzchni przed i po kolejnych eksperymentach aplikacyjnych. Z kolei metodą Rentgenowskiej Spektroskopii Fotoelektronowej (XPS) udało się uzyskać kluczowe informacje o powierzchniowych właściwościach chemicznych badanych obiektów, w tym o ich powierzchniowej niestechiometrii, oraz rodzaju wiązań chemicznych, a także obecności zanieczyszczeń powierzchniowych głównie węglowych (C), będących wynikiem niekontrolowanego kontaktu wykorzystywanych wybranych nanostruktur ZnO z zanieczyszczeniami obecnymi w atmosferze lub w wodzie. Ponadto, w przypadku nanodrutów ZnO, udało określić zachowanie się powierzchniowych zanieczyszczeń węglowych, w tym zwłaszcza możliwość ich usunięcia w procesie desorpcji termicznej w bardzo wysokiej próżni, przez zastosowanie kombinacji metody Spektroskopii Desorpcji Termicznej (TDS), w połączeniu z badaniami metodą XPS.

Zgodnie z celem i przedmiotem pracy, sprawdzono możliwości wykorzystania nanowarstw DCMS ZnO jako materiału fotokatalitycznego do rozkładu zanieczyszczeń (wodnego roztworu błękitu metylenowego) w wodzie w procesie jej uzdatniania, a nanodrutów ZnO jako materiału sensorowego w czujniku gazów toksycznych na bazie efektu fotonapięcia powierzchniowego (SPV) do detekcji groźnego gazu toksycznego - dwutlenku azotu NO_2.

Uzyskane w ramach realizacji pracy doktorskiej informacje są kluczowe, gdyż z jednej strony udało się określić podstawowe właściwości powierzchniowe wybranych nanostruktur tlenku cynku (ZnO), co ma znaczenie poznawcze, a z drugiej – udało się potwierdzić możliwości aplikacyjne tych obiektów w mikroelektronice, w tym ich potencjalne zastosowanie do uzdatniania wody w procesie fotokatalitycznym (nanowarstwy ZnO) oraz do detekcji gazów toksycznych (nanodruty ZnO).

CONTENT

Abbreviation	Meaning
AES	Auger Electron Spectroscopy
AFM	Atomic Force Microscope
AOP	Advanced Oxidation Process
BG	Band Gap
BSE	Backscattered Electrons
CHA	Concentric Hemispherical Analyzer
CVD	Chemical Vapour Deposition
DCMS	Direct Current Magnetron Sputtering
DCS	Direct Current Sputtering
DPXPS	Depth Profiling X-ray Photoelectron Spectroscopy
EDX	Energy-Dispersive X-ray Spectroscopy
EM	Electron Microscopy
FE-SEM	Field-Emission Scanning Electron Microscope
HR SEM	High Resolution Scanning Electron Microscope
IMS	Ion Magnetron Sputtering
MB	Methylene Blue
MBE	Molecular Beam Epitaxy
MS	Mass Spectrometry
NPs	Nanoparticles
PC	Photocatalytic
PLD	Pulsed Laser Deposition
PVD	Physical Vapour Deposition
QDs	Quantum Dots
QMS	Quadrupole Mass Spectrometer
RFIS	Radio-Frequency Ion Sputtering
RGA	Residual Gas Analyzer
RIS	Reactive Ion Sputtering
RMS	Root Mean Square
RT	Room Temperature
SCL	Space Charge Layer
SE	Secondary Electrons
SEM	Scanning Electron Microscope
SPS	Surface Photoelectron Spectroscopy

SPV	Surface Photovoltage
STM	Scanning Tunneling Microscope
TCO	Transparent Conductive Oxide
TDS	Thermal Desorption Spectrometer
TEM	Transmission Electron Microscope
TFT	Thin Film Transistor
TPD	Temperature Programmed Desorption
UHV	Ultra-High Vacuum
UV	Ultraviolet
UV-Vis	Ultraviolet – Visible Light
VB	Valence Band
VDW	Van Der Waals
XPS	X-ray Photoelectron Spectroscopy

Chapter 1.
Motivation and scope

In the last decades there has been a general tendency to look for the potential applications of electronics materials in the solid state electronics in order to develop a novel generation of the specific micro- and nano- electronic devices. It makes it possible to decrease the size of the devices into nanoscale level while maintaining or even improving their properties and functionality [1].

A great and increasing interest, mainly in the last years, is focused on the transparent conductive oxides (TCO) because of their outstanding simultaneous optical and electronic properties, with respect to the commonly used elemental semiconductors of group IV (like Si and Ge), and compound semiconductors of group III-V (like GaAs and related compounds), as well as of group II-VI (like CdS and related compounds). TCO can be fabricated as n- and p-type conductors. Both their transparency and conductivity can be adjusted. Therefore, it opens up a wide range of energy-efficient optoelectronic circuits, and they have found wide applications in optoelectronic devices such as solar cells, displays, touch screens, interfaces and optoelectronic circuits, to name just a few [2].

Zinc oxide ZnO is one of the most popular semiconducting transparent conductive oxides. Being non-toxic and having a high chemical stability combined with the above-mentioned high transparency in over visible and near infrared region, and high electric conductivity compatible with standard electronics, it has attracted great interest because of its wide potential application in scientific or industrials areas. Among others, ZnO is used in photovoltaics, optoelectronics and environmental engineering [3,4].

In general, the above-mentioned basic specific properties of ZnO are strongly related to its dimensionality, which is absolutely crucial. This is because it determines compounds' purity and stoichiometry, forms of atomic structure and surface morphology, and related electronic as well as optical properties, which determine their potential application, especially with a view to the common modern tendency to downscale the electronic devices [5].

The main thesis of this work is that the selected low dimensional ZnO nanostructures having the controlled and precisely defined surface properties, mainly including surface chemistry and surface morphology, can have a wide potential practical application in microelectronics and environmental engineering.

The survey of literature (state-of-the art) on ZnO as the electronic material, with special emphasis on the low dimensional ZnO nanostructures, their basic properties, technology of their preparation, and finally their potential application is described in ***Chapter 2*****.**

In ***Chapter 3*** the aim and scope of own studies is described within this thesis.

Chapter 4 contains the description of fundamentals, apparatus and abilities of the selected analytical methods used in this work for the characterization of surface properties of low dimensional ZnO nanostructures.

In ***Chapter 5*** the details of technological procedures for the preparation of selected low dimensional ZnO nanostructures are described, together with the procedures for the characterization of their surface properties applied in these studies.

In ***Chapter 6*** the results of own studies of the surface properties of the nanostructured ZnO thin films and ZnO nanowires are described and discussed, with special emphasis on their atomic structure and surface morphology, as well as the surface chemistry including contaminations and surface bondings, combined with the residual gas interactions at their surfaces.

Chapter 7 contains the description of the results of own studies on the potential application of the nanostructured ZnO thin films in photocatalysis and water purification.

Chapter 8 contains the description of the results of own studies on the potential application of the ZnO nanowires as electrode material in SPV gas sensor device for NO_2 detection.

In ***Chapter 9*** a short summary and conclusions of the author's own studies and the obtained results are proposed, together with final remarks.

The main part of experimental results obtained within the author's own studies have already been published in the set of 4 original papers in JCR journals as listed below:

- Monika Kwoka, Barbara Lyson-Sypien, **Anna Kulis**, Monika Maslyk, Michal Adam Borysiewicz, Eliana Kaminska and Jacek Szuber ***Surface Properties of Nanostructured, Porous ZnO Thin Films Prepared by Direct Current Reactive Magnetron Sputtering***. Materials, 2018 11(1) 131; doi: 10.3390/ma11010131, IF: 3.601
- Monika Kwoka, **Anna Kulis-Kapuscinska**, Dario Zappa, Elisabetta Comini and Jacek Szuber ***Novel insight on the local surface properties of ZnO nanowires,*** Nanotechnology. 2020 31(46) 465705; doi: 10.1088/1361-6528/ab8dec, IF: 3.874
- **Anna Kulis-Kapuscinska**, Monika Kwoka, Michal Adam Borysiewicz, Tomasz Wojciechowski, Nadia Licciardello, Massimo Sgarzi and Gianaurelio Cuniberti ***Photocatalytic degradation of methylene blue at nanostructured ZnO thin films,*** Nanotechnology, 2023 34(15) 155702; doi: 10.1088/1361-6528/aca910, IF: 3.874
- **Anna Kulis-Kapuscinska**, Monika Kwoka, Jacek Szuber, Elisabetta Comini and Dario Zappa ***SPV gas sensing studies of ZnO nanowires in NO_2 atmosphere*** **(during submission)**.

and noted in Arabic digits cited in Bibliography within the Thesis as [40],[21],[41], respectively, whereas the last paper is cited as [72].

Chapter 2.
ZnO low dimensional nanostructures

2.1. ZnO as the electronic material

Zinc oxide (ZnO) was already known probably by ancient people, mainly as an ointment for the wound treatment or as paint. Furthermore, ZnO was used for example as ore to make brass, as a pigment or in the rubber, ceramic, drug industries, etc. [6]. As a semiconductor it was researched by scientists at the beginning of the 20th century. However, in the last twenty years a revival and rapid expansion of research on zinc oxide has been noticeable, taking into account its unique properties.

ZnO is one of the most important zinc compounds and belongs to the transparent conductive oxides (TCO) of a popular group of electronic materials.

In nature it exists in the form of rare mineral zincite which usually contains an amount of other elements like Mn and other impurities, which changes the color to yellow, brown or red [7].

It is possible to get three different crystalline structures of ZnO (as shown in Fig. 2.1.) like cubic zinc blende by epitaxial growth on substrate with cubic lattice structure, rocksalt by acting under high pressure (about 10GPa) or hexagonal wurtzite, which is the most frequently used structure due to its stability in ambient conditions. None of the aforementioned forms is characterized by inversion symmetry.

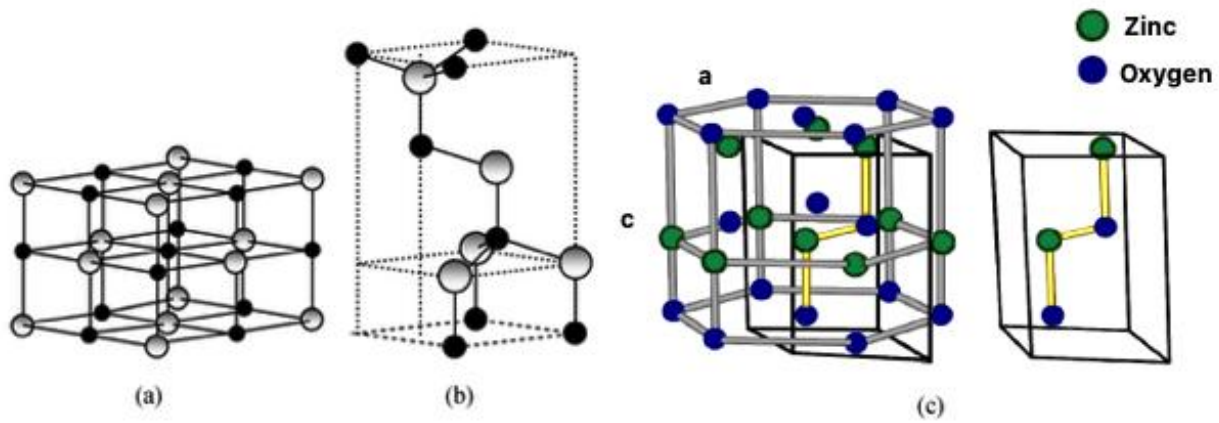

Fig. 2.1. Atomic structures of ZnO: (a) cubic rock salt, (b) cubic zinc blende [8] and (c) hexagonal wurtzite, where gray represents Zn and black O atoms, respectively.

The ZnO unit cell has a spatial group C4 6v (Schoenflies) or in a different notation P63mc (Hermann-Mauguin), where each anion is surrounded by four cations and vice versa, each cation is surrounded by four anions, placed in the corners of tetrahedral bonding configuration. In the ideal structure the ratio of two lattice parameters *a* and *c* is equal to 1.633, where the values *a* and *c* are approximately equal, respectively, to ~3.2495 Å and ~5.2062 Å. However, in the real occurrence, the structure deviates from that form and the ratio *c/a* has a smaller value [6,9]. The wurzite nanostructure can achieve different growth morphology like nanotubes, nanowires, nanobelts, nanoflowers, etc.

ZnO is a chemical compound of atoms of II and VI group. Most of them have covalent character with sp^3 bonding, but there are also largely ionic bondings – the electrostatic attraction between Zn^{2+} and O^{2-}, which increases the band gap and results in piezoelectric properties. As a result, an electrical charge appears on the crystallographic surface.

As mentioned before, zinc oxide is characterized by a wide band gap, which depends mainly on the carrier concentration – in case of 1018-1020 cm^{-3}, it is equal to around 3.37 eV. Three states (A, B, C) can be distinguished in the upper part of the valence band, obtained at the same Γ point, where k=0, created by spin-orbit and crystal-field splitting. These levels define the interval between the so-called valence band maxima and the lowest conduction band minima [10], as shown in Fig. 2.2.

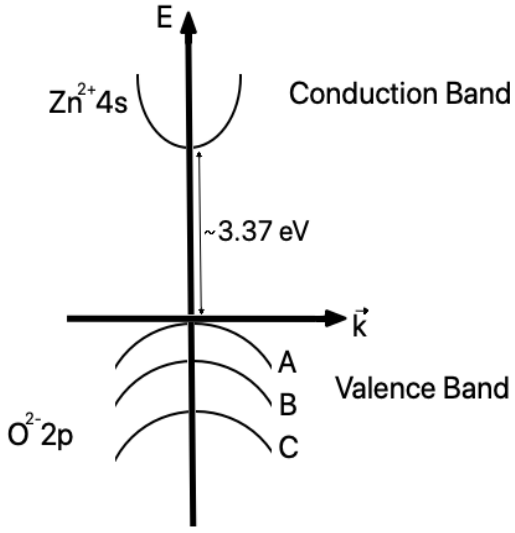

Fig. 2.2. Schematic diagram of the direct band gap in ZnO.

ZnO, by analogy to the most available TCOs, is an n-type semiconductor, because of conductivity by electrons, which has an influence on its electrical properties. Meanwhile, doping efficient p-type ZnO remains difficult and continues to be a challenge. The mobility of

electrons is high and varies with the temperature, i.e. the highest value equal to around 2000 $cm^2/V \cdot s$ is achieved at ~193.15 ºC [11].

The main unique properties of ZnO are listed below:

- direct wide band gap semiconductor - 3.37 eV,
- large binding energy (60meV),
- transparency in visible wavelength range,
- n-type conductivity related to O vacancies and Zn interstitial position – SCL,
- high electron mobility: 10^2 [$cm^2/V \cdot s$] - a similar level as for SnO_2,
- high electron conductivity ~ 10^3 [S/m],
- high optical transmission (IR-VIS) - 80 ÷ 90 % (depending on the forms),
- photocatalytic properties,
- large piezoelectric constants,
- relative stability in biological and chemical conditions,
- high chemical and thermal activity,
- strong oxidation capability,
- amphoteric oxide,
- thermochromic,
- low thermal expansion,
- low toxicity.

Because of the above listed unique properties, ZnO has attracted attention not only in basic science but also in the wide applications, including, among others, in optoelectronic devices, solar cells, flat-panel displays, gas sensors, especially toxic ones, photocatalysis, etc.

2.2. Low dimensional ZnO nanostructures – classification and basic properties

In general, all the ZnO nanostructures are mainly characterized by their extremely small sizes. Their classification is based on the number of dimensions which are in the nanoscale range of 1 ÷ 100 nm.

According to Richard W. Siegel [12], the following general types (forms) of nanostructures can be distinguished:

- zero-dimensional (0-D), e.g. particles, clusters,
- one-dimensional (1-D), e.g. nanowires, nanotubes, nanobelts, nanorods,
- two-dimensional (2-D), e.g. nanolayers, nanoplates, nanofilms,
- three-dimensional (3-D), e.g. nanoflowers,

which have respectively none, one, two or three diameters greater than 100 nm.

Fig. 2.3. below shows different possible types of material nanostructures with respect to the dimension and possible ways of obtaining, which are discussed in detail in subchapter 2.3.

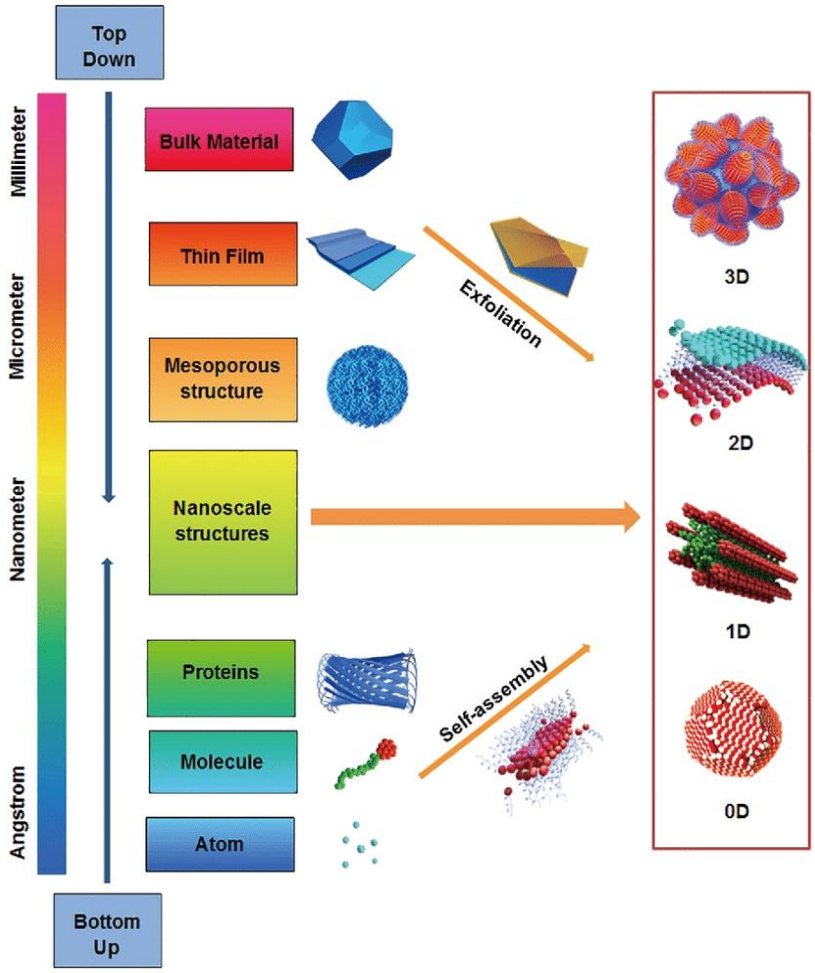

Fig. 2.3. Various types (forms) of material nanostructures [13].

In the last years, many innovative nanomaterials have been obtained. They often have unique properties like optical, photovoltaic, electrical, magnetic, catalytic properties, which makes it possible to use them in many fields of science, due to their small sizes, thickness, large surface-to-volume ratio, different shapes or morphology. In gas sensors with sensing parts built from nanomaterials, better sensitivity, stability or selectivity could be achieved.

Among these nanostructures, as shown in Fig. 2.4., ZnO is one of the most promising materials, due to the unique properties listed in Chapter 2.1. The additional beneficial effects of ZnO depend on the way of synthesis, shape, size, surface morphology or doping.

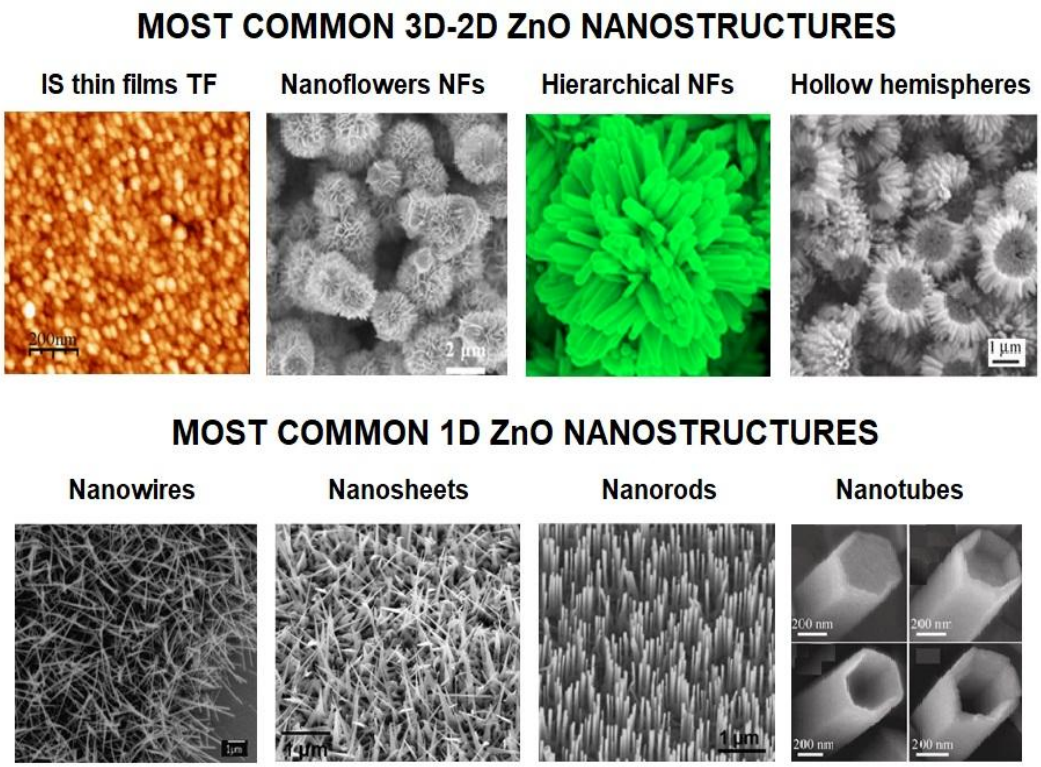

Fig. 2.4. Most common ZnO low dimensional nanostructures.

2.3. Technology of low dimensional ZnO nanostructures

ZnO is currently in the limelight, as it is widely used in many fields of science and technology, as well as in everyday life. Different technologies could be distinguished for obtaining nanostructures including thin films with controlled properties. Together with the reduction of size to nanoscale and many possible forms of structure, they make it possible to achieve, for example, the electrical or optoelectronic character, important in the production of sensing parts of gas sensors, transparent electrodes in photovoltaic cells, photodiodes, transistors, etc.

Taking into account the way in which the nanostructures (NSs) are produced, various categorizations of methods can be used. One of them, as shown in Fig. 2.5., is for example the division into:

- bottom-up – where nanostructures are prepared from single atoms or molecules, to grow crystal planes and structures. The controlled segregation is necessary to achieve desired nanomaterials. Typical techniques of such phenomena are sol-gel syntheses, the hydrothermal method, microwave assisted synthesis and microemulsion,
- top-bottom – as opposed to the previous method– fabrication, in which larger planes are etched out to remove crystal structure and realize nano-sized format. Ball milling, pyrolysis methods, laser ablation, vapour depositions can be provided as examples.

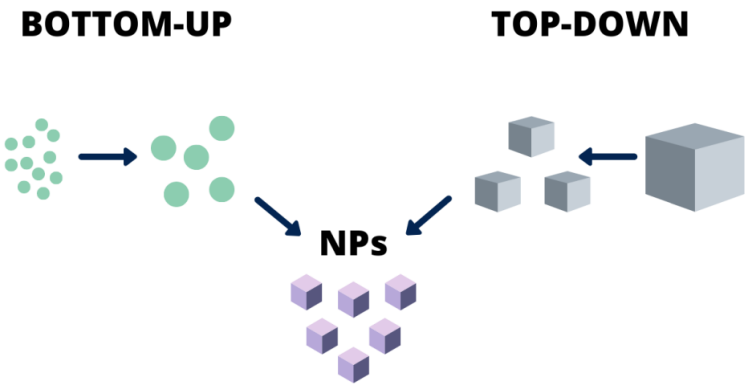

Fig. 2.5. Scheme of fabrication of NSs by bottom-up and top-down methods.

Another classification could be into natural, incidental or engineered [14]. In the first type, synthetization is a natural process in the environment. The second group includes nanomaterials which are obtained as by-products of industrial works. Engineered methods include experiments and specialized processes.

Generally, it is understood that manufacturing can be also divided into the three main categories: physical, chemical and biological. It is necessary to control the growth of nanostructures during a specific chosen process, to achieve proper size, shape and thickness. The methods of ZnO production are really numerous; in this chapter only selected ones are described and divided into two main groups, i.e. physical and chemical, as briefly described below.

Physical methods

These methods are based on deposition – condensation of molecules, atoms or ions generated in specific sources at the selected substrates. They make it possible to obtain high purity materials, intended among others for industrial electronics. The most common technological methods within this approach are briefly described below.

- **Molecular Beam Epitaxy (MBE)**

This method is based on the deposition of atomic flux of Zn from the effusion cell (source) at the properly prepared substrate maintained at the controlled temperature in the plasma (O/N) atmosphere, while the thickness of deposition of ZnO nanolayers is precisely controlled. A simplified scheme of such a process is shown in Fig. 2.6.

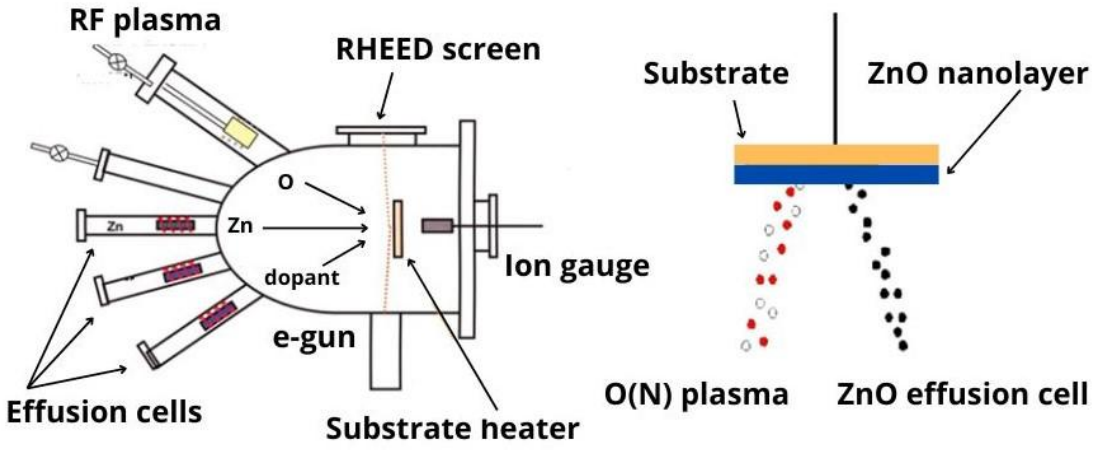

Fig. 2.6. Simplified scheme of the MBE method for the deposition of ZnO nanolayers.

- **Atomic Layer Deposition (ALD)**

This method is based on the deposition at the well prepared substrate maintained at the controlled temperature of flux of Zn from the decomposed precursor of di-ethyl-zinc (DEZ) and water vapour in the Ar gas flux, while the thickness of deposition of ZnO nanolayers is precisely controlled. A simplified scheme of such a process is shown in Fig. 2.7.

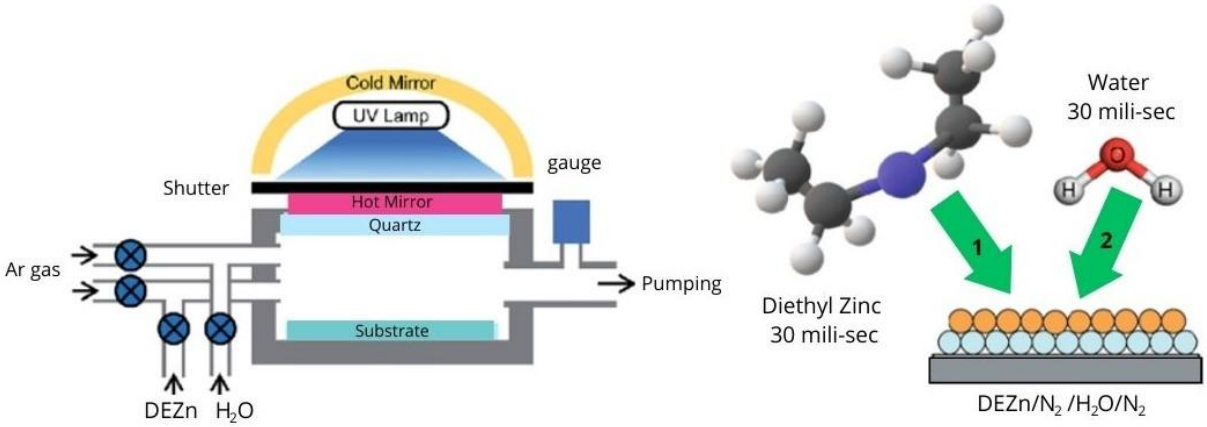

Fig. 2.7. Simplified scheme of the ALD method for the deposition of ZnO nanolayers.

- **Pulsed Laser Deposition (ALD)**

This method is based on the deposition at the properly prepared substrate maintained at the controlled temperature of flux of ZnO from the pure ZnO disc bombarded by the pulse KrF laser beam, while the thickness of deposition of ZnO nanolayers is precisely controlled. A simplified scheme of such a process is shown in Fig. 2.8.

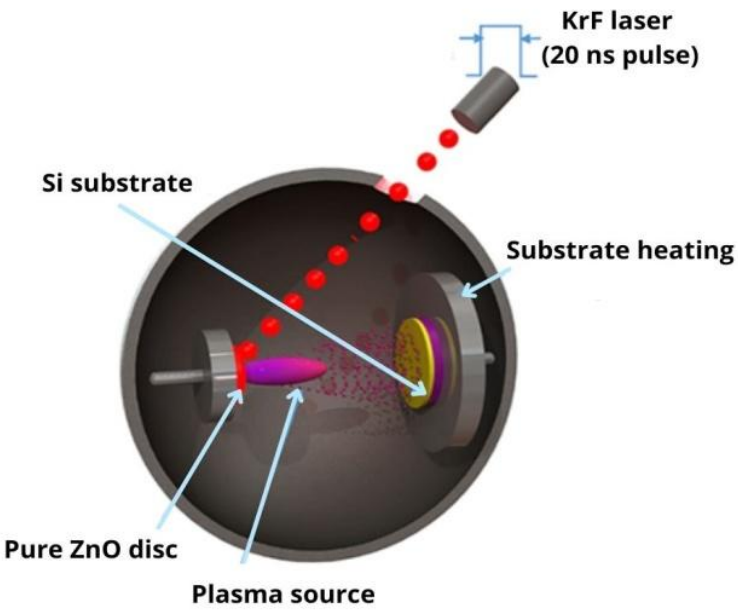

Fig. 2.8. Simplified scheme of the PLD method for the deposition of ZnO nanolayers.

- **Ion Sputtering Methods (ISM)**

This method is based on the deposition at the properly prepared substrate maintained at the controlled temperature of flux of Zn from the Zn target ionized by the Ar^+ ions generated by the ion source. The following four experimental approaches have been applied in this procedure:

- Direct Current Sputtering (DCS),
- Radio-Frequency Ion Sputtering (RFIS),
- Reactive Ion Sputtering (RIS),
- Magnetron Sputtering (MS),
- Combined Direct Current and Magnetron Sputtering (DCMS).

A simplified scheme of this last approach, most effective mainly in the deposition of nanostructured ZnO nanolayers, is shown in Fig. 2.9.

In this process, target coating of the basic atoms of the deposited material is bombarded by the Ar ions excited by the high voltage between cathode (generally behind the target) and anode, and finally the „sputtered" ions from the target in the plasma (O/N) atmosphere are deposited on a chosen substrate in the form of ZnO nanolayers.

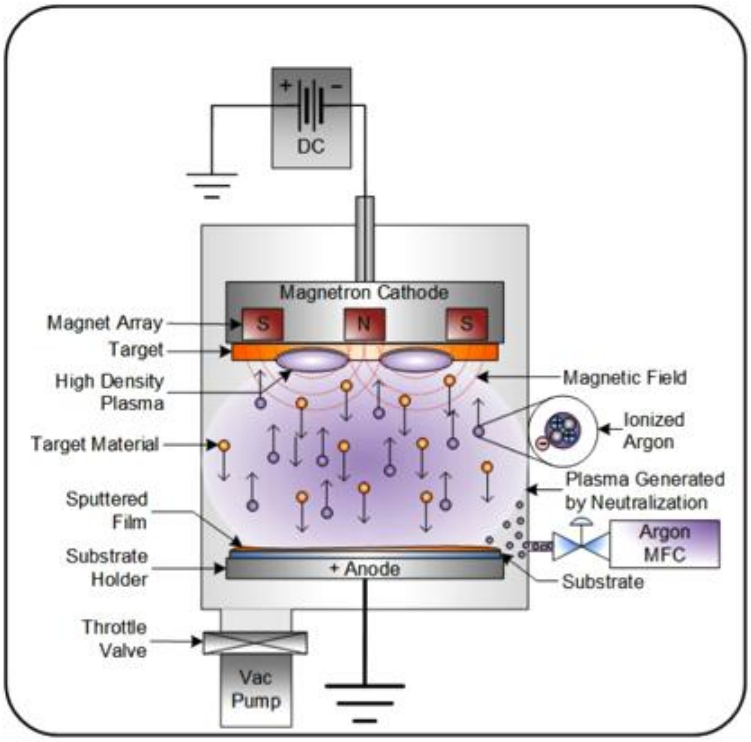

Fig. 2.9. Simplified scheme of the DCMS method for the deposition of ZnO nanolayers [15].

What is crucial, this method has been used for the preparation of porous nanostructured ZnO thin films (nanolayers) being the first type of samples used in the experimental studies presented in this thesis.

- **Combined Evaporation – Condensation Method (ECM)**

This method is based on the deposition of flux of ZnO from the pure ZnO powder evaporated from one part of the quartz tube inside the furnace and then condensed at the properly prepared substrate maintained at the controlled temperature. A simplified scheme of such a process for the deposition of ZnO nanowires is shown in Fig. 2.10.

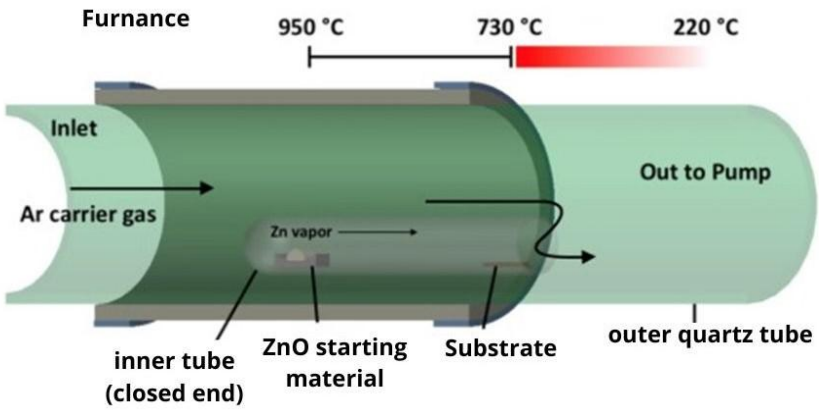

Fig. 2.10. Simplified scheme of the ECM method for the deposition of ZnO nanowires.

What is crucial, this method has been used for the preparation of ZnO nanowires deposited at Si substrate covered with Ag nanoparticles deposited by DCMS being the second type of samples used in our experimental studies presented in this thesis.

Chemical methods

These methods consist in the deposition at the surface of selected substrates of molecules, atoms or ions generated as a results of electrolytic, pyrolytic and optical decomposition of the reagent, as well as by the chemical reaction of reagents. They also make it possible to obtain high purity materials, intended among others for industrial electronics. The most common technological methods within this approach, based on the dry and wet chemical synthesis are briefly described below.

- **Chemical Vapour Deposition (CVD)**

  This method is based on three subsequent following steps [16]:

  - carefully chosen reagents in the form of gaseous fluxes are transported to the substrate,
  - specific chemical reactions of reagents with the surface substrate occur combined with their decomposition and subsequent surface diffusion at the controlled temperature,
  - by-products of all the reactions are removed by gas flowing through the chamber.

A simplified idea of the CVD process for the deposition of ZnO nanolayers is shown in Fig. 2.11.

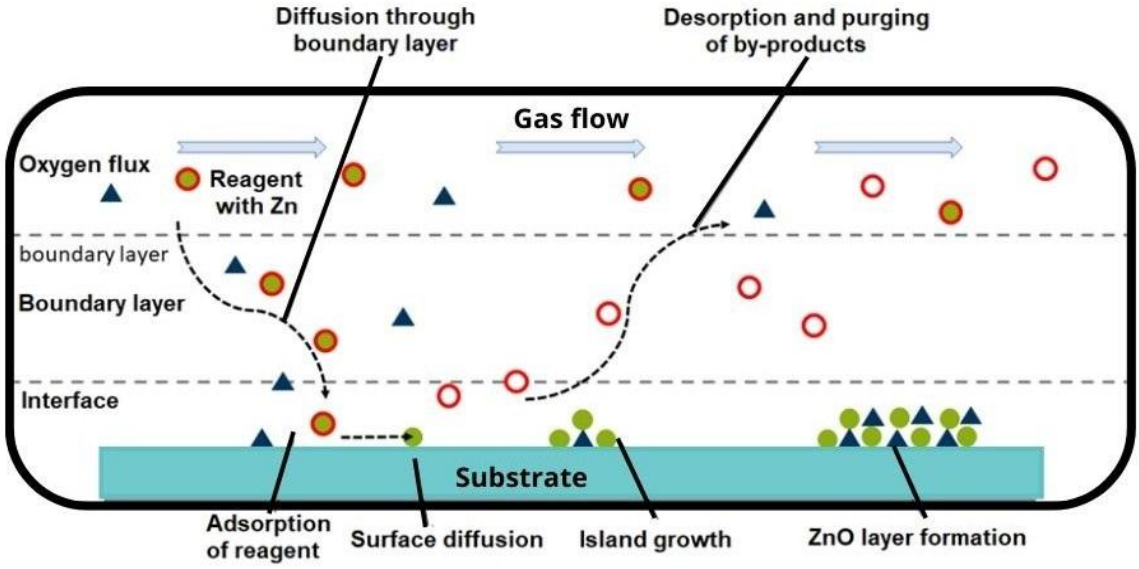

Fig. 2.11. Simplified idea of the CVD method for the deposition of ZnO nanolayers.

- **Sol-Gel Synthesis (SGS)**

This method is based on the hydrolysis and polycondensation reactions to achieve solid materials (gel) from small molecules or microparticles (sols). Depending on the precursor used, the colloidal method and polymeric (alkoxide) route can be distinguished.

In general, the precursors can hydrolize with water or alcohols, according to the formula (2.1) below:

$$M(OR)_n + nH_2O \rightarrow M(OH)_n + nROH\,, \qquad (2.1)$$

where: *M* is metal and *R* – alkyl group.

To achieve a sol form, a specific amount of acid must be added, and then sol is converted into gel by evaporation at a sufficiently high temperature. In general, thin films can be prepared on the chosen glass or metallic substrates with this procedure. Moreover, it should be noted that when the spin coating is additionally applied, the thin layers can be obtained; double-sided deposition is also possible when the dip-coating is additionally used. A simplified scheme and idea of the sol-gel process for the deposition of ZnO nanostructures is shown in Fig. 2.12.

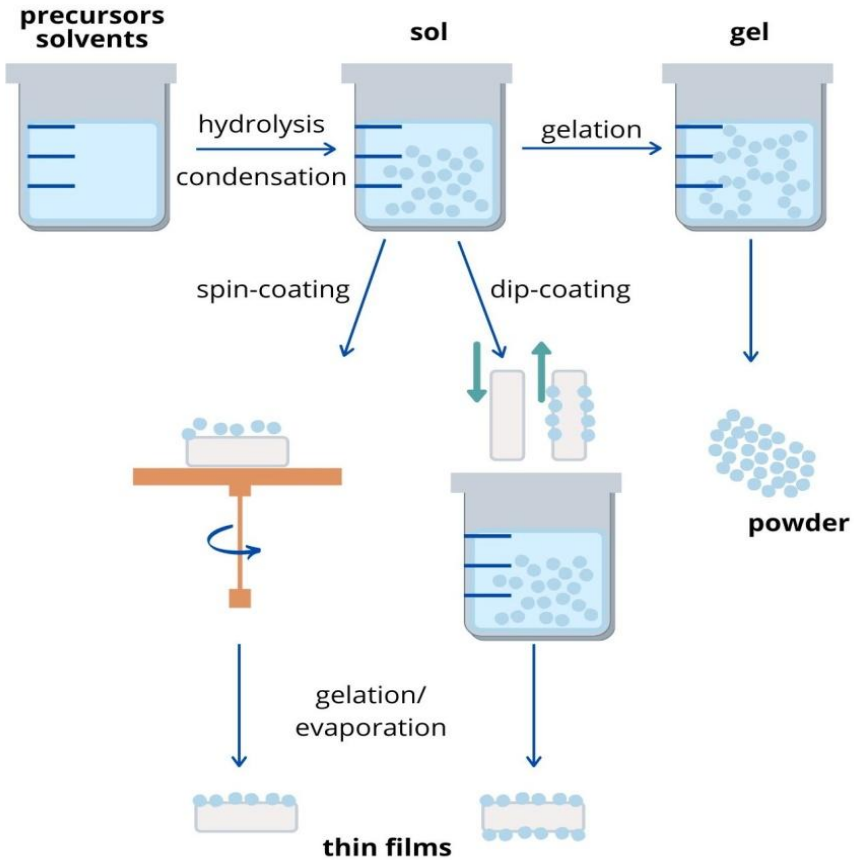

Fig. 2.12. Simplified scheme of the sol-gel technique for the deposition of ZnO nanostructures.

2.4. Potential application of low dimensional ZnO nanostructures

Due to the unique attractive chemical and physical properties and a set of characteristics, such as low toxicity, strong oxidation capability, relative stability in biological and chemical conditions, photocatalytic activity or thermal activity and low costs, ZnO as material has generated great interest and has been widely applied in many disciplines. Additionally, as it is characterized by ease of processing resulting in its diversity in terms of morphology, it can be applied in different ways [17,18]. ZnO nanostructures including nanoparticles of such a compound are well-suited for improving the quality and effectiveness of many electronic devices which play an important role in everyday life, as summarized in Fig. 2.13.

Fig. 2.13. List of most important applications of ZnO nanostructures.

Moreover, ZnO nanostructures can also have biomedical applications, including cosmetology, medicines or food packaging due to their antibacterial, antimicrobial, antioxidant and antitumor properties and UV protection efficiency [17]. What is more, they have good biocompatibility and low toxicity, hence they can be applied in bioimaging, drug or gene delivery. The overall amount of taken medicines can be reduced and thus the unwanted side effects can be minimized by using nanoparticles to target specific sites of cancer cells. ZnO particles in nano-scale are also adjusted in many therapies and diagnosis, e.g. as anticancer drugs.

Because Zn is one of the main components of various systems in the human body, it is present in various tissues, including brain, muscles, bones and takes part in important processes such as metabolism, neurogenesis or synthesis of proteins and nucleic acids. Thanks to ZnO nanoparticles, zinc is better absorbed by human body [19].

ZnO is also widely recognized as a sunscreen ingredient which protects the skin against UV radiation. That is why it is used as a cosmetic ingredient to protect the skin against sunburn or skin aging. In sunscreens, it protects the skin against UVA (320 ÷ 400 nm) and UVB (280 ÷ 320 nm).

ZnO nanomaterials applied in plastics, paints, tapes, pigments or rubber industry prevent the abrasion of the rubber composite, improve the quality, persistence and other properties of such products. Last but not least, ZnO plays a very important role in electronics and photovoltaics. In industry it is mostly included in optical and electrical equipment. Nowadays, a rapidly developing field of semiconductor physics and material science is transparent electronics.

As a TCO (transparent conductive oxide) with a wide, simple energy band gap, high electron mobility and transparency greater that 90% in a visible region it provides great opportunities for the use in optoelectronic or photovoltaic devices.

Among others, ZnO nanostructures are used in transistors and diodes, which results in better functionality, low-cost production and therefore, the use in other systems such as sensors. They are mainly implemented as channel materials, can be used in various forms and also with dopants or as dispersed particles in different solvents to improve their suitability for the chosen purposes.

Fig. 2.14. presents the schematic view of a ZnO based thin film transistor (TFT) with gold nanoparticles (AuNPs).

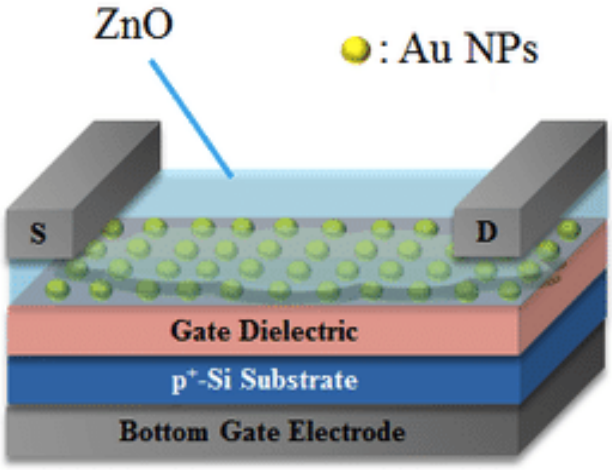

Fig. 2.14. A Cross section of ZnO based TF transistor with AuNPs between the dielectric and the channel layer [20].

Due to the appropriate metallic conductivity and optical transparency for visible light, ZnO is applied in solar cells as a layer or structure for transport of the electron charges.

It appears also as the anode material for lithium-ion batteries due to the higher theoretical capacity.

In recent years, ZnO has been widely recognized that by using it as a sensor materials in the form of nanostructures, gas detection performance can be significantly improved [21]. One of the groups of sensors uses a change in its surface conductivity, because it is related to the combined effect of adsorption and desorption of gases from the surrounding atmosphere at the surface of ZnO. This is why ZnO is one of the most popular oxide semiconductor gas (especially toxic and explosive one) sensing materials in the construction of gas sensor devices.

The gas sensing properties of various forms of ZnO strongly depend on their atomic structure and morphology, because these parameters strongly influence the gas response of such devices. They can be improved by large surface-to-volume ratio, which can be achieved by using low dimensional nanostructures, for example 1D nanobelts, nanowires, nanotubes. Moreover, also the porosity and non-stoichiometry have a significant impact on the development of sensors with very good sensitivity.

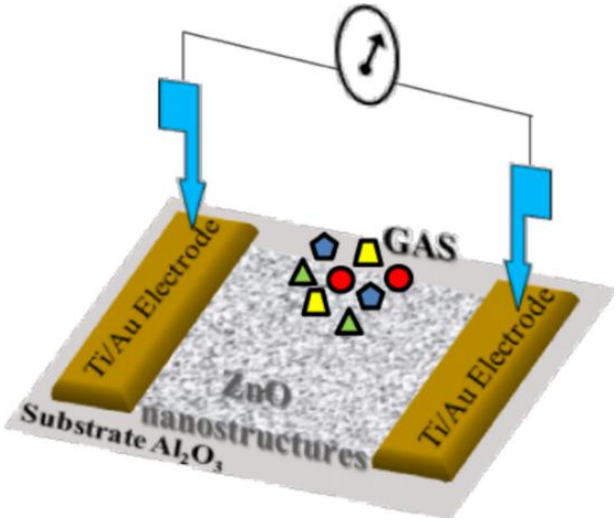

Fig. 2.15. Simplified scheme of a typical resistive type ZnO gas sensor [22].

What is more, ZnO nanomaterials are also becoming a promising material in environmental protection. Due to their good photocatalytic activity, wide band gap, low toxicity, chemical, thermal and photo-stability, they can be applied in waste water treatment for the degradation of organic pollutants. In general, a semiconductor photocatalyst absorbs light and is part of chemical transformation reactions. There are many advantages of the immobilized type of photocatalysis, e.g. no preparation process before application is needed, almost no mass transfer limitations, uniform distribution, continuous operations without final filtration, easy separation after reactions and possible reuse. Additionally, efficiency is increased by doping ZnO with different metals such as Ag, Au or Cu.

Chapter 3.
Aim and scope of own studies

As mentioned above, the main point of this doctoral thesis is that the selected low dimensional ZnO nanostructures with controlled and precisely defined surface properties, mainly including surface chemistry and surface morphology, can have a wide potential practical application in microelectronics and environmental engineering.

In order to verify this point, the aim of the studies proposed in this work was to perform a comparative analysis of surface properties of the selected low dimensional ZnO nanostructures including nanostructured ZnO thin films (in close cooperation with Łukasiewicz Research Network – Institute of Electron Technology, Warsaw, Poland) and quasi one-dimensional ZnO nanowires (in close cooperation with Brescia University, Italy), with special emphasis on their surface morphology, as well as the surface chemistry, by using the complementary surface analytical methods, such as:

- Atomic Force Microscopy (AFM) and Scanning Electron Microscopy (SEM) for the control of their surface morphology,
- X-ray Photoelectron Spectroscopy (XPS) for the control of their surface chemistry, including stoichiometry and surface contaminations, as well as surface bondings,
- Thermal Desorption Spectroscopy (TDS) for the control of the desorption process of surface contaminations of the residual gases from the sample under investigation.

Based on the performed experiments, a comparative analysis of surface chemistry and surface morphology of nanostructured ZnO thin films and ZnO nanowires has been proposed.

Moreover, on the basis of the above-mentioned information at the next step of our works the potential application of the nanostructured ZnO thin films in water purification based on the photocatalysis effect (in close cooperation with Technical University of Dresden, Germany), as well as the ZnO nanowires as the electrode material in SPV gas sensor device for NO_2 detection have additionally been verified and precisely described.

Chapter 4.
Analytical methods for surface characterization of ZnO nanostructures

In this chapter and in the subsequent subchapters, various analytical methods (measurement techniques) used in our experiments for surface characterization of ZnO nanostructures are described including their fundamentals, apparatus, abilities, as well as their advantages and limitations.

4.1. Atomic force microscopy (AFM)

In general, the Atomic Force Microscopy (AFM) makes it possible to obtain the images related to the morphology of solid surfaces. In this thesis the AFM method was mainly used for the control of surface morphology of the nanostructured ZnO thin films.

Fundamentals

In the AFM method a laser light beam is reflected from a flexible cantilever with a sharp tip scanned over the sample surface under scrutiny located at the XYZ piezo-scanner and measured by a quadrant photodiode system. A different interaction force can be seen versus distance graph based on the tip and sample surface relations. In general, two forces can be distinguished, which have an impact on the deflection of the cantilever, which is mainly related to the Van der Waals force appearing between the tip and sample surfaces (Fig. 4.1.).

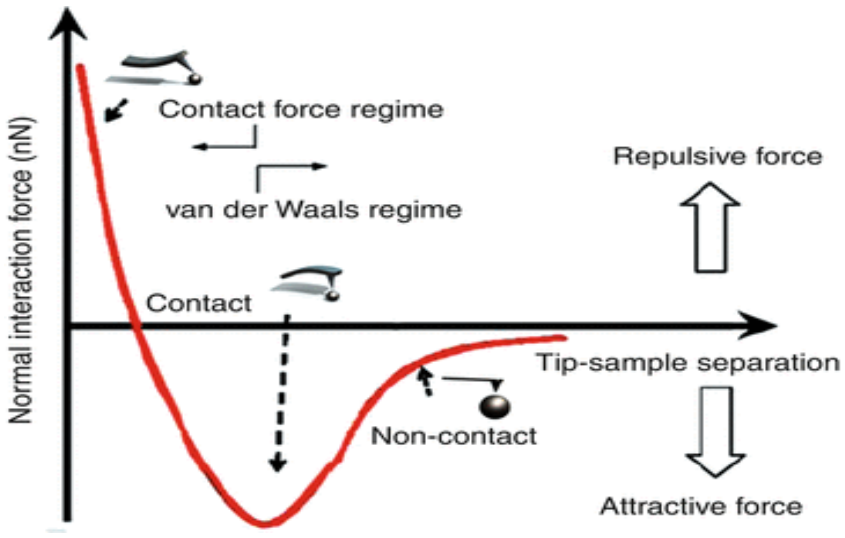

Fig. 4.1. Dependence of acting VDW forces on distance between the tip and sample surfaces [23].

It is caused by fluctuations in the charge density of atomic cores and the surrounding electrons. The value of the force is associated with the particular geometry of the objects, typically assumed to occur between single atoms; however, it also has an effect in the interaction of macroscopic objects. The second force that appears between charges of the particles or objects, is called a Coulomb force.

Depending on the range of those forces versus tip-sample distance or the type of surface to be tested, several modes of operations could be distinguished according to their characteristic features, which enlarges the research field. Basically, the following division can be made: static or dynamic (in line with the bending of the cantilever) and contact or non-contact (whether the tip has a direct physical contact with the surface or not) [24], which is presented in Fig. 4.2.

Besides those subdivisions, other deeper methods can be evaluated, such as those based on the analysis of the electrical properties, mechanical viscoelasticity, electric and magnetic fields or surface potential.

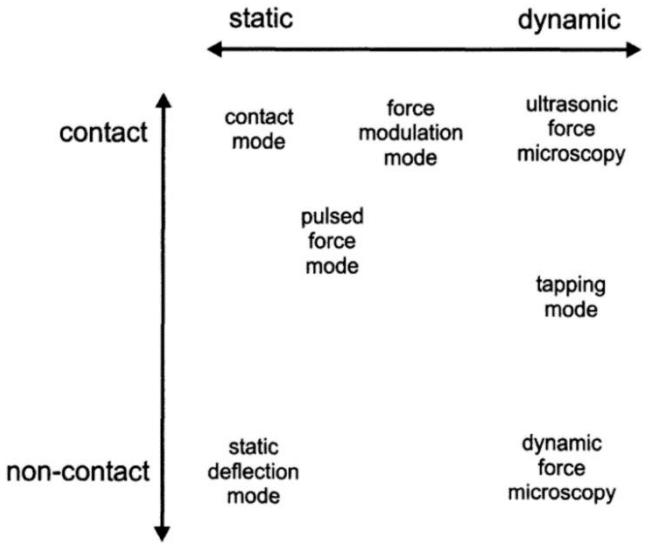

Fig. 4.2. General scheme of various AFM operation modes [24].

The subsequent section is focused on the main, generally recognized classification of the modes, which illustrates the operation of the AFM technique most clearly. In Fig. 4.3. the basic three modes of AFM operation are shown, which have been briefly described.

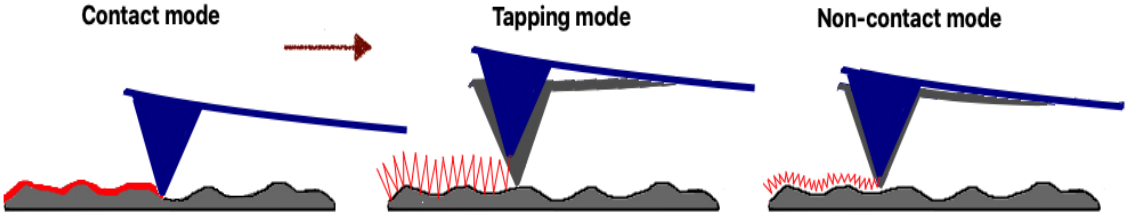

Fig. 4.3. AFM operation modes depending on the distance between the tip and sample surfaces.

❖ **Contact mode**

It is also known as a repulsive mode. In that case the tip contacts directly with the examined surface at constant force or at distance. As can be seen in [23], the slope of the van der Waals force is very steep; hence, it balances almost any force that tries to move the atoms closer together. The result is that the cantilever bends rather than forcing the tip atoms closer to the sample atoms. The height of the cantilever is regulated by the feedback circuit (deflection setpoint). Detector controls the changing deflection of the cantilever, and the force (repulsive) can be calculated according to Hooke's law (4.1):

$$F = k \cdot \mathrm{x}, \quad (4.1)$$

where *k* is a spring constant, and *x* is cantilever deflection.

The force is usually in the range of 0.1 ÷ 1000 nN, as it directly affects the surface of the probe, which can lead to its destruction. After the system detects the deflection of the cantilever, depending on the samples used, the type of tips, etc., it is possible to work in one of two sub-modes.

In the constant force method, the height of the tip is constantly regulated to keep a certain deflection. During the measurements, high resolution could be achieved; however, the speed is limited. In the second case, constant distance, due to the fixed height of the scanner, the topographic data set can be generated by directly used spatial variation of cantilever deflection. To retain control during scanning for the feedback loop, the sample should be sufficiently smooth, but the high speed of scanning is the advantage.

❖ **Non-contact mode**

In this case, there is no contact between the cantilever and the tested surface, thus it cannot be destroyed. Unlike the other modes, the advantage here is that it can be used with soft, not necessarily conducting samples. It is based on the principle of "amplitude modulation" detection and is controlled by a Z-servo system feedback loop. In contact mode, the attractive forces between the sample and the tip are much larger than in that application; hence, in non-contact mode the tip must be given a small oscillation (< 10 nm) slightly above its resonant frequency at a constant oscillation amplitude. The oscillation takes place above the sample, and images can be created by scanning the tip above the surface. The van der Waals attraction force causes changes in both amplitudes and the vibration phase of the support when the tip is getting closer to the probe. Three types of construction of the image can be distinguished: magnetic, electrostatic and tapping. The first two are typical examples of non-

contact mode, while the last is actually intermittent contact mode and will be discussed as a separate issue. In magnetic exchange force microscopy magnetic tips are used to achieve with atomic resolution the distribution for magnetic moments on the surfaces in opposition to the second case, where the electrostatic force is analyzed. Various factors must be analyzed to obtain the result, such as the tip configuration, the role of the chosen applied field, the magnitude of the signals, and the interaction between the forces [25].

- **Tapping mode**

It is the most commonly used dynamic method, where the cantilever oscillates (taps) vertically with or slightly below the resonance frequency with the amplitude mostly in the range of 20 ÷ 100nm. The distance between the tip and probe is controlled by electronic feedback to achieve either the phase or the amplitude in constant. Vibration is caused by piezo motion driving an external frequency generator, next the tip is moved in the surface direction until they are in slight contact. Periodic tapping with the substrate causes the reduction in oscillation due to the energy loss, since the cantilever has less space. The opposite situation appears, when it meets the depression (Fig. 4.4.). The piezoelectric scanner reacts to those changes by deflecting the sample in such a way that the amplitude is maintained at a preset level (related to the change in voltage), the analysis of changes is possible thanks to the reflected laser beam. Such phenomenon is used for measurements and identification of the surface topography [26]. Tapping mode gives better resolution than in contact mode, because cantilever tap and straightly detaches the surface during each oscillation and the lateral tip-sample forces are avoided [27].

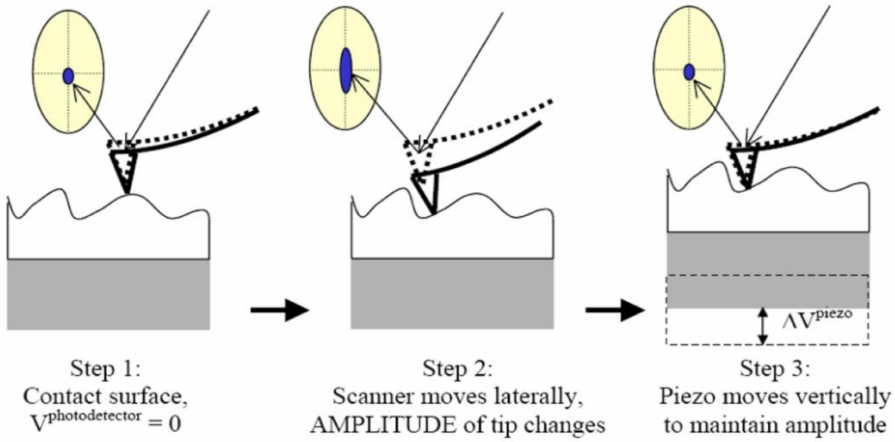

Fig. 4.4. Steps of surface investigation in tapping mode AFM [26].

Using the above-described modes the AFM method makes it possible to characterize the surface morphology of the samples under investigation.

Apparatus

A typical AFM instrument always contains the following main components: sample on the piezoelectric tube, tip-cantilever array, laser or laser diode, quadrant photodiode detector and control electronics with display, as shown in Fig. 4.5.

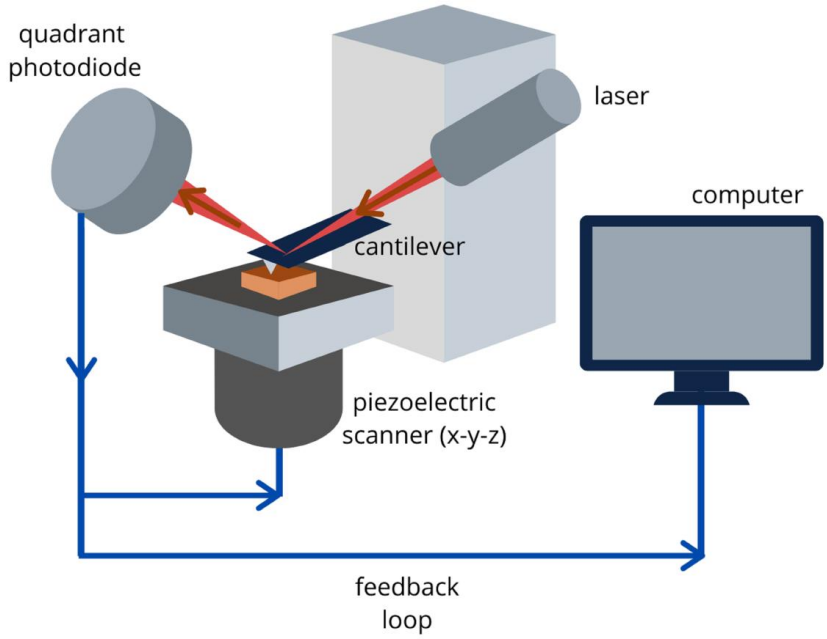

Fig. 4.5. General idea (scheme) of AFM instrument.

The probe should be placed on the appropriate stage. The piezoelectric element is handled by the cantilever oscillation, on which the appropriate tip is placed. There is a force sensor created by the light lever – the beam of the laser is focused on the cantilever and reflected into the photodetector. When the topographic changes of the examined sample appear, the sensor checks the output force and sends that value to the feedback controller. It affects the piezoelectric scanner under the influence of voltage; the scanner deviates in such a way that the tip stays at a constant force or height, depending on the required properties. The detector reads the movement and converts it into an electrical signal. Finally, the graph corresponding to the sample being tested is displayed on the monitor in the appropriate program.

In accordance with the mode of operation, some steps can vary. In contact mode, the cantilever deflection is detected and compared with the desired value in the feedback controller. In the case of differences the amplifier applies voltage to the piezoelectric scanner to set the sample in a proper position when the required values are equal. The situation is slightly different in the tapping mode. The feedback loop makes it possible to keep the amplitude of oscillation of the cantilever constant. It is necessary to obtain the proper oscillation frequency, at the lowest possible level is supported by the software.

Depending on the type of surface to be examined, its softness, morphological structure or the mode of use of microscope, various types of cantilevers can be distinguished. They are long in the range of 100 ÷ 500 μm and they are thick in the range of 0.5 ÷ 5 μm, mostly made of monolithic silicon with different dopants to dissipate electrostatic charges. Due to their chemical volatility and high mechanical Q-factor, they become more sensitive. What is crucial, the sharp tips, located at the end of cantilever, have a different geometry, mostly based on triangular and rectangular shapes, with the radius in the range of 1 ÷ 10 nm, being pyramidal with a polygonal shape or conical and may be made of a variety of materials suitable for the test probes [28]. It is very important to place the tip on the cantilever in the proper way to obtain the correct image, avoid scratching the surface of the sample and damaging it. Moreover, tips are really small and sensitive, hence they could be broken easily.

Abilities

The basic analytical information that can be obtained with the AFM method is available in the form of specific AFM images containing the set of characteristic features mainly related to the surface morphology (topography) of the sample under study. It can be divided into three groups, as listed below:

- 2D topography and 3D dimensions morphology containing information on:
  - characteristic features at top of surface as well as in subsurface materials with the main contribution from grains found at sample surface,
  - the average dimension of the specific object imaged at the material surface (width, height),
  - distribution of specific objects at material surface with respect to dimension,
- Atomic surface profile along a specific axis by using specific software (like WSxM5.0),
- Surface roughness including RMS parameter by using specific software (like WSxM5.0).

Advantages

The main advantages of AFM method are related to the fact that:

- samples viewed by AFM do not require special treatments, it perfectly works in air and liquid,
- AFM provides a true 3D surface profile,
- AFM gives true atomic resolution under UHV, and also in liquid environments,

- high resolution AFM (especially in UHV) is comparable in resolution to other commonly used microscopic methods like STM and TEM.

Limitations

The basic limitations of the AFM method are related to the following:

- image size (maximum scanning area is around 150 by 150 mm),
- incorrect choice of the tip for the required lateral resolution can lead to image artifacts,
- relatively slow rate of scanning during AFM imaging (especially at contact mode) often leads to thermal drift in image,
- images can be affected by hysteresis of piezoelectric material and cross-talk between the (x,y,z) axes, which may require software enhancement and filtering.

4.2. Scanning Electron Microscopy (SEM)

The Electron Microscopy (EM) methods are the tools to obtain high resolution images of the samples. For this purpose, instead of light in optical microscopes, electrons are used as a source of radiation due to their very short wavelengths.

Basically, two main types of electron microscopes can be distinguished according to the different information that can be obtained, i.e. Transmission Electron Microscope (TEM) and Scanning Electron Microscope (SEM). The main difference between them is in the optics, signal detection and the type of information that can be achieved.

In general in the SEM method the images are created by scanning a high energy electron beam on the surface of the sample.

In this work the Scanning Electron Microscopy method was mainly used for the control of surface morphology of ZnO nanowires.

Fundamentals

Principally, the SEM experiment takes place in a high vacuum environment in order to avoid pollution and to obtain the image in the best possible resolution. If the system is unsealed, this could result in the appearance of various particles from the outside, as well as deflection of the electron beam and a problem with their collection.

Generally, in this method the beam is scanned across the sample, and the reemitted electrons are measured combined with the electronic unit for steering and control of the measuring process and subsequent data acquisition in order to form the respective image. In other words, the electron beam interacts with the atoms at different depths in the sample.

Electrons are able to distinguish more details and finer features of the examined surface due to the shorter wavelength. This produces various signals, such as secondary electrons (SE), Auger electrons, backscattered electrons (BSE), characteristic X-rays, photons, and so on. For the creation of the image SE, which are emitted from the surface, and BSE, generated deeper, are used. However, apart from those electrons, generated specific X-rays are also detected and can be used in the energy-dispersive X-ray spectroscopy (EDX) for additional mapping of the distribution and estimation of concentration of elements in the sample.

In Fig. 4.6. various signals (particles) coming out from the sample after interaction with the electron beam and their distribution are presented.

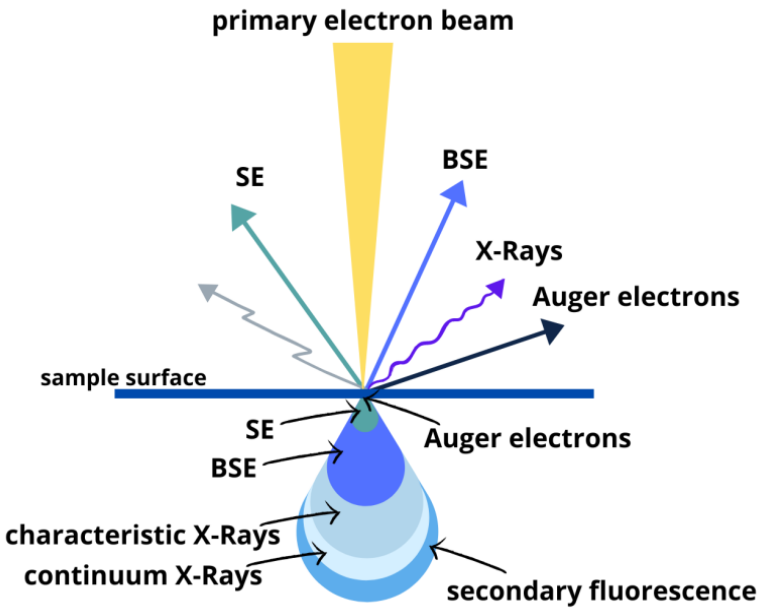

Fig. 4.6. Various outcoming particles (signals) from the sample after interaction with the electron observed in electron microscope experiments.

Apparatus

The typical SEM instrument contains the following main components: i.e. electron gun, anode, different lenses, sample under investigation in UHV chamber, electron detector, amplifier, monitor. A simplified scheme of the SEM instrument is shown in Fig. 4.7.

Generally, the electron microscope instrument contains two main parts: electron column and sample chamber. Inside the first part, electron gun, scan coils, condenser and objective apertures with proper lens systems are placed. The sample chamber mainly contains the special holder/stage, as well as systems of detectors and additional equipment, which is necessary for the connection with computer systems. At the beginning of the microscope operations, electrons are generated by the electron thermionic source, as well as the Schottky or field-

emission cathode, from where they are emitted. This part is also called an electron gun and it is connected with the high-voltage power system. The typical energy range of electron beam is from 0.2 keV to 40 keV. Thanks to the voltage difference between cathode and positively charged anode, electrons are accelerated and attracted [29]. As mentioned above, all the internal parts of microscope are operating in a high vacuum environment; this is important, among other aspects, to avoid electron scattering.

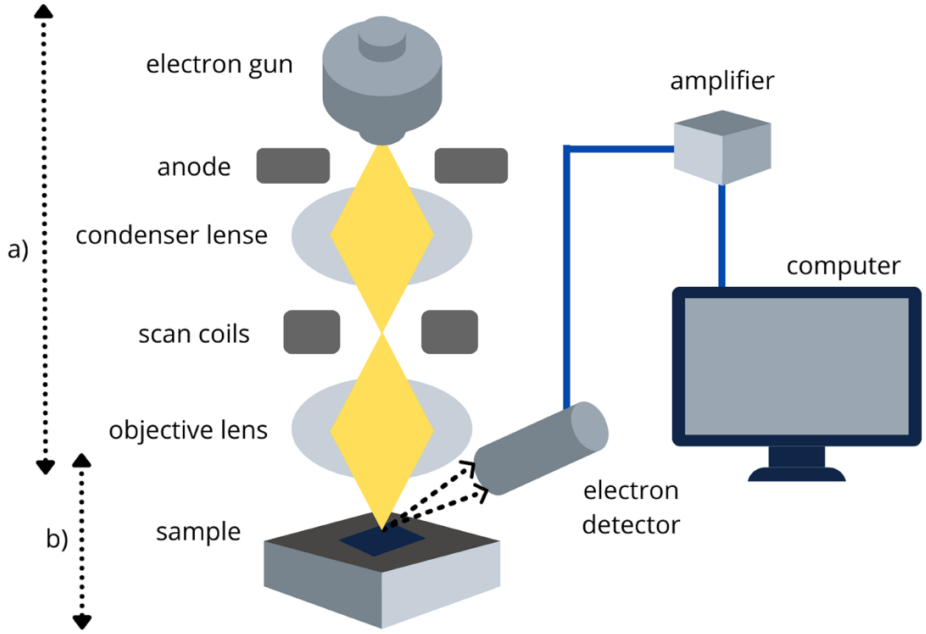

Fig. 4.7. General idea of the scanning electron microscope, where a) is an electron column and b) sample chamber.

In the SEM instrument there are electromagnetic lenses located in the column, which are used to control the electron path. There are two types of lenses: a condenser, typically two lenses at the beginning, which converges or re-converges an electron beam, and an objective which collects the beam again directly before the impact on a probes. The sample should be positioned on a holder that is located in a specimen stage. It can move in the x,y and z directions, tilt and rotate to be able to choose the proper area for testing, set the convenient working distance and improve the signal collection [30]. The samples are scanned in a raster system. It is possible mainly due to scanning coils which are in the above-mentioned lenses. A magnetic field is created by direct current running through the coils, which exert a force upon the electrons moving along the column. The value of the force can be calculated by the formula (4.2):

$$F = B \cdot e \cdot v \cdot \sin \alpha, \qquad (4.2)$$

where B is the magnetic field induction and α is the angle between B and v [30].

Afterwards, the electrons are reflected and collected by the appropriate detectors, which are placed above in the chamber, at the angle to the sample to achieve maximum electron spillage. They collect and convert the signal into an electrical signal that is processed to be finally displayed as an image or spectrum. At the end, the final image is created and presented on the screen of monitor.

Abilities

The basic analytical information that can be obtained with the SEM method is available in specific SEM images, containing the set of characteristic features mainly related to the topography of the surface of the sample under investigation that can be divided into two groups as listed below:

- 2D topography and 3D dimensions morphology containing information on:
  - characteristic features at the top of the surface as well as in subsurface materials with the main contribution from grains found at sample surface,
  - the average dimension of a specific object imaged at the material surface (width, height),
  - distribution of specific objects at material surface with respect to dimension,
- Atomic surface profile along a specific axis by using a cross sectional approach.

Advantages

The main advantages of SEM are such that various electron-specimen interactions appear, beside the backscattered and secondary electrons, which are important for the image creation and provide qualitative and quantitative information. By the manipulation of the current of the scanning coil, the scaling of image can be provided while keeping the size of the image unchanged (about $10x10cm^2$), e.g. magnification increases if the current decreases [29]. Another benefit of this method is related to the fact that it uses a rather simple (easy) analytical (technical) procedure. Additionally, the following advantages can be distinguished:

- Fast time of realization due to the rapid imaging and results obtaining,
- Wide range of samples can be tested in various states of matter,
- High resolution, large depth of field.

Limitations

The basic limitation of the SEM method is as follows:

- The SEM experiment takes place in a high vacuum environment in order to avoid pollution,

- Depending on the form of sample, lateral resolution can be obtained at the level of tens nm, which is comparable to the AFM method, but is evidently lower with respect to the Transmission Electron Microscopy (TEM) method,
- The size of the samples is limited and in the case of non-conductivity properties, they should be coated.

4.3. X-ray Photoelectron Spectroscopy (XPS)

In general, the X-ray Photoelectron Spectroscopy method makes it possible to obtain the information in the form of specific spectra on elemental surface composition of the examined material, its chemical and electrical state of identified elements including its stoichiometry and final surface empirical formula. As mentioned above, the XPS technique was used in this work for the control of surface chemistry, including stoichiometry and surface contaminations, as well as the surface bonds, of the various low dimensional ZnO nanostructures under investigation.

Fundamentals

In general, the XPS method consists in the measuring of photoelectrons emitted from the solids as the results of excitation of atoms in the subsurface region by the beam of X-ray photons. This is because even the penetration depth and respective excitation area are at the level of mm, the photoexcited electron can only be emitted from the specific narrow solid angle, as shown in Fig. 4.8.

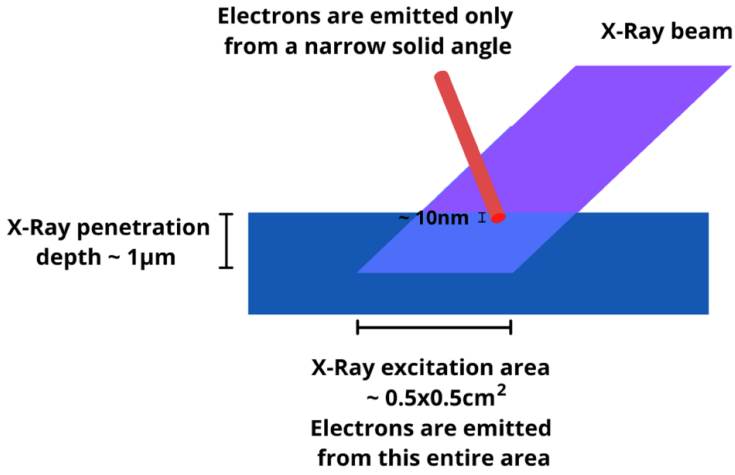

Fig. 4.8. General idea of the XPS method including the penetration of the X-ray beam in subsurface region and subsequent photoexcitation of atoms and emission of photoelectrons from the solid.

What is crucial, in the case of semiconductors, the X-ray photons penetrate the surface layer and cause the emission of photoelectrons from the core levels of ionized atoms, as shown in Fig. 4.9., as well as from valence bands. However, apart from the emission of photoelec-

trons, the simultaneous undesired generation and emission of Auger electrons are observed and commonly analyzed in the Auger Electron Spectroscopy (AES) method.

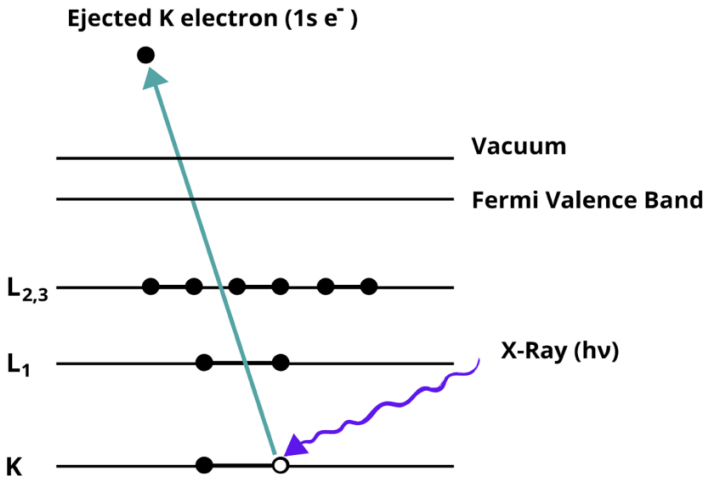

Fig. 4.9. Band scheme of the photoemission process used in the XPS method.

The mechanism of photoemission process of electrons from solid state is described by the commonly used three-step band model proposed by Spicer [31], which is used in both fundamental and practical cases, as schematically shown in Fig. 4.10.

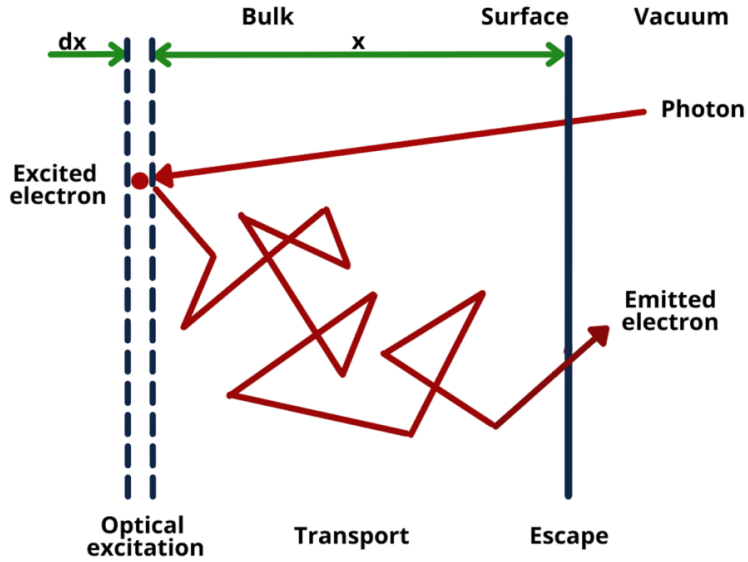

Fig. 4.10. Scheme of the 3-step model of the emission of photoelectrons from the solids.

It consists of:

- Optical excitation of solid,
- Transport of excited electron to solid surface,
- Escape of excited electron from solid to the vacuum.

The intensity I_A of photoelectrons emitted from the solid sample is defined as (4.3) [32]:

$$I_A = N_A \cdot \sigma_A \cdot \lambda_A \cdot K, \quad (4.3)$$

where:

N_A - average concentration per unit volume of chosen element (atom) *A* in subsurface region,

σ_A - photoionization cross section (probability of optical excitation of deep energy levels of selected core levels (corresponding to XPS peak) for the chosen element - atom) *A* of atomic number *Z* (see Fig. 4.11.),

λ_A - inelastic mean free path of a photoelectron from element A, corresponding to the so-called attenuation length, related to the so-called information depth in XPS analysis; for the XPS and UPS binding energy range of 20 ÷ 1200 eV is in the range of 3 ÷ 10 nm, as shown in [33,34],

K - reference parameter which combines together all other experimental and theoretical factors related to the quantitative detection of a signal (supposedly known and assumed to remain constant during the experiments) like photon flux F, depth of photoelectron emission *z*, electron detector efficiency *D* (usually constant), and electron analyzer transmission efficiency *T* (E_A).

This above relation (4.3) is a basis for quantitative analysis of chemical composition (chemistry) at the surface of sample under investigation, that will be more precisely analyzed in Chapter 6.

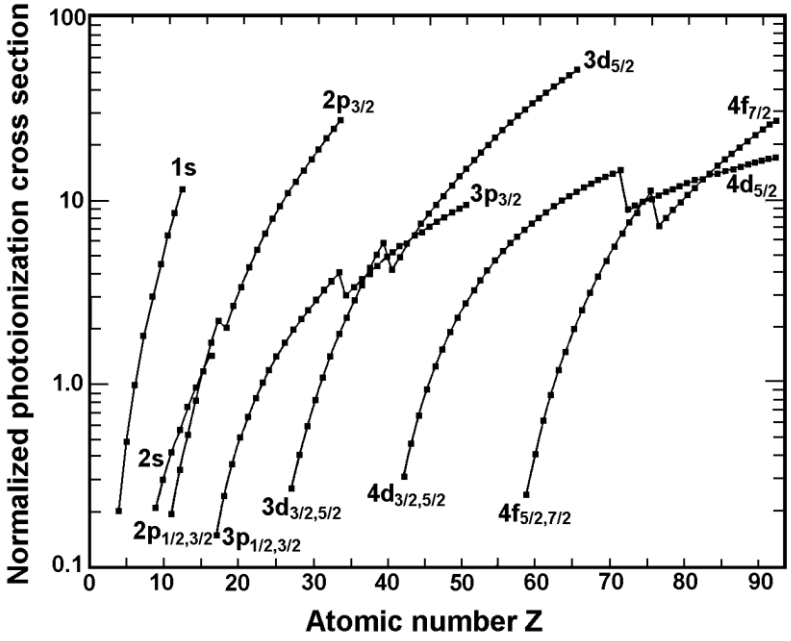

Fig. 4.11. Normalized photoionization cross section of the selected core levels for the chosen element (atom) *A* of atomic number *Z* [35].

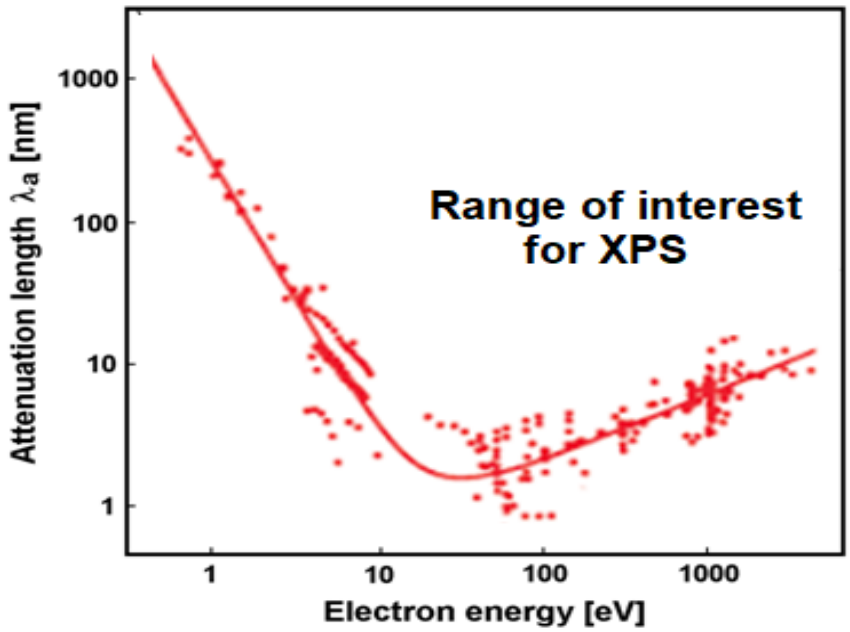

Fig. 4.12. The attenuation length related to depth information versus the energy of excited electrons in ionized atoms [33,34].

However, the most primary qualitative information in the XPS method is the photoelectron energy for the solid defined by the well-known Einstein's relation [36] that says in a summary that many materials emit electrons when they are irradiated by a light, extended with the work function, which is the minimum amount of energy needed to induce the photoemission of electrons from a solid surface (4.4):

$$h\nu = E_b + E_k + \varphi, \quad (4.4)$$

where:

$h\nu$ - primary photon energy,

E_b - binding energy of an electron in the solid,

E_k - kinetic energy of an emitted electron,

φ - electron work function from the solid.

By rearranging the equation accordingly, the kinetic energy of the emitted electrons could be determined as (4.5):

$$E_k = h\nu - E_b - \phi, \quad (4.5)$$

where: ϕ - spectrometer work function.

What is crucial, the binding energy can be described by the difference between initial and final states of the ejected electron. However, in the scale of binding energy, Auger peak positions are dependent on it. XPS makes it possible to identify different elements thanks to the fact that each of them has a unique set of values of binding energies. X-ray energy does not

affect the kinetic energy. In reality, kinetic energies can take on different values, since there are many different possible final states of ions from each atomic type. Furthermore, for each final state, there is a different probability or cross section of the state [37].

Apparatus

In the XPS experiments the photoelectron spectrometer is commonly used, which contains the following main components: i.e. sample under investigation in UHV chamber, which should be equipped with X-ray radiation source and the energy analyzer with electron detector for the analysis of energies of emitted photoelectrons, combined with the electronic unit for steering and control of the measuring process and subsequent data acquisition.
A simplified scheme of the most popular XPS spectrometers (without and with monochromator) is shown in Fig. 4.13.

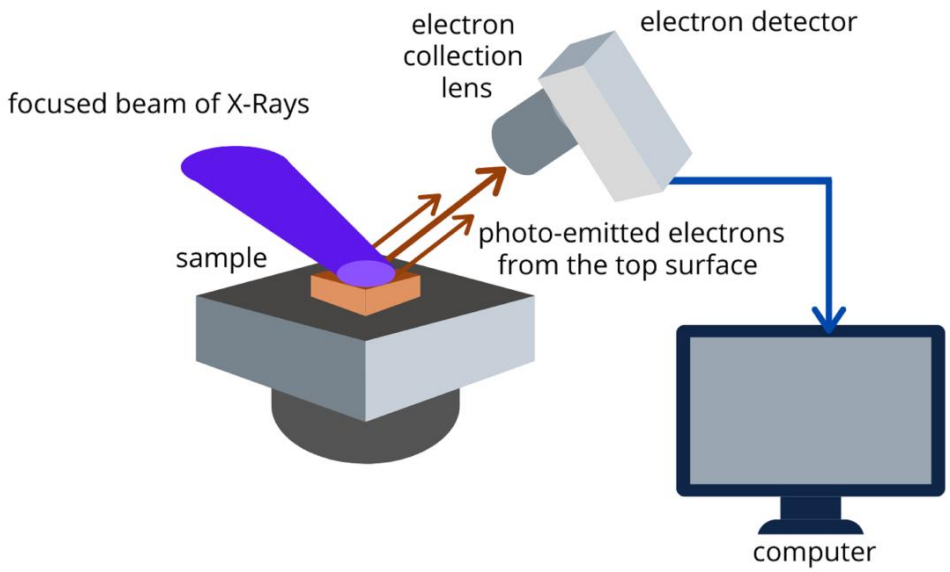

Fig. 4.13. Simplified idea and general scheme of the XPS spectrometer.

As mentioned above, the XPS spectrometer contains mainly the ultrahigh analytical vacuum chamber, which allows the photoelectron path to be extended and the environment to be kept clean as well as protected against contaminants that could interfere with the XPS signal.

In general, the X-ray source (lamp) emits the focused monochromatic X-ray beam, which irradiates the sample surface. Then the X-ray photon is absorbed by the atom or molecule and the electron can be ejected. There is an emission of photoelectrons whose energies are specific to the location. Before the electrons are analyzed by the detector, they pass through a so-called electron analyzer. There is a lens system, which collects the emitted elec-

trons and delays their velocity so that their kinetic energy corresponds to that of a concentric hemispherical analyzer (CHA) and can then be carried through holes and focused on the input slot of the analyzer. Next, the detector collects photoelectrons, measures their kinetic energy (E_k) and electrons emitted from the upper part (1 ÷ 10 nm depth) of the material, which generates the respective XPS spectrum to be received and displayed on a monitor screen. As mentioned before, the kinetic energy of the emitted photoelectron is dependent on the photon energy ($h\nu$) and bonding energy (E_b) of the electron.

The schematic view of the way of photoelectrons, lens systems and HSA with the detector is presented in Fig. 4.14.

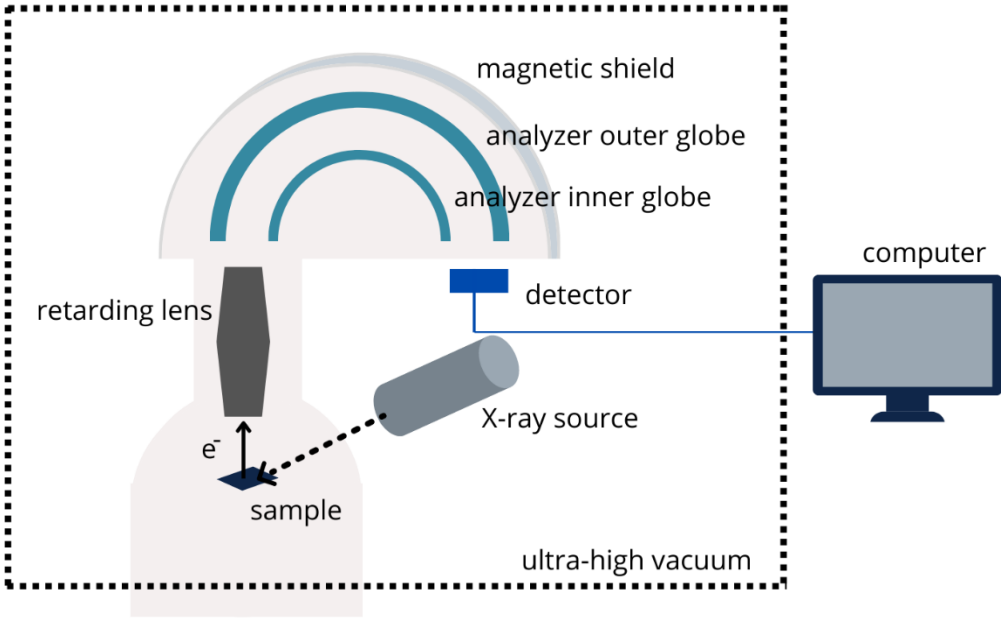

Fig. 4.14. Simplified scheme of the path of photoelectrons into CHA analyzer.

The XPS spectrum is obtained by counting ejected electrons in the whole range of the electron kinetic energy. It is presented as a plot of the number of detected electrons per energy interval versus their binding energy. As each element has its own unique spectrum, through the above-mentioned measurement it is possible to determine which one is on the surface of the tested sample, as well as its chemical state and electron bond energy. The sum of respective peaks of the individual constituents is approximated by a spectrum from a mixture of elements [37].

Moreover, the atoms of emitting electrons of a certain energy characterize the peaks in the spectrum. Identification and quantification of all surface elements (except hydrogen) are possible due to energy value and intensity of photoelectron peaks.

Abilities

As mentioned above, the basic analytical information that can be obtained with the XPS method is available in the XPS spectra, containing the set of characteristic peaks in various binding energy regions, which corresponds to the contribution of every element(s) that can be found at sample surface. This information can be divided into two groups, as listed below:

- Surface chemistry, including:
  - identification of chemical state based on the determination of spectral line energy, elemental identification of surface atoms including surface chemical bondings based on their binding energy (qualitative analysis),
  - surface chemical composition and corresponding relative concentration of various, elements (atoms), even at the level 0.01 monolayer - quantitative analysis - including depth profiling (DPXPS),
- Electronic properties of space charge layer (SCL) including:
  - relative position of surface Fermi level E_F, corresponding to the zero binding energy with respect to the top of the valence band at the surface E_V, corresponding to the surface potential (band bending $e \cdot V_s$),
  - distribution of the occupied electronic states in upper part of the valence band (VB), as well as in the band gap of semiconductor (BG).

Advantages

The main advantages of XPS method are related to the fact that:

- it can be widely used for the analysis of chemical surface properties of various materials,
- the information depth is at the level of single nm (single atomic layers), hence XPS is really a surface analytical method,
- when using the CHA analyzer combined with the channeltron or channel plate detector for photoelectrons, the sensitivity of the XPS method in detection of surface atoms is at the level of 0.01%.

Limitations

The basic limitation of the XPS method is related to the fact that for obtaining the highest binding energy resolution of XPS spectra (at the level of kT), the monochromatization of X-ray radiation is indispensable.

4.4. Thermal Desorption Spectroscopy (TDS)

In general, Thermal Desorption Spectroscopy is a method which makes it possible to obtain the information in the form of specific spectra on the competitive desorption effects for specific particles from the surface of the sample under investigation under its increased temperature.

As mentioned above, the TDS technique was used in this work for the control of the desorption process of surface contaminations of the residual gases from the low dimensional ZnO nanostructures under investigation.

Fundamentals

In general, the TDS method consists in the measuring of surface species (molecules) by the Mass Spectrometry (MS) method; molecules can be desorbed from the surface of the sample during its heating under ultrahigh vacuum (UHV) conditions with linearly increased temperature *T* in time *t*, which can be described as (4.6):

$$\beta(t) = \frac{dT}{dt}, \quad (4.6)$$

This is why the TDS is also commonly called TPD - Temperature Programmed Desorption.

The process schematically shown in Fig. 4.15. is related to the respective variation of partial pressure(s) of various gas species inside the measuring chamber with linear heating rate (ramp).

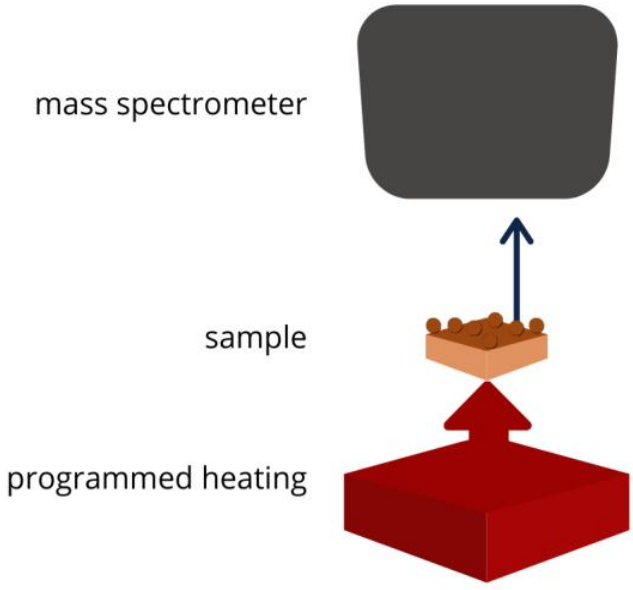

Fig. 4.15. Simplified idea of the thermal desorption process of gases from the sample surface.

The rate of gas desorption strongly depends on the precisely defined specific experimental conditions and can be described by the Polanyi-Wigner equation (4.7) [38] based on the Arrhenius expression:

$$-\frac{d\theta}{dt} = \theta^n v_0 \exp\left(-\frac{E_{des}}{k_B T}\right), \quad (4.7)$$

where:

θ - instantaneous surface coverage,

$d\theta/dt$ - desorption rate per unit area,

n - information on the adsorption and desorption mechanism,

θ - instantaneous surface coverage,

v_0 - attempt frequency,

E_{des} - desorption barrier,

k_B - Boltzmann constant,

T - sample temperature.

After converting the aforementioned equation by taking into account that temperature is increasing linearly, the following formula is obtained (4.8) [38]:

$$-\frac{d\theta}{dt} = \frac{\theta^n v_0}{\beta} \exp\left(-\frac{E_{des}}{k_B T}\right), \quad (4.8)$$

where: β - heating rate in the function of time $T = T_0 + \beta t$.

The shape of respective TDS peaks depends on the surface coverage and order of gas desorption. What is crucial, the temperature maximum of TDS peak is invariant with initial coverage only for the first-order thermal desorption (reaction), which is the most common effect observed on the surface of semiconductor materials, and can be used for the determination of desorption energy E_{des}. Thus, from the TDS spectrum the respective parameters like E_{des}, v_0 and n values could be obtained.

Apparatus

In general, Thermal Desorption Spectrometer (TDS) contains the following main components, i.e. the UHV chamber for thermal desorption experiments dynamically pumped at constant speed (turbomolecular systems are commonly used), DC power supply for the thermal heating of the sample at increasing linear temperature ramp, quadrupole mass spectrometer (QMS) or residual gas analyzer (RGA) for the detection of relevant desorbing species (gases) related to the control of variation of their partial pressure, and electronic unit for

steering and control of the TPD process combined with data acquisition, as schematically shown in Fig. 4.16.

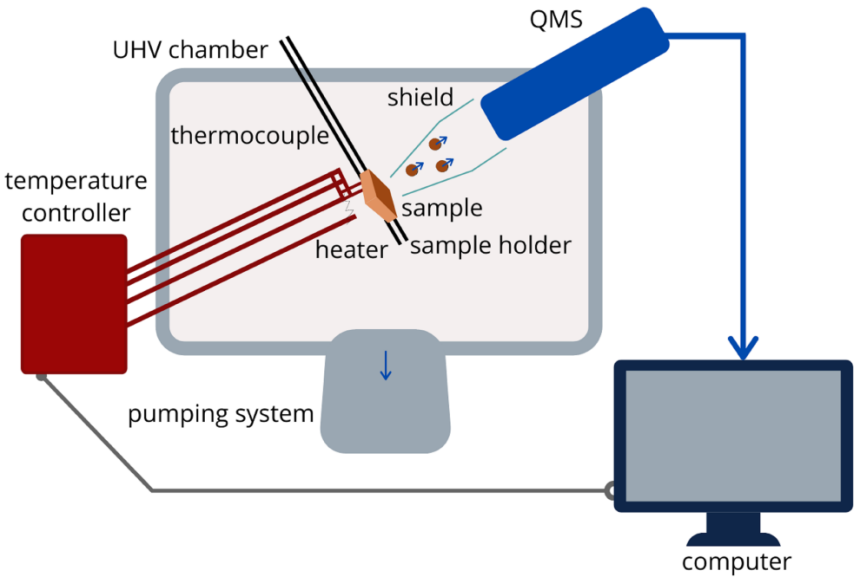

Fig. 4.16. Simplified idea and scheme of TDS spectrometer.

In general, within the operation of the TDS experiment method the following steps can be distinguished: after placing a sample with a certain amount of absorbed molecules in a suitable place, a gradual increase in temperature controlled by the thermocouple, using the programmed heating system, which causes the desorption of species from the surface being investigated. The ability to react to the desorbing molecules is provided by a specially designed sampling end, mainly cone-shaped. They are then analyzed by a mass spectrometer and finally the result can be achieved in the form of the TPD spectrum. With this method it is possible to observe, among other things, the amount of desorbed particles by analyzing the intensity of peaks on the spectrum, as well as their total amount through the total spectrum.

Abilities

The basic analytical information that can be obtained with the TDS method is available in the TDS spectra, containing the set of mass spectrometry partial pressures maximum peaks at the respective desorption temperature related to the specific ions corresponding to the atoms or molecules desorbing from the sample. The information allows us to control the desorption process of specific gas species adsorbed at the sample surface, usually in air atmosphere conditions. Moreover, from the maximum of the temperature for partial pressures of specific gas species their desorption energy can be estimated.

Advantages

The main advantages of the TDS method are related to the fact that it enables a simple and direct control of thermal desorption of specific gas species adsorbed at the sample surface. It makes it possible to determine interactions and kinetic parameters of adsorbents. Moreover, the sensitivity and accuracy of the TDS method is related to the ability of mass spectrometer used. With modern equipment, a wide operating temperature range is possible, which increases the variety of materials to be tested, as well as fully programmable control to improve the diversity of the tests.

Limitations

The basic limitation of the TDS method is related to the fact that for obtaining the highest reliability of the information on condition of the desorption of specific gas species from the sample surface, the properly controlled and repeatable pumping conditions should be allowed. Experiments are not repeatable if the desorbed gases do not return to the surface of the sample, so the working conditions must be right and the equipment must be properly calibrated. Moreover, there is no indication what is still left in the sample. Some of the adsorbents could decompose or react in various ways resulting in new chemical compounds what prevented them being removed from the surface.

Chapter 5.
Experimental methodology of preparation and characterization of selected ZnO nanostructures

5.1. Preparation of selected ZnO nanostructures

For the experimental part of the thesis, depending on the research being done, the specific, distinct types of samples were used, i.e. the nanostructure ZnO thin films and the ZnO nanowires. The methodology of their preparation (deposition) are precisely described below, in the subsequent subsections.

5.1.1. Nanostructured ZnO thin films

For preparation of the nanostructured ZnO thin films, the direct current reactive magnetron sputtering (DCMS) method (schematically shown above in Fig. 2.9.) was applied using the high vacuum reactor of an installation of Surrey NanoSystems γ 1000 C model (UK) in the Łukasiewicz Research Network - Institute of Electron Technology, Warsaw, Poland.

The above mentioned nanostructured ZnO thin films were deposited on Si(100) substrate degreased by boiling in trichloroethylene, acetone and isopropanol and bathed in buffered HF solution to remove any native oxide [39,40]. In the deposition process the 99.95 % pure Zn target with 75 mm diameter was used and the following technological parameters were implemented: 80 W DC under 3 mtorr constant total pressure with the various Ar/O_2 gas flows (in sccm: 3:0.3, 8:08, 10:1, 15:1.5 and 30:3, respectively), what allowed us to obtain the nanostructured ZnO thin films of different morphologies.

For the photocatalytic experiments, the chosen DCMS ZnO nanostructured porous thin films were used, which have been deposited on Si(100) substrate by the DC reactive magnetron sputtering method but combined with an additional post-deposition annealing at 700 °C [41] to obtain the optimal, more flat morphology, evidently crucial for our photocatalytic experiments combined with the purification processes of water contaminated with organic compounds. The details of these studies and the obtained results have been precisely described in Chapter 8. The exemplary samples used for are shown in Fig. 5.1.

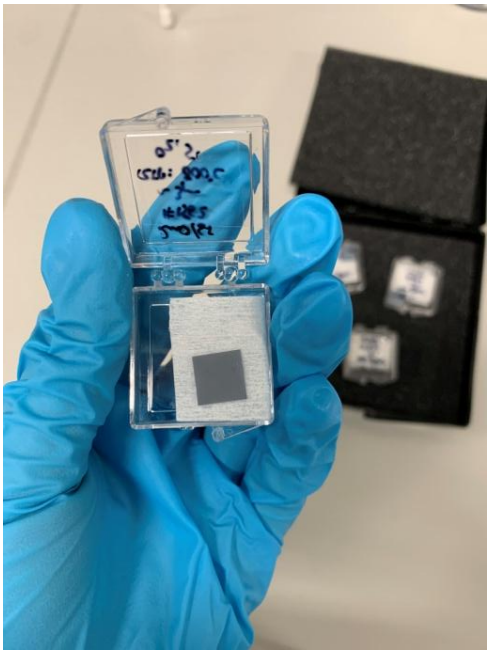

Fig. 5.1. Photo of nanostructured ZnO thin films deposited on Si substrate used in our photocatalytic experiments.

5.1.2. ZnO nanowires

For the preparation of ZnO nanowires the vapor phase deposition (VPD) method based on the subsequent evaporation-condensation process was applied, using the deposition system schematically shown above in Fig. 2.10, which is available in the SENSOR Lab, Department of Information Engineering, University in Brescia (Italy).

The ECM ZnO nanowires were deposited on Ag-covered Si(100) substrate from the ZnO powder, which was placed in the middle of furnace at high temperature of 1370 ºC and then condensed in a colder region (around 700 ºC) at the surface of substrate. For moving the evaporated material, an inner gas flow (Ar, 100 sccm) was applied. For the control the pressure inside at the level of 100 mbar the barometer - MKS model (Germany) was used.

The catalyzed growth assisted Ag nanoparticles were deposited on Si substrate by the DC magnetron sputtering method using the Kenotic system (Italy), which enabled to achieve good uniformity of ZnO NWs lateral dimensions [21].

Such prepared ZnO nanowires have been used as the electrode material in our novel type SPV gas sensor system for the determination of their gas sensor characteristics in NO_2 toxic gas atmosphere. The details of these studies and the obtained results have been precisely described in Chapter 8.

5.2. Methodology of surface characterization of selected ZnO nanostructures

5.2.1. Characterization of surface atomic structure and morphology by AFM and SEM methods

The morphology of nanostructured ZnO thin films was investigated by using the AFM Bruker MultiMode 8 system (Bruker, Santa Barbara, CA, USA), shown in Fig. 5.2, which consists of MultiMode8 head completed with three scanners (AS-130VLR-2, AS-2VLR-2 and AS-05-2) with different scanning ranges (areas). For the further analysis of achieved images, NANOSCOPE V controller with the original NanoScope V9.10 software was used. The AFM experiments were hold in Department of Cybernetics, Nanotechnology and Data Processing at Silesian University of Technology, Gliwice, Poland.

Fig. 5.2. Atomic Force Microscope at Department of Cybernetics, Nanotechnology and Data Processing, Silesian University of Technology, Gliwice, Poland.

In addition, the morphology of nanostructured ZnO thin films has also been controlled by the SEM method in a close cooperation with the Institute of Physics, Polish Academy of Sciences, Warsaw (Poland), using the commercial, high resolution scanning electron microscope HR SEM - Carl Zeiss Auriga 60 model (Germany) operating at 5 keV, with a lateral resolution of 2 nm, which is shown in Fig.5.3.

Fig. 5.3. HR SEM Instrument in Institite of Physics, Polish Academy of Sciences, Warsaw, Poland.

In turn, the experimental SEM characterization of the surface morphological properties of ZnO nanowires deposited at the Si(100) substrate by VPD method, was performed in cooperation with the SENSOR Lab, Department of Information Engineering (DII) in Brescia University (Italy), with the usage of Field-Emission Scanning Electron Microscope (FE-SEM, Gemini, Leo 1525 model), operating in the range of 3-5 keV, which is shown in Fig. 5.4.

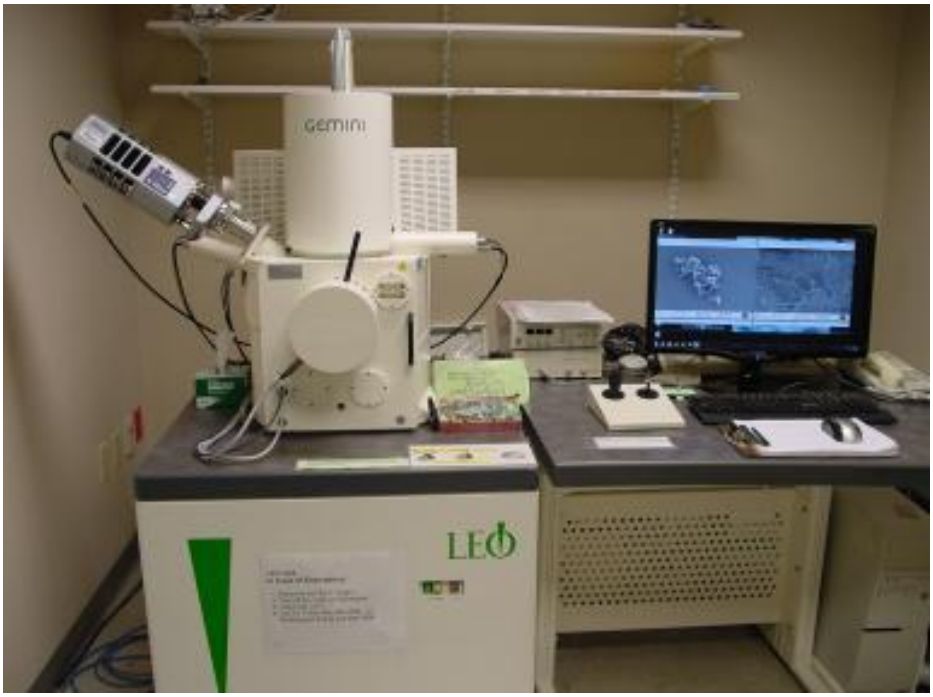

Fig. 5.4. FE-SEM instrument in SENSOR Lab, Brescia University, Italy.

5.2.2. Characterization of surface chemistry including contaminations by XPS method

The XPS studies of the above mentioned two low dimensional ZnO nanostructures were performed at the Department of Cybernetics, Nanotechnology and Data Processing, Silesian University of Technology, Gliwice, Poland, by using a commercial XPS spectrometer (SPECS, Berlin, Germany) equipped, among others, with the sample manipulator, an X-ray source (lamp -AlK_α, 1486.6 eV, XR-50 model) and the concentric hemispherical analyzer CHA (PHOIBOS-100 Model), which is shown in Fig. 5.5.

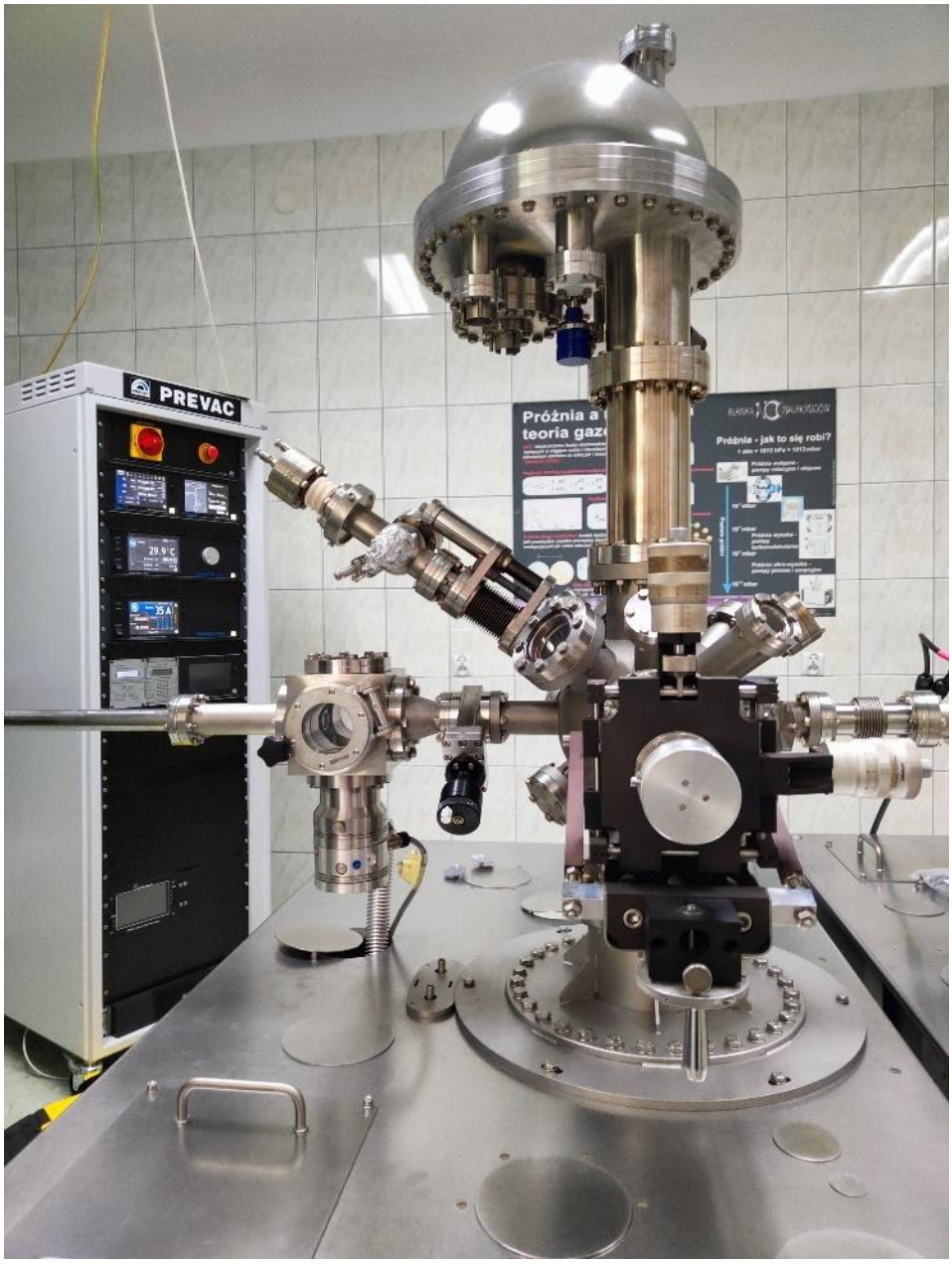

Fig. 5.5. X-ray Photoelectron Spectrometer (XPS) at the Department of Cybernetics, Nanotechnology and Data Processing, Silesian University of Technology, Gliwice, Poland.

5.2.3. Residual gas interaction at surfaces using TDS method

For detection of specific active surface gases desorbed from the above mentioned ZnO samples surface, the TDS measurements by in line mass spectrometry (MS) were performed in the Department of Cybernetics, Nanotechnology and Data Processing, Silesian University of Technology, Gliwice (Poland), using the commercial TDS systems (PREVAC, Poland) based on the UHV chamber, which consists of sample manipulator, resistive type sample heating unit with a temperature programmable control system (OmniVac-Dual Regulated Power Supply PSReg120 model) with a regulation of sample temperature in the range of 50 ÷ 300 ºC, and the mass spectrometer - residual gas analyzer – Stanford RGA200 model (USA). This system is Fig. 5.6.

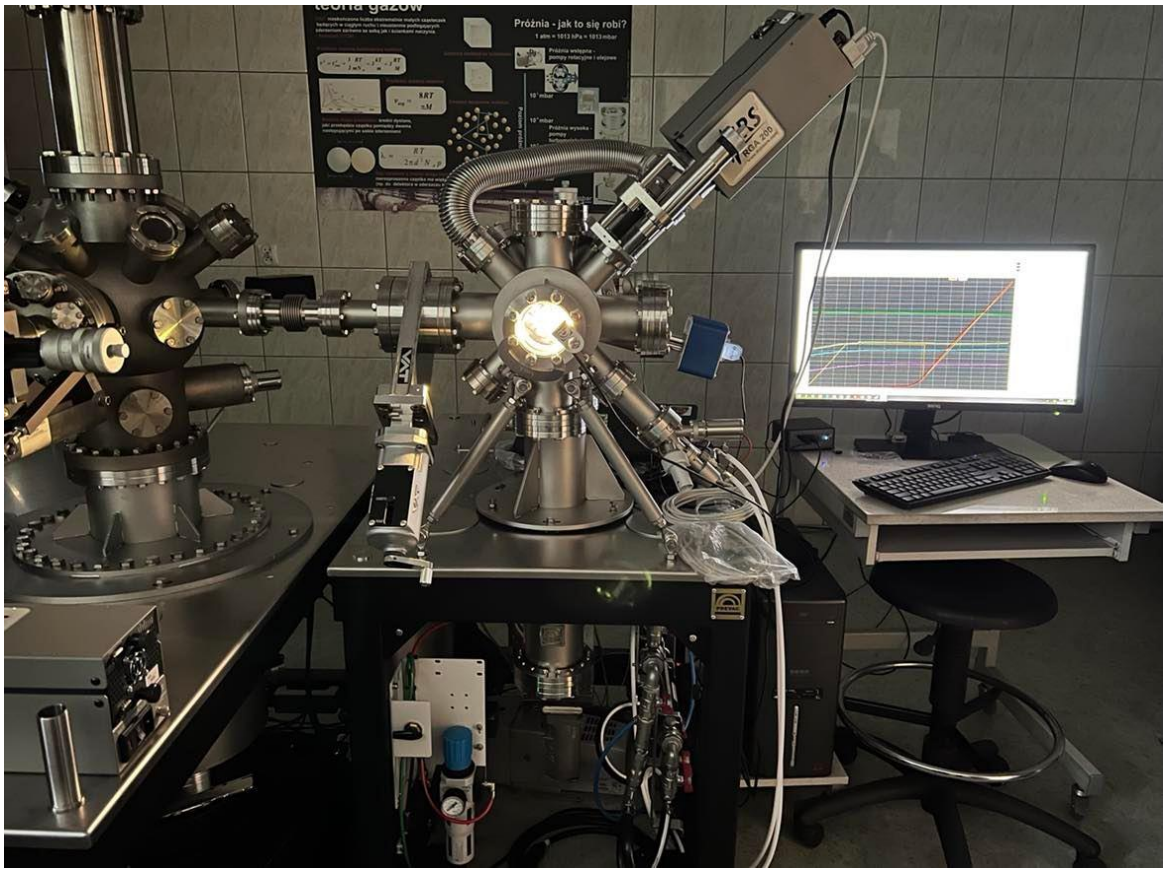

Fig. 5.6. Thermal Desorption Spectrometer (TDS) at the Department of Cybernetics, Nanotechnology and Data Processing, Silesian University of Technology, Gliwice, Poland.

Chapter 6.
Results and discussion on characterization of surface properties of selected ZnO nanostructures

In this chapter, the most significant experimental results on the characterization of surface properties of chosen ZnO nanostructures are presented divided into 2 main sections related to the nanostructured DC RMS ZnO thin films, as well as the VPD ZnO nanowires. Moreover, for both ZnO nanostructures their surface morphology, together with their surface chemistry including their purity and non-stoichiometry, as well as the surface bondings, having the strong direct influence on their electronic properties are presented.

6.1. DCMS nanostructured ZnO thin films

6.1.1. Crystallinity and surface morphology

At the first stage the surface morphology of nanostructured ZnO thin films deposited by the DC RMS technology for different Ar/O_2 gas flow conditions have been studied using the AFM method. It was observed, that only for the nanostructured ZnO samples from extreme gas flow concentrations, the changes in their morphology were noticeable, as shown in Fig. 6.1., where the set of two AFM images corresponding to the nanostructured ZnO thin films deposited at the Ar/O_2 gas flow ratio, consecutively equal to 3:0.3 and 30:3 sccm, are presented.

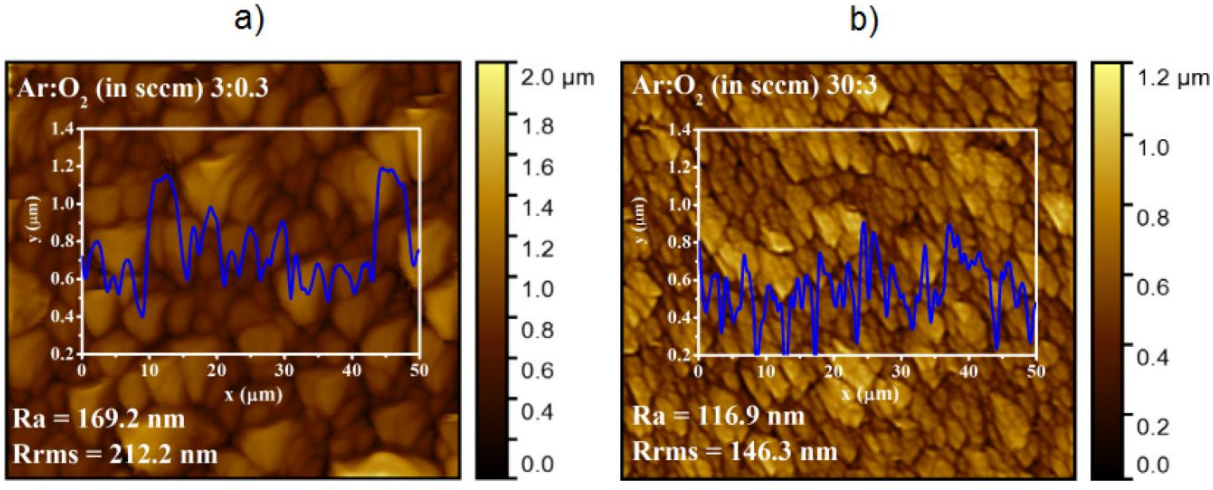

Fig. 6.1. AFM images of nanostructured ZnO thin films deposited at the Ar/O_2 gas flow of 3:0.3 sccm (a) and 30:3 sccm (b); the symbols R_a and R_{rms} denote arithmetical mean deviation of the assessed profile and a root mean square roughness parameter, respectively [40].

For these above images two analytical parameters have been determined, which describe the morphology of investigated surface.

A first one is R_a – arithmetical mean deviation of the profile, that can be ascribed with the following formula (6.1):

$$R_a = \frac{1}{L}\int_0^L |Z(x)|dx, \quad (6.1)$$

where: *Z(x)* is the function of the depth profile and *L* is the length considered.

In turn, a second one: R_{rms} stands for the root mean square roughness.

After detailed analysis of the information shown on images presented in Fig. 6.1. it is possible to observe, that for the least amount of the gas flow ratio, porosity was much lower than in the opposite, extreme case. In the Ar/O_2 flow equal to 30:3 sccm, the shape of ZnO nanostructure was almost similar to nanoflowers with the nanograins of average size in the range of 20 ÷ 40 nm, and the grains with the dimension of about 100 nm were easily identifiable. It can be explained by the fact that only at the highest Ar/O_2 flow rate the highest amount of oxygen inhibits the growth and coalescence of Zn crystallites caused by new nucleation centers at the growth front in the presence of oxygen atoms. Therefore, the morphology is modified by decreasing the size of the crystallites.

At the second stage the crystallinity and surface morphology of nanostructured ZnO thin films deposited by the DC RMS technology for the highest flow of Ar/O_2 mixture after their additional heating at 700 °C have been studied using the HR SEM method. The obtained SEM images for two specific conditions are shown in Fig. 6.2.

On the base of observation of above mentioned images shown in Fig. 6.2., one can observe, that surface morphology of nanostructured ZnO thin films under investigation resembles the coral reef that consists of polycrystalline coral dendrites. It was maintained even with the rechecking of morphology, after 4 cycles of the photocatalysis. However, the statistical analysis of individual crystallites' long and short axis lengths showed, that the size has grown and the median is shifted from 43 to 76 nm (long axis) and from 28 to 58 nm (short axis). It was calculated based on manual determination of crystallite shape and size using the ImageJ processing program. This difference in size can be explained by the presence of residual adsorbed methylene blue (MB) or its photodegradation by-products on the sample‘s surface, as well as by the effect of UV irradiation.

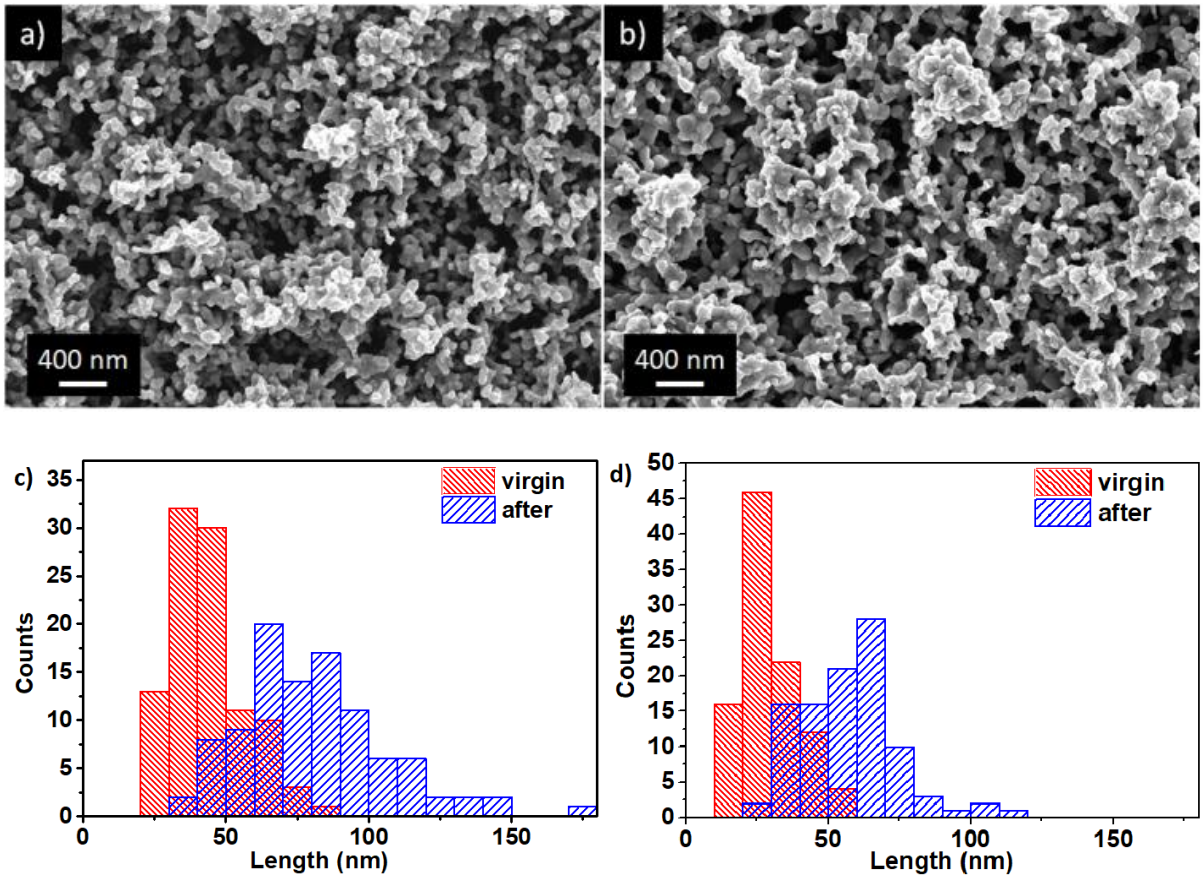

Fig. 6.2. HR SEM images of the nanostructured ZnO thin films for the virgin sample (a) and after 4 cycles of the photocatalysis (b) with histograms of individual nanocrystallites long (c) and short (d) axis lengths after image analysis [40].

6.1.2. Surface chemistry including contaminations

As was mentioned above, apart from the surface morphology of nanostructured ZnO thin films in our experiment their surface chemistry have also been studied including their purity, non-stoichiometry, and surface bondings have, using the XPS method.

As before, at first stage the XPS studies were performed for the nanostructured ZnO thin films deposited by the DC RMS technology for the extremally different Ar/O_2 gase flow conditions 3:0.3 and 30:3 sccm, respectively.

In general, in common XPS studies, the XPS survey spectra within the commonly used binding energy range (1200 eV) are registered. However, due to the large unwanted background - especially in the 1200 ÷ 600 eV range, in order to more precise determination of the relative concentration of major elements at the surface (in the subsurface layers) of nanostructured DC RMS ZnO thin film, only the lower range of binding energy (to 600 eV), has been also registered, what is shown in Fig. 6.3.

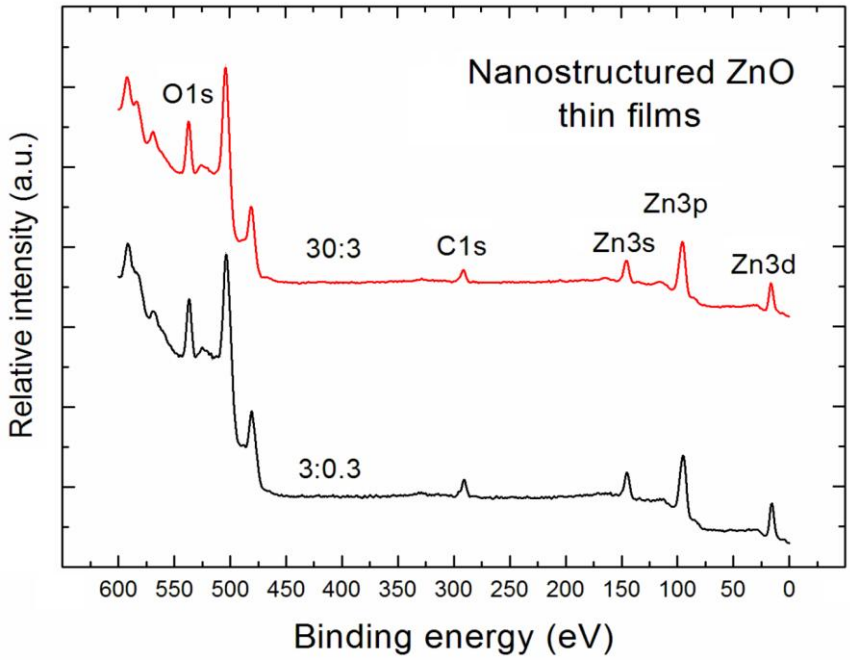

Fig. 6.3. XPS survey spectra in limited binding energy range for the nanostructured ZnO thin films deposited at the gas flow ratio 3:0.3 (black) and 30:3 sccm (red) [40].

One can observed in the XPS spectra presented above, that the contribution of main core level lines O1s, Zn3s, Zn3p and Zn3d, that correspond to the main elements (atoms) in the investigated samples, are clearly visible. Furthermore, the XPS C1s lines can also be noticed related to the undesired C contaminations. It usually appears after exposure of the sample to air atmosphere, e.g. during the transport from the deposition chamber to the XPS analytical chamber. However, it should also be mentioned, that apart from the main core level lines, the additional peaks associated with Auger electron emission lines at ~570 eV, ~500 eV and ~470 eV, corresponding to the Zn $L_3M_{23}M_{45}$, Zn $L_3M_{45}M_{45}$, and Zn $L_2M_{45}M_{45}$ electron transitions, respectively, were also observed, which can be omitted in our further data analysis.

Based on the experimental XPS survey spectra shown in Fig. 6.3., using the well-known analytical formulas [40], it was possible to calculate the relative surface concentration of main elements with respect to all recognized surface atoms, using the set of basic 3 relations shown below (6.2).

$$O: \quad \frac{[O]}{[Zn]+[O]+[C]} = \frac{\frac{I_O}{ASF_O}}{\frac{I_{Zn}}{ASF_{Zn}}+\frac{I_O}{ASF_O}+\frac{I_C}{ASF_C}} \qquad Zn: \quad \frac{[Zn]}{[Zn]+[O]+[C]} = \frac{\frac{I_{Zn}}{ASF_{Zn}}}{\frac{I_{Zn}}{ASF_{Zn}}+\frac{I_O}{ASF_O}+\frac{I_C}{ASF_C}}$$

$$\text{and} \quad C: \quad \frac{[C]}{[Zn]+[O]+[C]} = \frac{\frac{I_C}{ASF_C}}{\frac{I_{Zn}}{ASF_{Zn}}+\frac{I_O}{ASF_O}+\frac{I_C}{ASF_C}} \qquad (6.2)$$

where:

I - the intensity (height) of O1s, C1s and Zn3p core level peaks corrected by the transmission function T(E) of CHA PHOIBOS 100 of 1.00, 0.90 and 0.85, respectively,

ASF - the atomic sensitivity factor for O1s equal to 0.66, C1s to 0.25 and Zn3p to 0.40.

Using the above relation, the relative surface concentrations of main elements with respect to all recognized surface atoms have been determined, which are presented in the Table 6.1. below.

Table 6.1. The relative concentrations of main elements in the subsurface layers of nanostructured ZnO thin films [40].

Ar/O_2 ratio at deposition of ZnO thin films (sccm)	**Relative concentration of the main specific elements**		
	[O]/ ([Zn]+[O]+[C])	**[Zn]/ ([Zn]+[O]+[C])**	**[C]/ ([Zn]+[O]+[C])**
3:0.3	0.25 ÷ 0.03	0.48 ÷ 0.03	0.27 ÷ 0.03
30:3	0.29 ÷ 0.03	0.53 ÷ 0.03	0.18 ÷ 0.03

Based on the analysis of XPS data presented in the Table above, one can noticed that the relative concentration of O atoms with respect to all other surface atoms for the analyzed samples is rather similar, since it varies only in the range of 0.25 ÷ 0.29. Moreover, for the relative concentration of Zn atoms in the same reference, the value is quite stable and changes only in the range of 0.48 ÷ 0.53 (taking into account the accuracy, the respected difference in Zn concentration is more than two times larger).

However, a different relative concentration of C was observed with respect to all other surface atoms. Its amount is clearly different, varying in the range of 0.27 ÷ 0.18 and is significantly lower for nanostructured ZnO thin films deposited at the highest gas flow ratio (30:3). In that case, the specific difference in above mentioned relative concentration with respect to the accuracy is three times larger, what is very important for the further interpretation of presence of unexpected carbon contamination at the surface of our ZnO nanostructures.

The obtained results confirm the evident non-stoichiometry, combined with a high content of C impurities at the surface of our nanostructured ZnO thin films. As this may be attributed to the existence of specific additional oxygen and carbon surface bond forms, the next step was to analyze the local surface chemistry of nanostructured ZnO thin films.

In order to perform the analysis and interpretation of obtained results, the deconvolution of the spectral lines Zn2p, O1s and C1s was performed, using the Casa XPS SPECS software. The achieved spectra (graphs) are presented below (Fig. 6.4., Fig. 6.5. and Fig. 6.6., respectively).

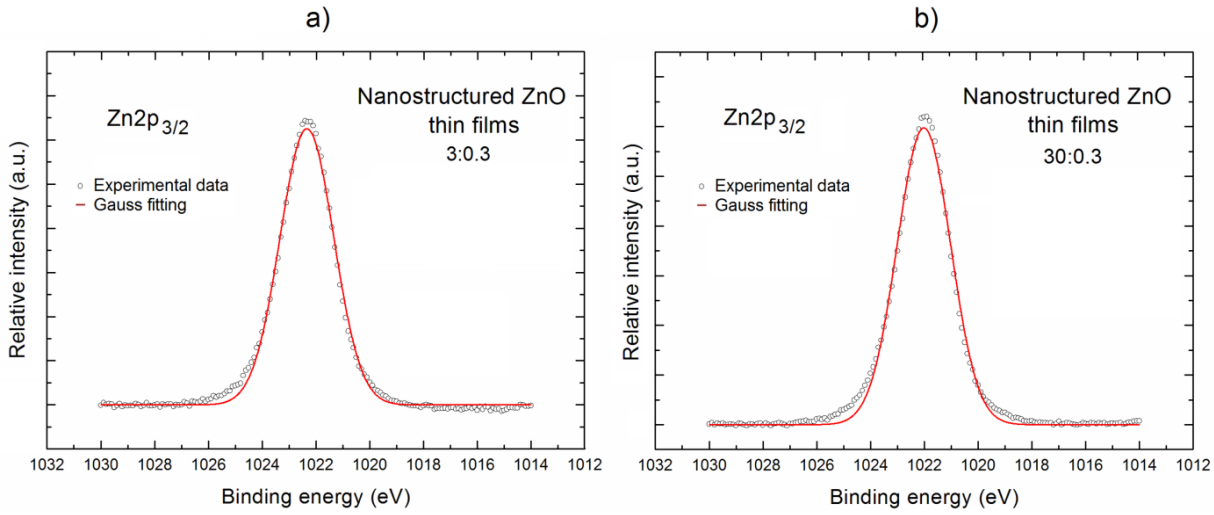

Fig. 6.4. The XPS $Zn2p_{3/2}$ lines after Gauss fitting deconvolution for the nanostructured ZnO thin films deposited at the gas flow ratio respectively (a) 3:0.3 and (b) 30:3 sccm, respectively [40].

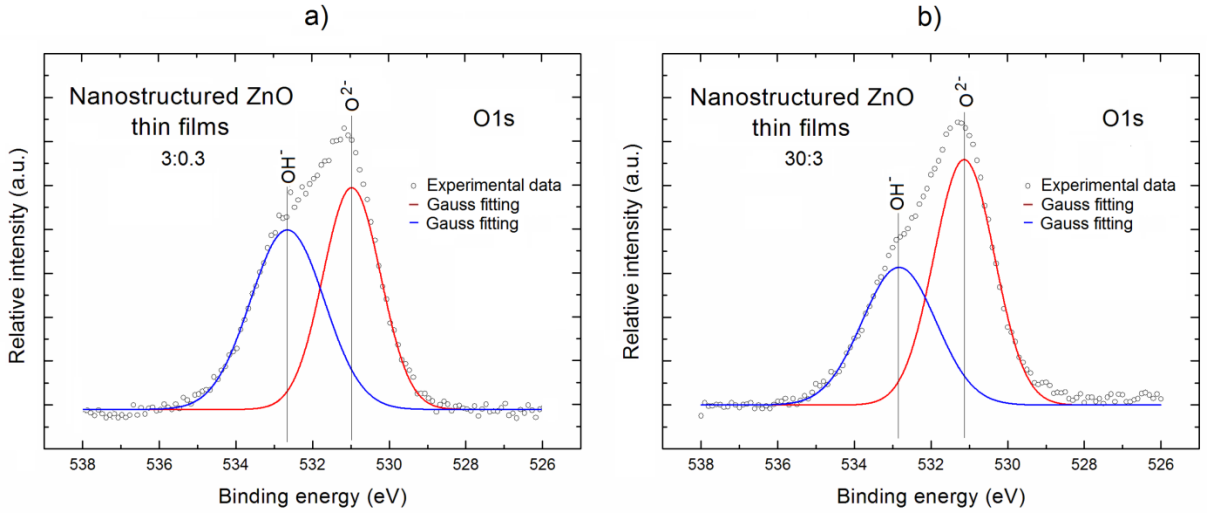

Fig. 6.5. The XPS O1s lines after Gauss fitting deconvolution for the nanostructured ZnO thin films deposited at the gas flow ratio respectively (a) 3:0.3 and (b) 30:3 sccm, characterized by extreme O surface concentration [40].

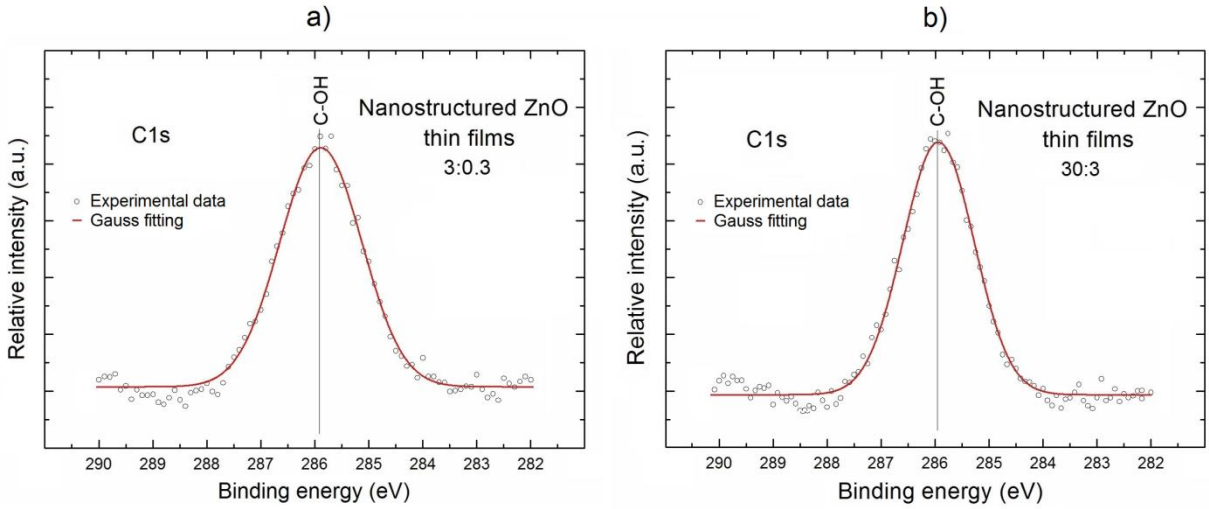

Fig. 6.6. The XPS C1s lines after Gauss fitting deconvolution for the nanostructured ZnO thin films deposited at the gas flow ratio respectively (a) 3:0.3 and (b) 30:3 sccm, characterized by extreme C surface concentration [40].

In the Fig. 6.4. one can observe the deconvolution using Gauss fitting for the XPS $Zn2p_{3/2}$ line, for 3:0.3 and 30:3 sccm Ar/O_2 gas flow ratio, as it had the highest intensity from all Zn XPS peaks. For both investigated ZnO samples, the shape of XPS lines looks symmetrical, whereas in order to verify the surface bonds it was necessary, after appropriate background subtraction, to use deconvolution procedures (as red curves in the graph).

Since the deconvoluted XPS $Zn2p_{3/2}$ lines in both cases have a very large line fitting parameter (RMS = 0.995) and a similar line width (~ 2.4 eV), this proves that only one component is observed always at a binding energy of ~1022 eV, which corresponds to Zn atoms in the ZnO lattice on the surface.

In turn, Fig. 6.5. shows the XPS O1s lines after deconvolution using Gauss fitting for both above mentioned ZnO samples deposited at 3:0.3 and 30:3 sccm Ar/O_2 gas flow ratio. In this case the pronounced asymmetry of this XPS O1s lines is clearly noticeable. This may indicate the existence of different forms of oxygen bonds at the surface of above mentioned ZnO samples. Further, by the detailed verification of potential oxygen bond forms using deconvolution for both ZnO samples it was noticed, that they consist of two components. A first one (blue curve) is located at binding energy ~ 531.0 eV and can be attributed to O_2^- ions in ZnO lattice, while the second one (red) at binding energy ~ 532.5 eV corresponds to oxygen atoms in OH- groups on ZnO surface. The XPS line widths of identified components in both cases are very comparable, being 2.35 eV for the left component and 1.88 eV for the right component, correspondingly.

In addition, by determining the relative area under the components of XPS O1s lines, it was found that for lower Ar/O_2 gas flow ratio the relation between the OH^- groups and O_2^- ions is practically identical (~1.0), while for the second sample (with higher gas ratio) the relative concentration of O_2^- ions in relation to OH- groups increases, achieving the value of ~ 1.5. It should be underlined at this moment that the above mentioned information related to the existence of OH− groups at the surface of our both ZnO samples remains in agreement with the information obtained from the XPS C1s lines for our both nanostructured ZnO thin films.

The last Fig. 6.6. presents the XPS C1s lines, exhibiting a similar symmetry as for the case of XPS O1s spectral lines. Then, after performing a similar Gauss deconvolution procedure, it was found that the RMS fitting parameter was very high and is about 0.98 in both cases with binding energy of ~286 eV and line width of 1.84 eV. Such a coincidence can be attributed to the existence of C-OH surface bonds, which confirms that two kinds of different surface hydroxyl groups have been observed for the XPS O1s (~532.5 eV) and XPS C1s (~286 eV) peaks, which can induce a change in the local surface chemistry.

It should be added at this points that the non-stoichiometry of nanostructured ZnO can affect the surface morphology and resulted in different carbon content on their surface. In the case of the higher gas flow concentration ratio Ar/O_2 (30:3 sccm), where the non-stoichiometry was slightly higher (0.29/0.53) and the porosity was greater, it can be seen that a lower amount of relative C concentration was observed. This is related to the smallest carbon adsorption surface area corresponding directly to the proportion of OH^- groups, since this ZnO sample more easily adsorbs OH- groups on the surface.

The opposite situation occurred for the lower Ar/O_2 gas flow ratio (3:0.3), where grains with dimensions of 100 nm were well-recognized. The relative concentration of C has the highest value (0.27), even at a slightly lower relative oxygen concentration (0.25).

Thanks to the performed studies, it can be concluded that for the potential application of nanostructured ZnO thin film layers for gas detection, those obtained at the highest Ar/O_2 ratio (30:3) are definitely better, as they have a lower level of C impurities. They could be promising candidates for the detection of mainly oxidizing gases, especially in the presence of water vapor H_2O, due to the non-stoichiometry corresponding to the higher concentration of oxygen vacancies, which play a key role as specific adsorption sites for various active oxidizing gases in the gas detection process. Such ZnO nanostructures can be very sensitive especially to toxic gas species containing ambient oxygen, such as nitrogen dioxide (NO_2).

What is crucial, the high concentration of C impurities, including C-OH, causes an undesirable barrier, e.g., for adsorption of toxic gases, especially at the lower operating temperature. Furthermore, this can have a strong influence on the uncontrolled aging effect of the sensor. Therefore, the presented results are very important for the design of gas sensors.

At this point it should be mentioned that all the above described own XPS results have already been published in one of author's paper listed as [40].

As before, at the second stage the XPS studies were performed for the nanostructured ZnO thin films deposited by the DCRMS technology after their additional heating at 700 °C in relation to the independent photocatalytic experiments done within the further studies performed within this work. For the reason described above, for more precise analysis of relative concentration of main specific element the survey spectra at limited binding energy (BE) range (0 ÷ 600 eV) presented in Fig. 6.7. have been taken into account.

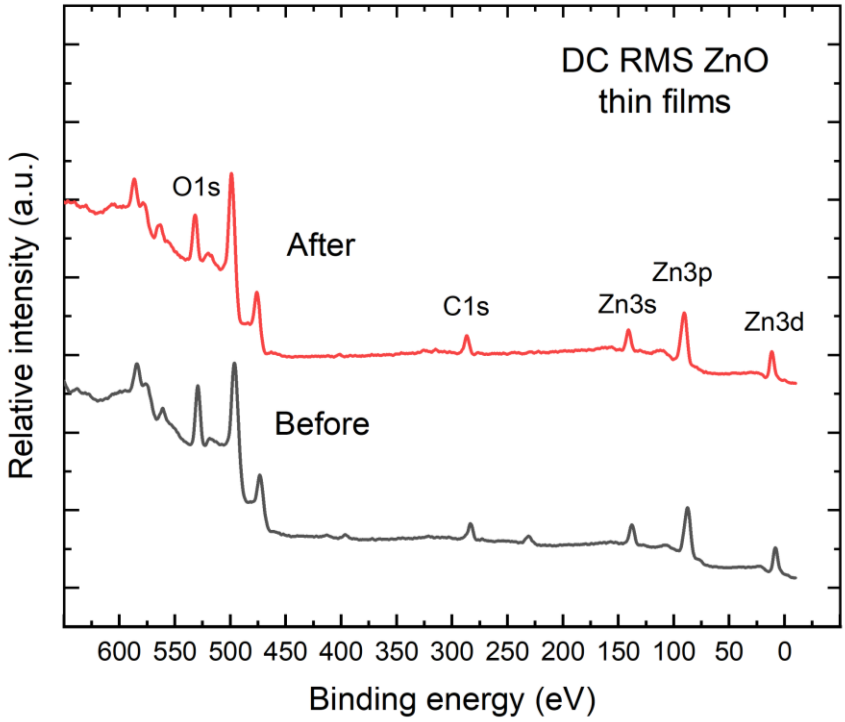

Fig. 6.7. The XPS survey spectra of the nanostructured ZnO thin film after additional heating at 700 °C, before (black) and after (red) 4 cycles of photocatalytic experiments [41].

In this XPS survey spectra, the contribution of main core level XPS lines O1s, Zn3s, Zn3p and Zn3d, as well as the undesired XPS C1s lines related to the undesired C contaminations can be observed. Moreover, as before, apart from the main core level lines, the additional peaks associated with Auger electron emission lines at ~570 eV, ~500 eV and ~470 eV, corresponding to the Zn L3M23M45, Zn L3M45M45, and Zn L2M45M45 electron transitions, respectively, were also observed, which can be omitted in our further data

analysis. Based on the experimental XPS spectra shown in Fig. 6.7., using the above proposed analytical procedure, the relative surface concentration of main elements with respect to all recognized surface atoms have been determined, what was summarized in Table 6.2.

Table 6.2. The relative concentrations of main elements from the subsurface layers of nanostructured ZnO thin films additionally heated at 700 °C before and after photocatalysis [41].

Experimental period	**Relative concentration of the main specific elements**			
	[O]/ ([Zn]+[O]+[C])	**[C]/ ([Zn]+[O]+[C])**	**[O]/ [Zn]**	**[C]/ [Zn]**
before/after	~0.25	~0.20	~1.4	~1.2

As observed in the XPS survey spectra shown in Fig. 6.7. and from the data summarized in Table 6.2, the surface chemistry of above mentioned nanostructured ZnO thin films before and after photocatalytic experiments were similar. It means, that in the surface/subsurface region of the ZnO sample a significant non-stoichiometry was found, which is related to the presence of different surface oxygen atoms combined with surface carbon atoms. It was confirmed by the deconvolution of selected XPS spectral lines $Zn2p_{3/2}$, O1s and C1s, respectively, using the Casa XPS SPECS software.

Fig. 6.8. shows the XPS Zn2p double lines of the nanostructured ZnO thin film before and after the photocatalytic experiments, as well as the XPS $Zn2p_{3/2}$ spectral line for both cases after Gauss fitting deconvolution procedure.

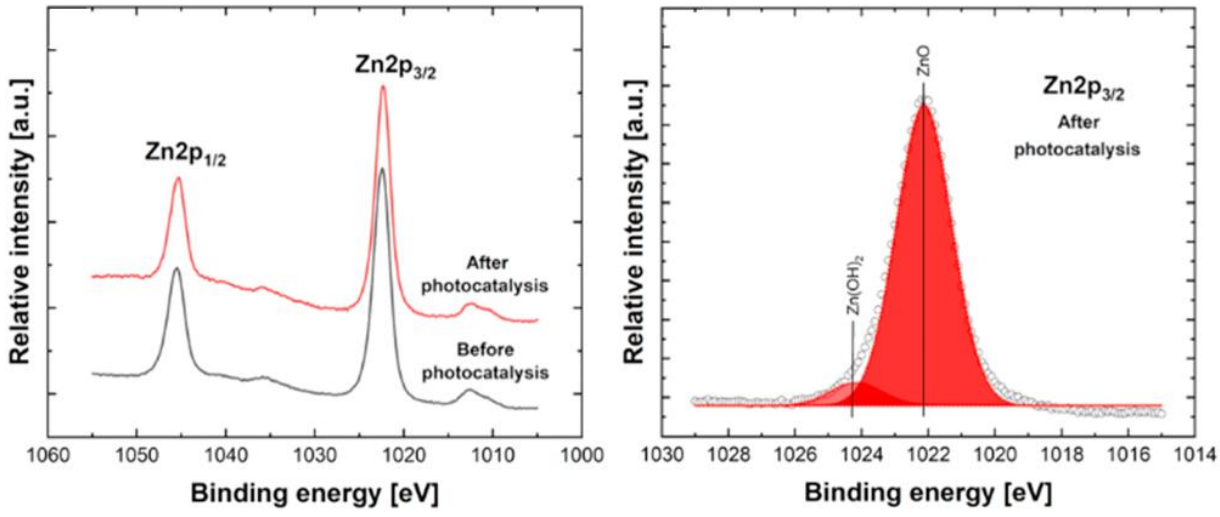

Fig. 6.8. XPS Zn2p double spectral lines of the nanostructured ZnO thin films before (black) and after (red) the photocatalytic experiments (left side) and the XPS $Zn2p_{3/2}$ spectral line for both cases after Gauss fitting deconvolution (right side) [41].

As shown in Fig. 6.8. (left side) the XPS Zn2p double spectral lines of the sample before and after the photocatalytic experiments are broadly, and slightly asymmetrical, having two easy resolved components with the binding energy successively equal to 1045 eV and 1022 eV, what corresponds to the spin orbit splitting of $Zn2p_{1/2}$ and $Zn2p_{3/2}$, with an interval about 23 eV between them, what is proper value according to the reference data [42]. This confirms exactly that the surface Zn atoms occur mainly in the form of Zn^{2-} ion [39].

In turn, as can be seen in the Fig. 6.8.b, after the deconvolution procedure of XPS $Zn2p_{3/2}$ spectral lines, two components, located at ~1022 eV and ~1024 eV, were recognized. A first one being higher can be related to Zn atoms in the ZnO lattice, while the second one is specific to the zinc hydroxide species Zn(OH)2 [40,43], what could be related to the exposure of the sample to natural humidity conditions.

Moreover, in the Fig. 6.9. the XPS spectra of O1s and C1s of nanostructured ZnO thin film before the photocatalytic experiments after Gauss fitting deconvolution procedure.

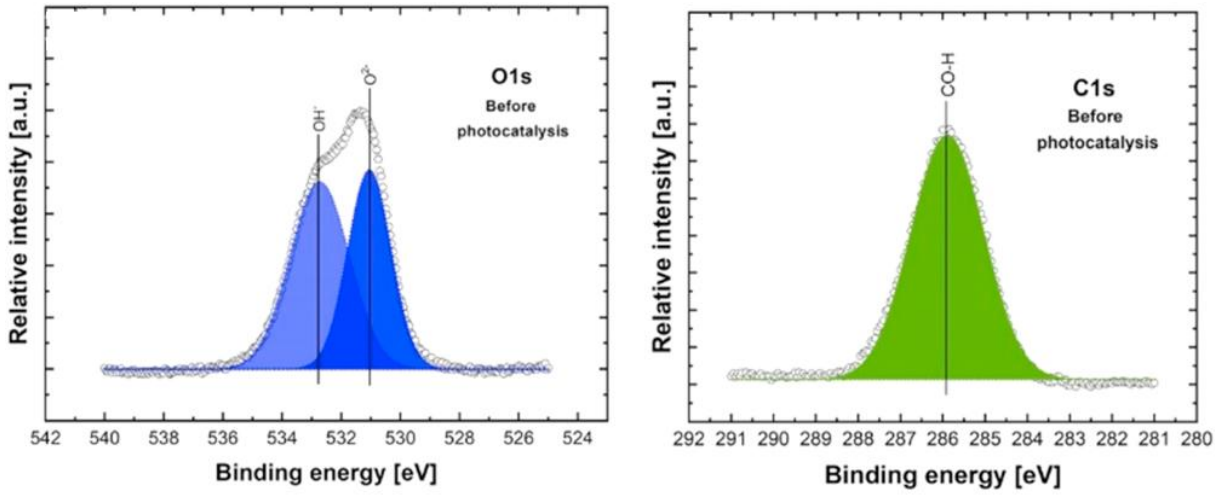

Fig. 6.9. The XPS O1s spectral line (left side) and C1s spectral line (right side) of the nanostructured ZnO thin film before the photocatalytic experiments obtained after Gauss fitting deconvolution [41].

In the left graph two typical oxygen surface bonds at binding energy of 531.1 eV and 532.8 eV, are visible, that can be ascribed to the hydroxyl groups OH^- and the ZnO lattice oxygen ions O_2^-. In turn, in the right graph, a single typical C surface bond at the binding energy 285.8 eV associated with the carbon hydroxyl group C-OH one can observed. The presence of these components is very important for photocatalysis, because the surface oxygen ions O_2^- can take part in the oxidation of adsorbed surface species [44] and surface oxygen hydroxyl groups OH^- could catch holes to form OH radicals. This can also lead to increased molecular oxygen O_2 adsorption, which results in increased production of superoxide ions O_2^- through the reduction by photogenerated electrons [45].

What is crucial, the interesting changes in the oxygen and carbon surface bondings are observed after photocatalysis, which was confirmed by the variation of respective XPS spectral lines shown in Fig. 6.10. As it was already mentioned, the specific oxygen ion form is observed after the photocatalysis, although the oxygen of carboxyl functional groups O-C=O replaces the surface hydroxyl groups OH-, observed before photocatalysis, at the binding energy of 534.1 eV.

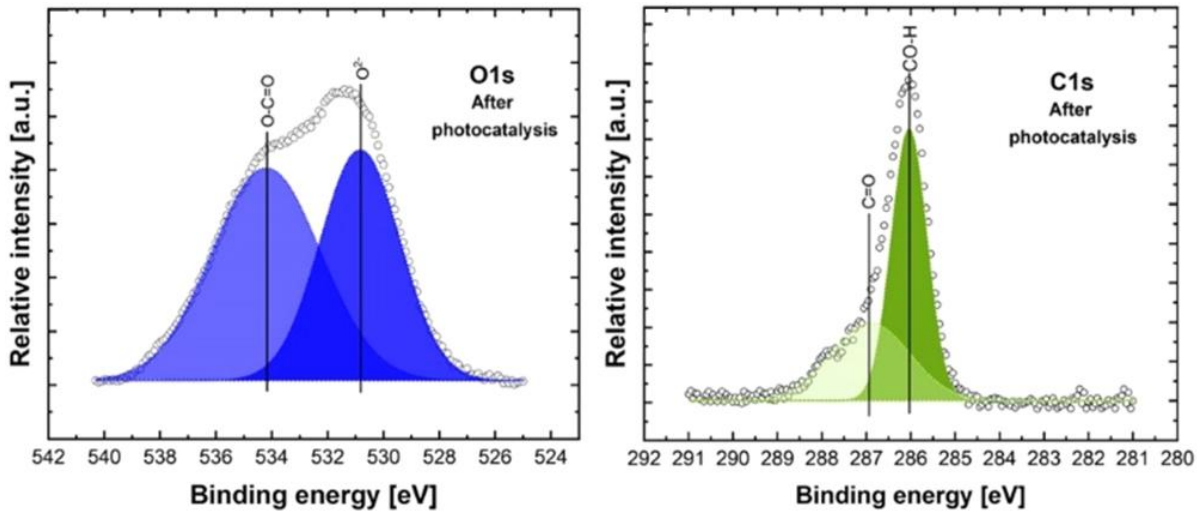

Fig. 6.10. XPS spectral lines of O1s (left side) and C1s (right side) of the nanostructured ZnO thin film after the photocatalytic experiments obtained after Gauss fitting deconvolution procedure [41].

One can observed that for the case of surface C bonds, the C-OH carbon hydroxyl groups, which were present earlier, after photocatalysis can be associated with carbonyl C=O functional groups with a binding energy of 287.2 eV, as shown in Fig. 6.10. (right side). This may suggest that carbonyl and carboxyl groups originate from by-products of photocatalytic degradation of MB [44]. The presence of adsorbed species may cause the appearance of a specific barrier to the intra-particle diffusion of contaminant molecules on the surface of nanostructured porous ZnO thin film, which may result in a decrease in photocatalytic activity in subsequent cycles. Moreover, the morphology of the sample did not change in overall, which is in contrary to the behavior of ZnO nanowires [46,47], nanorods [48–50] and hierarchical ZnO nanostructures [45,51–54].

At this point it should be added that the detailed analysis of the photocatalytic processes at the surface of nanostructured ZnO thin films within the own experiments is presented in one of next chapter.

What is also crucial, the above described own XPS results have already been published in one of author's paper [41].

6.2. VPD ZnO nanowires

As was mentioned above, in this chapter most significant experimental results on the characterization of surface properties of the VPD ZnO nanowires were described, with a special emphasis on their crystallinity and morphology, together with their surface chemistry including purity, non-stoichiometry, and the specific surface bondings.

6.3.1. Crystallinity and surface morphology

As before, for nanostructured DC RMS ZnO thin films, at the first stage a crystallinity and surface morphology of VPD ZnO nanowires deposited at the Ag-covered Si(100) substrate have been studied. However, for these samples the HR SEM method has been used.
Fig. 6.11. shows the SEM images for the VPD ZnO nanowires achieved at two different magnification levels (analytical area).

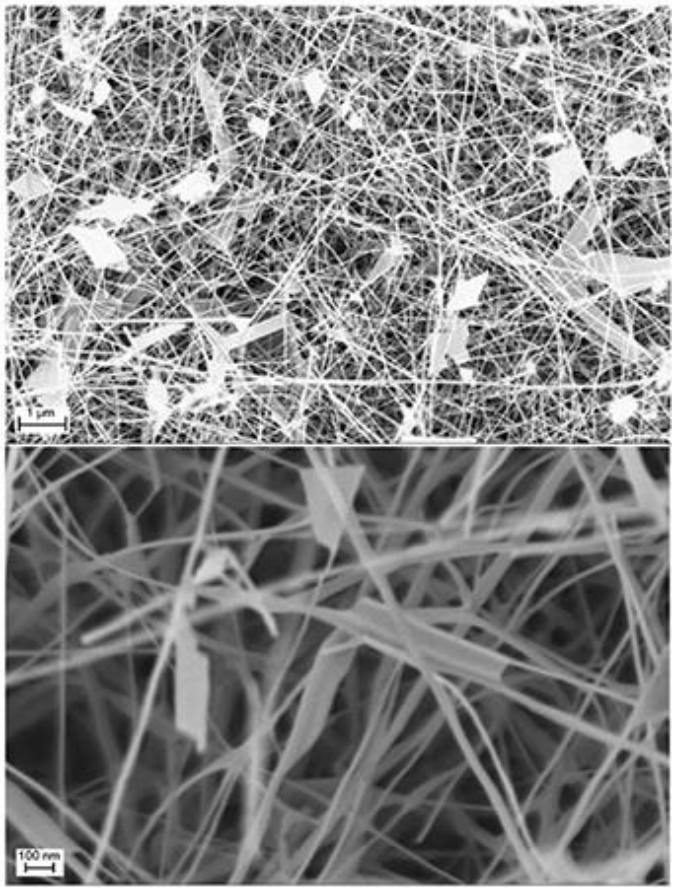

Fig. 6.11. SEM images of VPD ZnO nanowires deposited at the Ag-covered Si(100) substrate at two different magnification levels, and related lateral resolution [21].

One can observe from the images in Fig. 6.11, that Ag-covered Si substrate is almost completely covered by ZnO nanowires (nanoribbons). However, also a small Ag metallic nanograins are observed, which contributes the growth process of ZnO NWs nuclei.

By zooming in more deeply, it is possible to perform the detailed analysis of surface morphology of this sample. It is evident that the ZnO nanowires are mostly isolated and irregular, with varying lengths exceeding one μm and varying in diameter (in the range of 10 ÷ 50 nm). This fact is extremely important, when using this object as the gas sensor material since the gas sensor effect appears in the surface space-charge region of ZnO corresponding to the Debye length, which is of the order of several nm.

6.2.2. Surface chemistry including contaminations

As before for the case of nanostructured ZnO this films, for determination of the surface chemistry of VPD ZnO nanowires deposited on Ag-coated Si substrates, the XPS method has been applied, in combination with the TDS method, respectively.

As before, the survey spectra were obtained before and after the TPD process. However, for the reason explained above, for the deeper analysis of relative concentration of main specific elements, the XPS survey spectra at the limited binding energy (BE) range (0 ÷ 600 eV) presented in Fig. 6.12. have been taken into account.

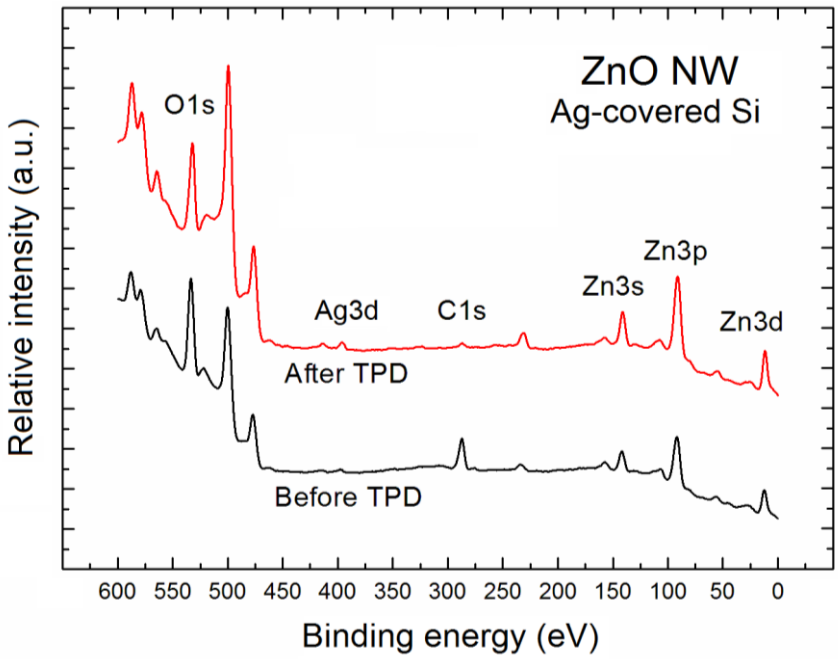

Fig. 6.12. XPS survey spectra of the VPD ZnO nanowires deposited at the Ag-covered Si(100) substrate before (black) and after (red) TPD process [21].

Apart from typical above mentioned Auger Zn LMM and O KLL electron lines (unlabeled - omitted), one can identify the contribution of main XPS Zn2p, O1s, Zn3s, Zn3p and Zn3d spectral lines, corresponding to the main ZnO elements. Additional, also in this case of samples, it was noticed distinct contribution of undesirable carbon contamination at the surface – visible as XPS C1s peaks at binding energy around 286.0 eV.

As before, using the above mentioned data analysis, the relative concentrations of basic elements with respect to all atoms appearing at the ZnO nanowires surface have been determined based on the relative intensities (heights) of the XPS $Zn2p_{3/2}$, O1s, and C1s spectral lines core levels and properly, recently used specific ASF values and additionally corrected for the T(E) of the CHA PHOIBOS 100 energy analyzer. The obtained results are summarized in Table 6.3.

Table 6.3. The relative concentrations of the main elements at the surface of VPD ZnO nanowires deposited on Ag-covered Si(100) substrate before and after TPD process [21].

ZnO NWs	**Relative concentration of the main specific elements**		
	[O]/ ([Zn]+[O]+[C])	**[Zn]/ ([Zn]+[O]+[C])**	**[C]/ ([Zn]+[O]+[C])**
before TPD	0.35	0.32	0.33
after TPD	0.37	0.58	0.05

Based on the obtained results, it can be concluded that before the TPD process, the relative concentrations of main elements at the surface of ZnO nanowires are quite similar (around 0.33). What is even more important the ZnO nanowires exhibits almost stoichiometric form. This information is expected and important, in aspects for their potential application as the gas sensors material, since it is well known that hydrocarbon contaminations are common observed at the surface of such samples exposed to air, similarly to the nanostructured ZnO thin films, during sample transport and handling. However, as discussed earlier, the presence of undesirable C impurities can create a barrier to the gas interaction a the specific surface places, where such potential interaction of adsorbing gases can be expected.

What is crucial, after the TPD process, the relative concentration of main elements at the surface of ZnO nanowires has evidently changed. The most important, which is immediately apparent, is that after the TPD process, the amount of undesirable C contaminants drastically decreased, which was confirmed by the fact that XPS C1s signal reached the level of noise, in contrary to the relative concentration of O with respect to all the surface atoms, which has also strongly changed and reached a value very far from the natural stoichiometry. Perhaps this is due to the existence of specific bond forms on the surface. Therefore, a further more detailed analysis of the evolution of the XPS lines of Zn2p, O1s and C1s has been performed.

At the beginning the XPS Zn2p double lines of the VPD ZnO nanowires before and after the TPD process have been registered, as shown in Fig. 6.13.

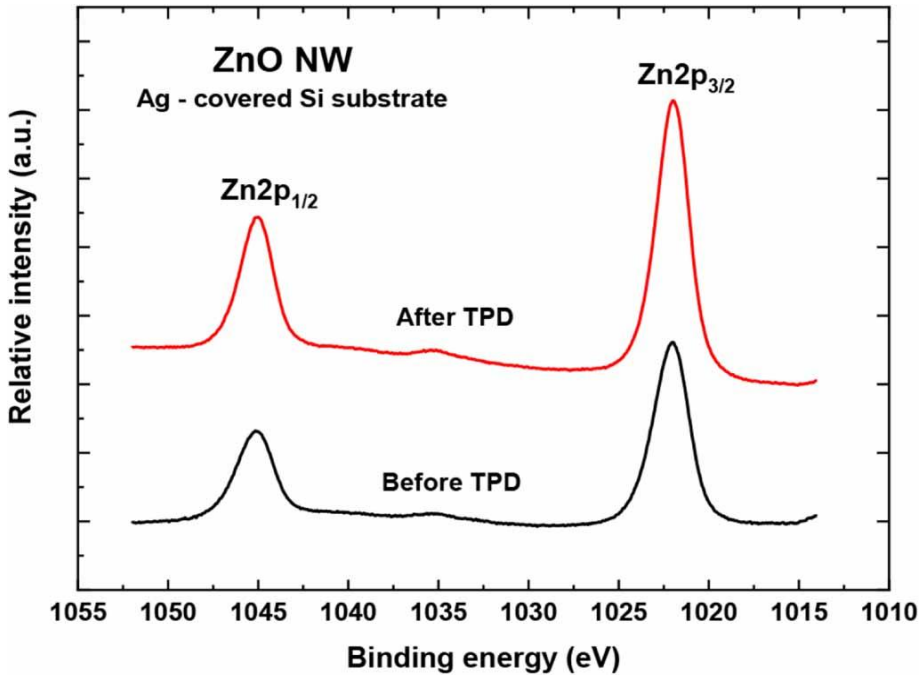

Fig. 6.13. The evolution of XPS Zn2p core level lines for the VPD ZnO nanowires before (black) and after (red) TPD process, respectively [21].

As can be observed in Fig. 6.13., for both cases (before and after TPD process) two components of the XPS Zn2p spectral lines appeared, i.e. a first one at a binding energy of ~1045 eV, which can be attributed to $Zn2p_{1/2}$ component, and the second one at binding energy of ~1022 eV, which is characteristic for the $Zn2p_{3/2}$ component due to the spin orbital splitting effect. What is important an interval between them is at the level of 23 eV, what agrees with the data in the available literature [55–57]. It means that probably Zn surface atoms are mainly present as Zn^{2+} cations, which corresponds to Zn atoms in the ZnO lattice

[55]. However, it can be noticed that the XPS line $Zn2p_{3/2}$ is slightly asymmetric. This is why an additional further analysis of this component was performed using the deconvolution procedure, and the obtained results are presented in Fig. 6.14.

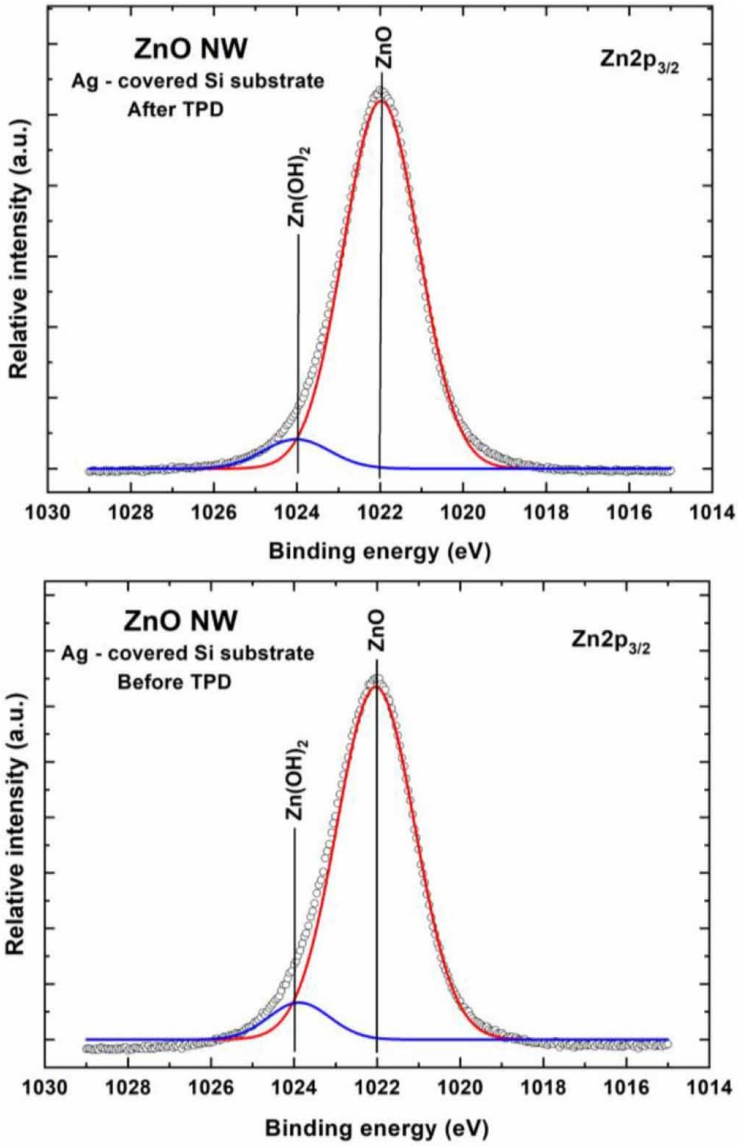

Fig. 6.14. XPS $Zn2p_{3/2}$ lines for the VPD ZnO nanowires before (lower) and after (upper) TPD process respectively, after Gauss fitting deconvolution procedure [21].

As can be noticed in Fig. 6.14. in both cases after the deconvolution procedure the XPS $Zn2p_{3/2}$ spectral contains two components, located at binding energy ~1022 eV and ~1024 eV, respectively, with a very high degree of matching (RMS = 0.995).

A first one being higher in amplitude is related to Zn^{2+} cations in the ZnO lattice, whereas a second one corresponds to the zinc hydroxide $Zn(OH)_2$ species [40,43], which could be related to the exposure of sample to natural humidity conditions, also observed for ZnO nanoparticles by Guo et al. [58] or for ZnO thin films by Armelao et al. [59].

It should be underlined at this point, what is extremely important, that a specific $Zn(OH)_2$ surface bonds at the surface of ZnO nanowires was observed both before and after TPD process. It was also visible in the XPS O1s spectral lines, shown in Fig. 6.15. for the VPD ZnO nanowires before and after TPD process.

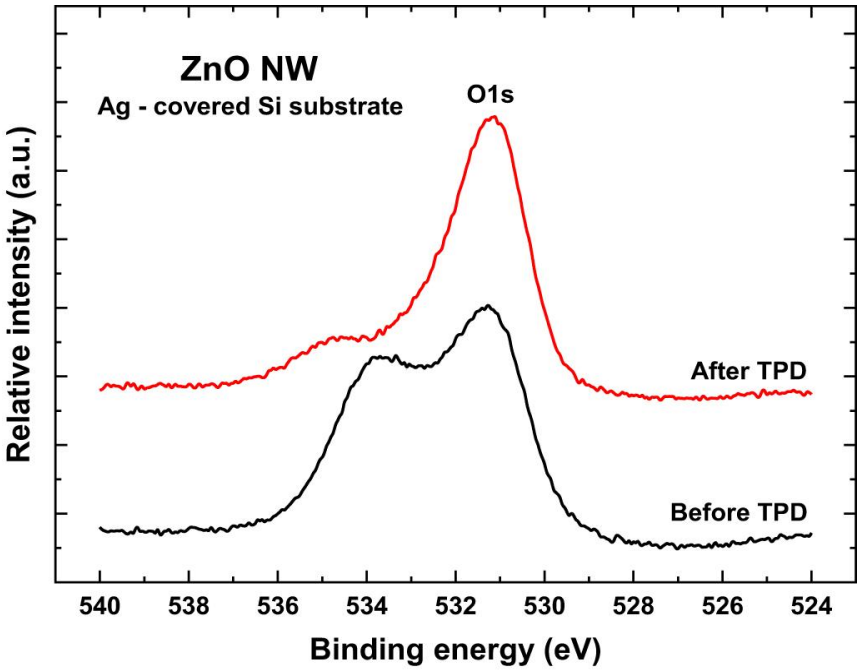

Fig. 6.15. The evolution of XPS O1s core level spectral lines before (black) and after (red) TPD process, respectively [21].

As can be noticed in Fig. 6.15., the XPS O1s lines in both cases show a clear asymmetry with two main parts, which can be directly connected to the potential existence of various forms of oxygen bonds on the surface of VPD ZnO nanowires under investigation.

As before, in order to verify their details, the deconvolution of XPS O1s lines was performed using the Gauss fitting procedure, and the obtained results are shown in Fig. 6.16.

As can be seen from Fig. 6.16., the XPS O1s line before the TPD process contains four components clearly visible at successive binding energies of 533.9 eV and 534.6 eV, respectively.

A first one at binding energy of ~ 531.2 eV can only be attributed to the presence of partially reduced ZnO, such as ZnO_x, directly related to the existence of O_2^- ions caused by oxygen deficiency in the ZnO matrix. Its binding energy has the value about 1 eV higher then normally occurring, what is very significant information, and already is also found in available literature [60,61]. The appearance of defects such as oxygen vacancies and zinc interstitials is related to the fact that oxygen-poor regions appear at the surface of our ZnO nan-

owires, strongly related to their non-stoichiometry. This affects the electrical conductivity, particularly in quasi-single ZnO nanowires with a large surface-to-volume ratio.

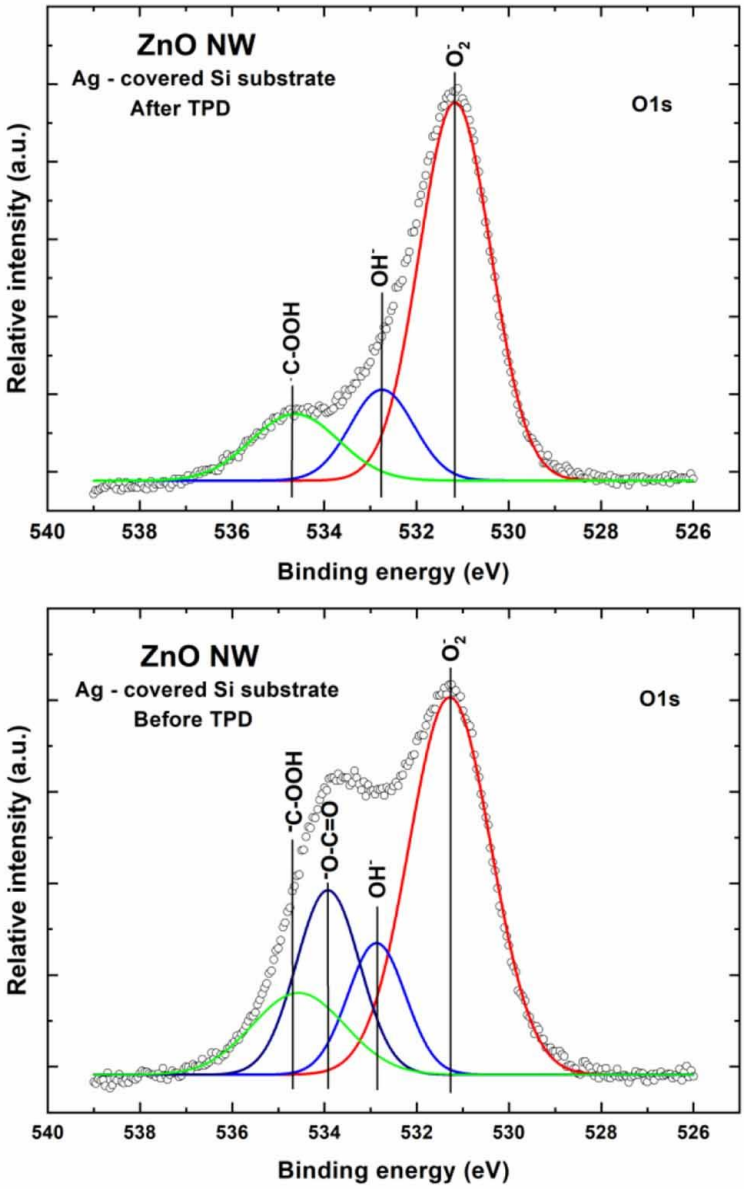

Fig. 6.16. The XPS O1s spectral lines for the ZnO nanowires before (lower) and after (upper) TPD process, respectively, after the Gauss fitting deconvolution procedure [21].

A second one at binding energy of ~532.8 eV, of significantly lower intensity, can be attributed to the presence of loosely bound oxygen at the surface of ZnO nanowires to certain species, such as adsorbed water vapour H_2O or hydroxyl groups, as can also be found in the available literature [59].

A third one at binding energy of ~533.9 eV, higher than the second one, can be ascribed to the additional carbon dioxide O-C=O surface bonds, that can appear at the surface of our ZnO nanowires, whereas a fourth one at binding energy of ~534.6 eV, broad but lowest,

can be attributed to the COOH carboxylic acid groups adsorbed at the surface of our ZnO nanowires.

In turn, after the TPD process, as can also be seen in Fig.6.17, also only three aforementioned XPS O1s spectral line components are clearly visible, at the binding energy of ~531.2 eV, ~532.8 eV and ~534.6 eV, respectively.

What is crucial, a component which was recently attributed to the adventitious carbon dioxide O-C=O (BE ~533.9 eV) disappeared, what can be associated with the desorption of C contaminants from the surface of our ZnO nanowires in the form of gaseous carbon dioxide CO_2 also causing an increase in the relative intensity of component related to the loosely bound oxygen in adsorbed hydroxyl groups.

The obtained results described above related to the specific behavior of XPS O1s spectral line are in good correlation with the behaviour of XPS C1s spectral lines.

Fig. 6.17. shows the subsequent evolution of XPS C1s spectral lines before and after TPD process.

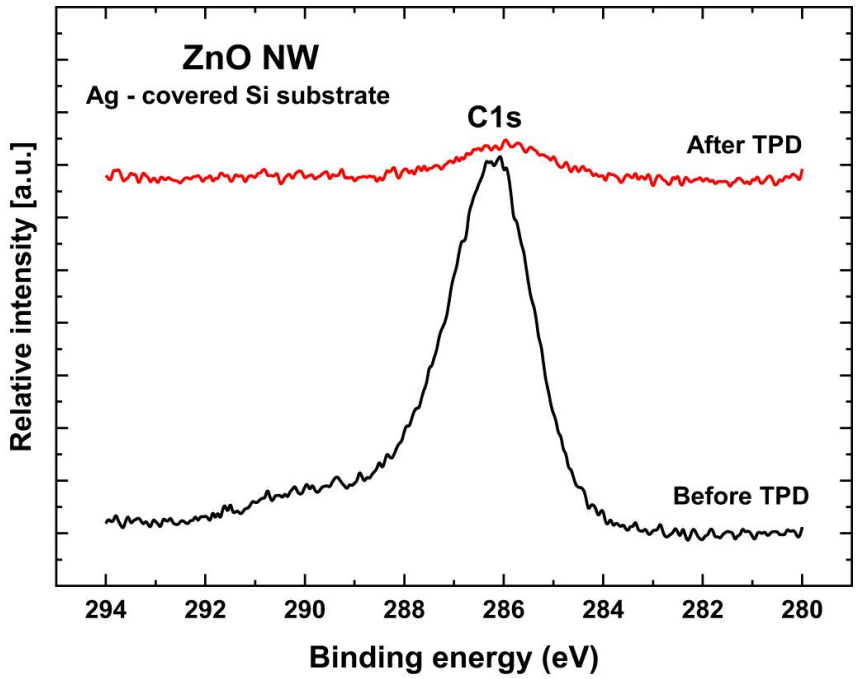

Fig. 6.17. The evolution of XPS C1s core level lines of the ZnO nanowires before (black) and after (red) TPD process, respectively [21].

It has already been repeatedly mentioned that the amount of C pollutants after the TPD process rapidly decreased. As opposed to the XPS O1s line, the XPS C1s line shows only a slight asymmetry before the TPD process, which is certainly related to the existence of selected forms of C surface bonds. It was possible to identify them using Gauss fitting deconvolution, presented in the Fig. 6.18.

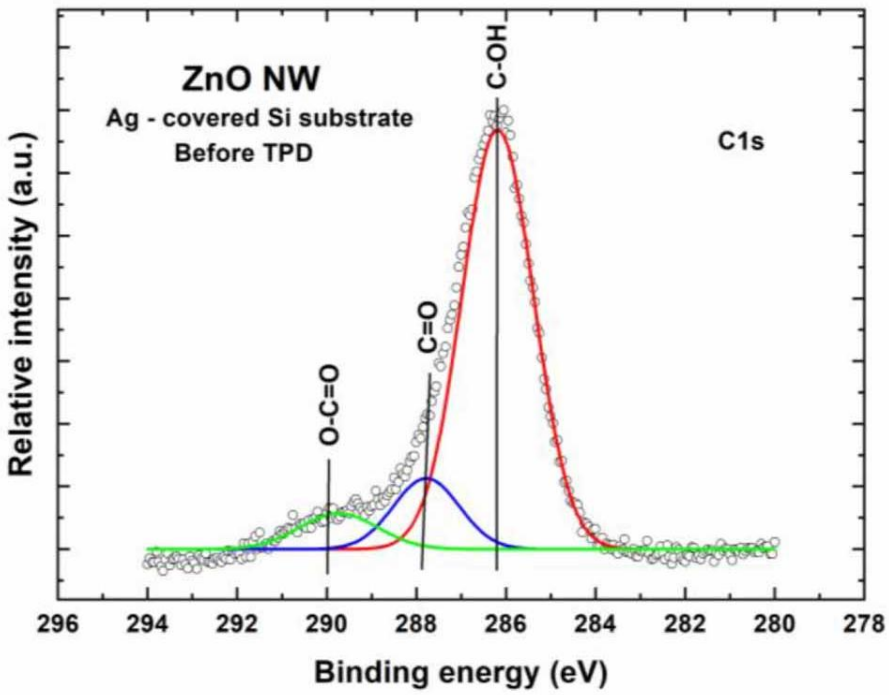

Fig. 6.18. XPS C1s spectral lines of the ZnO nanowires NWs before TPD process [21].

Based on the detailed analysis, it was found that the line fitting parameter was also very high (RMS ~ 0.98) and the XPS C1s spectral line consists of three components at binding energies of 286.1 eV, 287.8 eV, and 288.8 eV, respectively.

A first of the mentioned peaks can be assigned exclusively to C-O bonds, like C-OH, which are commonly seen at the surface of various forms of oxides [62]. This corresponds to the hydroxyl groups adsorbed on the sample surface also recognized in the XPS O1s line.

The two remaining components can be assigned to the different bond forms of carbon oxides bonds, such as C=O and O=C-O. Because after the TPD process the ratio signal-to-noise ratio was at the level of 3, the deconvolution procedure would be questionable. It is certain that only the main peak located at binding energy of 286.1 eV would be visible. As it is connected to the C-OH bonds, it may strongly influence on the local surface chemistry of ZnO nanowires, which is important for further implications for potential sensor applications.

As was mentioned earlier, at the next stage of our experiments the TDS experiment on VPD ZnO nanowires have been performed. Fig. 6.19. shows the TDS spectra of the major residual gases desorbed from the VPD ZnO nanowires after exposure to air, additionally corrected for the probability of ionization of the studied gases detected during the experiments.

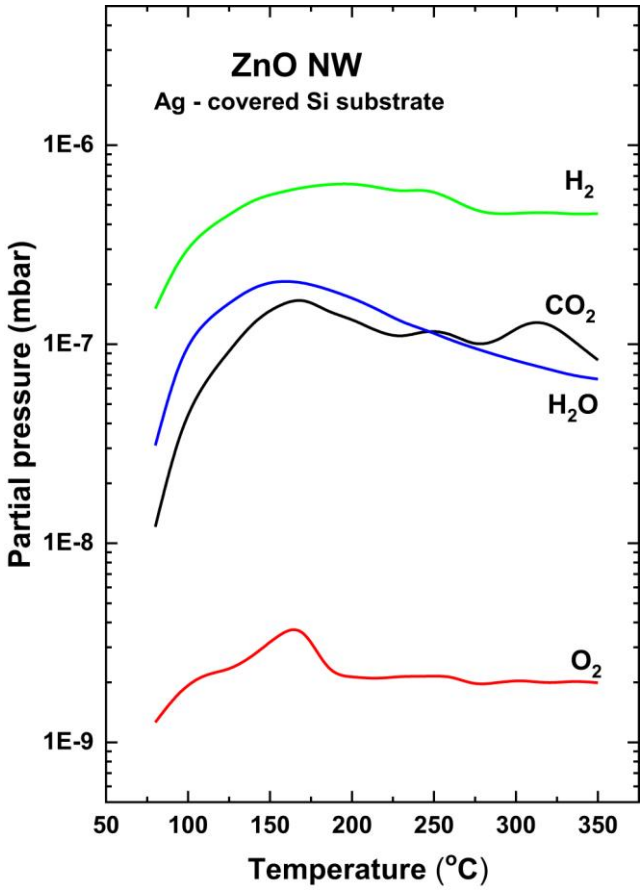

Fig. 6.19. TDS spectra of main residual gases desorbed from ZnO nanowires exposed to air [21].

Based on the analysis of obtained TDS results it was noticed, that during TPD process mainly molecular hydrogen H_2 was desorbed with the highest relative partial pressure of $10^{-6} \div 10^{-7}$ mbar. The H_2 desorption has already started below 100ºC and characterized by almost flat trend in the range 150 ÷ 350 ºC, what is probably caused by high crystallinity of the ZnO nanowires. As far as it is known, such case never occurred in the available literature.

In turn, for the case of molecular oxygen O_2, only small amount desorbed from the sample at the relative pressure of ~ 10^{-9} mbar, starting below 100 ºC and having the highest value (maximum) at ~165 ºC. This may indicate that O_2 remaining in the air atmosphere is only physically adsorbed at the surface of ZnO nanowires. Nevertheless, the relative concentration [O]/[Zn] after the TPD process only slightly decreased.

As water vapour H_2O and carbon dioxide CO_2 are the main gases playing a role in gas sensing effects, their evaluation is particularly important. Similarly as in previous components, water vapour started to desorb below 100 ºC, in the partial pressure range of $10^{-6} \div 10^{-7}$ mbar and has the oscillating tendency with local maxima at 170 ºC, 250 ºC and 320 ºC, respectively, what is characteristic for the presence of various forms of hydroxyl groups at the surface of ZnO nanowires. For the CO_2 desorption effect it has also begun below ~100 ºC,

with the similar partial pressure as for the case of H_2O and has almost constant tendency in the range of 150 ÷ 350 ºC.

Taking into account all the above mentioned information it should be underlined that there are quite good correlations between TDS and XPS experimental results because the desorption of residual gases like H_2O and CO_2 corresponds to the fluctuation of relative concentration of main elements at the surface of ZnO nanowires, related to the at least complete removal of C contamination.

What is crucial, by removing the impurities, the ZnO nanowires surface has become more non-stoichiometric, which has a great influence on potential detection process of adsorption of oxidized gases at the surface of ZnO nanowires, as has been pointed many times above.

Furthermore, by applying the TDS procedure, based on the thermal heating, it was possible to remove almost all of the C impurities, what is a very important finding that can lead to improvements in sensitivity of chemoresistive (conductometric) gas sensors based on ZnO nanowires, as well as their long response/recovery times, respectively, being still a key problem and a limitation of the commonly applied of various forms of the low dimensional ZnO nanostructures.

As before, what is also crucial, the above described own XPS and TDS results have already been published in one of author's paper [21].

What is more, this type of ZnO nanowires have also been used within this work for further experiments on the gas sensor detection of nitrogen dioxide NO_2 using the own gas sensor device based on the surface photovoltage (SPV) effect, what was precisely described in Chapter 8.

Chapter 7.
Application of nanostructured ZnO thin films in photocatalysis and water purification

As it was already mentioned above in this thesis, the selected ZnO nanostructures has found wide application in different fields. The first one, i.e. the nanostructures ZnO thin films, have been used in our studies on photocatalysis combined with the purification of water contaminated with organic compounds, what was in details described in this chapter.

7.1. Fundamentals of photocatalytic (PC) effect

Photocatalysis is a process, belonging to the catalysis area, in which under the influence of light irradiation the specific chemical reaction is improved and accelerated in the presence of a photocatalysts.

In general, there could be distinguished different types of photocatalysis. Mainly, it can be divided into homogeneous and heterogeneous one.

In the first case reactant and photocatalyst are in the same phase. Normally, the photocatalyst is dissolved in the test solution. The second group, by analogy, contains ingredients that are in a different phases.

In each of the above mentioned types, it is possible to additionally distinguish different kinds of chemical reactions that may occur, mainly due to the materials used and the reaction environment.

In this work, the aforementioned heterogeneous method was used to check the photocatalytic activity of the low dimensional ZnO nanostructures under ultraviolet (UV) light by analysis of degradation of methylene blue (MB) in aqueous solution. Additionally, the reusability of this tested ZnO nanostructures was investigated.

In general, the photocatalysis is an advanced oxidation process (AOP), that is based on the formation of the very high rate constants OH• radicals, which then take part in a series of reactions. The whole process occurs with the presence of photocatalyst, which absorbs the light. Fig. 7.1. schematically shows the mechanism of photocatalysis with ZnO particle in the presence of pollutant (P).

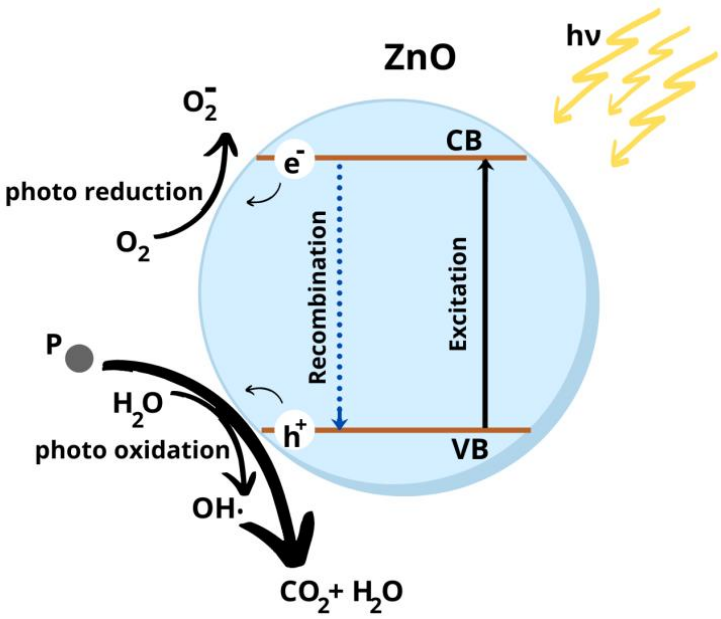

Fig. 7.1. Simplified scheme of photocatalytic mechanism by using ZnO as photocatalitic material.

For the adsorption it is desirable to take the materials, which have the great active surface area and the high porosity. What concerns the semiconductors, unlike the metals, they are characterized by possessing the band gap - the void energy region with no energy states, what is directly described as the difference between the top of valence band (VB) and the bottom of conduction band (CB), respectively.

When the photon having energy greater or equal to the band gap value after its absorption, the respected excitation effect occurs, what is related to the so-called generation (creation) of electron-hole pair, because electron is excited from the VB to the CB, what directly induces in the VB the creation of a positive hole.

The reaction of photoexcitation with the presence of ZnO as photocatalytic material can be written as (7.1, 7.2, 7.3):

$$ZnO \overset{h\nu}{\rightarrow} ZnO(e^- + h^+) \qquad (7.1)$$

$$e^- + O_2 \rightarrow O_2^{\bullet -} \quad \text{(reduction)} \qquad (7.2)$$

$$h^+ + OH^- \rightarrow OH^{\bullet} \quad \text{(oxidation)} \qquad (7.3)$$

After that, at the surface of semiconductor, electrons react with the oxidizers, whereas the holes with reducers, respectively. This leads to reduced products and oxidized products. It is so-called mineralization - transformation (degradation process) of organic pollutants into carbon dioxide CO_2, water and other innocuous inorganic by-products. Those two processes of degradation can be described by following formulas (7.4, 7.5):

$$RH + OH^{\bullet} \rightarrow R^{\bullet} + H_2O \quad \text{(photodegradation)} \quad (7.4)$$

$$h^{+} + R \rightarrow R^{\bullet +} \quad \text{(degradation)} \quad (7.5)$$

7.2. Methodology of photocatalytic (PC) studies

For the photocatalytic experiments the following main components are contained: suitable photoreactor setup with light source, which is kept in a dark conditions, magnetic stirrer, laboratory glassware, spectrophotometric equipment and a solution with a specific dye. The basic components of simplified experimental setup of photocatalysis technique in shown in Fig. 7.2. below.

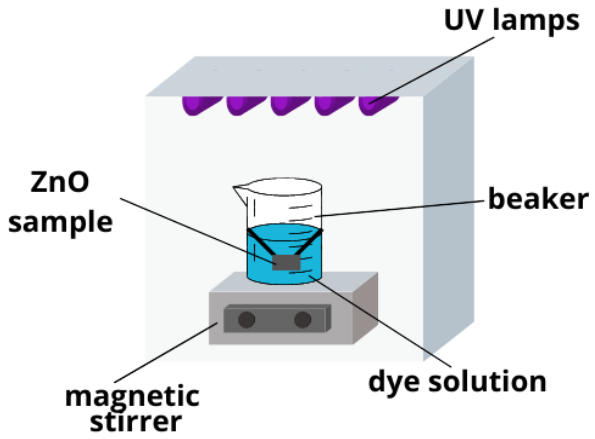

Fig. 7.2. A simplified scheme of the photocatalytic experimental setup.

At the beginning (at the first step), the proper solution with a dye has to be prepared. In that case, as it was already mentioned, methylene blue (MB) dissolved in distilled water had been chosen.

MB is an organic chemical compound, which consists of dark green crystals or crystalline powder, used in different fields e.g. in medicine as an antibacterial product, for cyanide and chad poisoning, to lower the levels of methemoglobin, in veterinary for various diseases occurring in animals, mainly fishes or as an indicator. The chemical structure of MB is presented in Fig. 7.3.

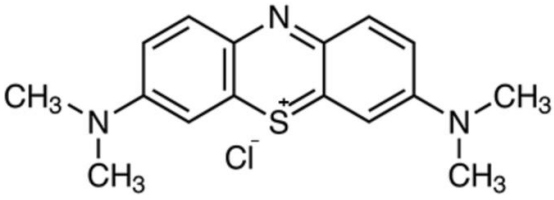

Fig. 7.3. Chemical structure of methylene blue (MB).

It should be noticed at this point, that MB dissolved in water or alcohol takes on deep blue color and cannot be easily removed, what may cause pollution of environment [63,64].

Next, (at the second step), the sample is placed on a special bridge, created from gold, inside the solution and put on magnetic stirrer. Before the whole setup is localized in photoreactor under UV light, the baker is left in the dark conditions for 30 min. This is for reaching the adsorption equilibration of MB at the surface of ZnO thin films. In a properly selected time intervals, a sample is taken from the solution into rectangular quartz cuvette, and then checked by means of double beam UV-Vis spectrophotometer, as shown in Fig. 7.4.

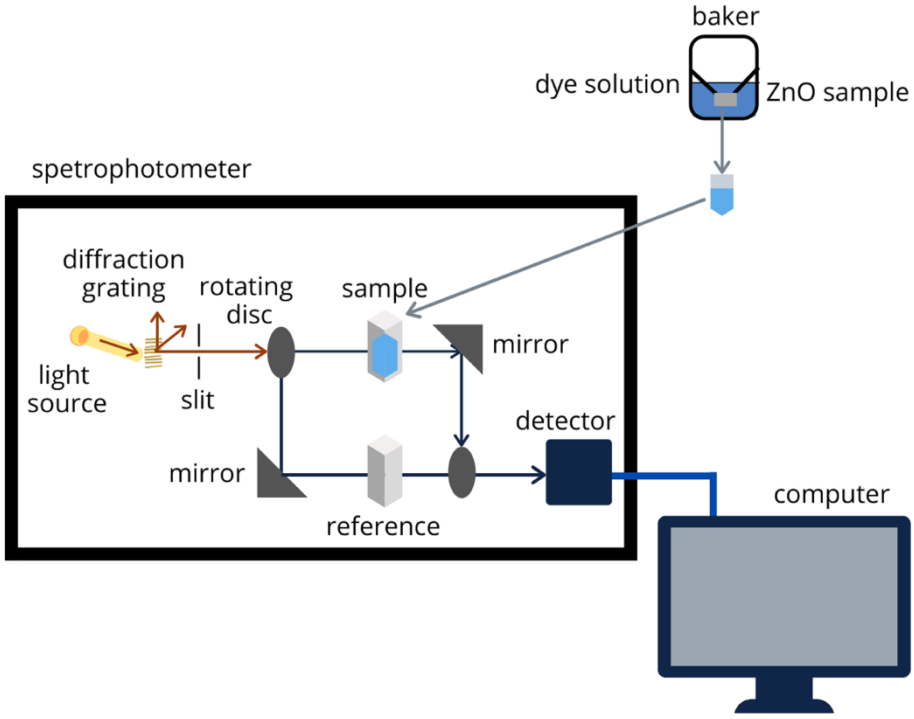

Fig. 7.4. Idea (scheme) of UV-Vis spectrophotometer used in photocatalytic experiments.

In general, in the above mentioned spectrophotometer consists of light sources related to the ultraviolet (UV), visible (Vis) and near infra-red (N-IR) regions, corresponding to the range of wavelength of 200 ÷ 800 nm, and the following two lamps - deuterium and tungsten or halogen one, respectively, are usually used. By the diffraction grating, light is split into the several beams, which are moving in different directions. Only those, which have very narrow range, can go through the slit. At the next step the rotating disc is hit, which consists of three parts. Depends on which of them is affected, there could be distinguished various sections:

- transparent - the light beam goes straight through the sample cell. Then it is reflected through a mirror to the mirrored part of the second rotating disc, from where it is directed to the detector,

- mirrored - the beam is reflected in the next mirror, from where it goes towards the reference cell. It then reaches the other rotating disc and from there it goes to detector,
- black - the light is blocked for a while.

What is crucial, in the detector, a light is converted into the current. Based on that, the intensity of each wavelength is measured and then the absorbance *A* can be calculated using the formula (7.6):

$$A = log_{10} \frac{I_0}{I}, \quad (7.6)$$

where:

I_0 - intensity of light passing through reference cell,

I - intensity of light passing through sample cell;

The respective measurements of concentration carried out by this equipment, based on the Beer-Lambert Law as (7.7),

$$A = \varepsilon \cdot l \cdot c, \quad (7.7)$$

where:

ε - molar absorption coefficient,

l - optical path length,

c - molar concentration;

allows to achieve the respective absorbance spectra for material under investigation.

Abilities

Photocatalysis, usually combined with photolysis) found very wide application in different fields. However, in that case the experiments were focused in one of the most important for human health or even life - water pollution. It is one of the biggest problem nowadays, which has also a major impact on the future. This can be defined as a change in the physical, biological or chemical properties of water, resulting in harmful consequences for living organisms. In order to reduce the pollution process, various methods can be used, such as photocatalysis, based also on the semiconductor nanostructures.

Advantages

As it was also already stated in subchapter 2.4, where potential application of various nanomaterials and nanostructures were presented, there could be distinguished many advantages of photocatalysis, especially, as in presented case, with usage of immobilized nanomaterials. Below, there are listened the main positive aspects:

- no preparation process e.g. mixing and dissolving is needed,
- disposal of persistent organic compounds or microorganisms,
- almost no mass transfer limitations,
- no appearance of secondary pollution,
- easy removal of photocatalyst - no need for filtration or special separation,
- relatively low costs,
- possibility of recovery and reuse of the nanomaterials.

Limitations

The basic limitation of photocatalysis technique are summarized and listened below:

- wide band-gap of the photocatalyst is unfavorable,
- high recombination rate of electron-hole pairs,
- low efficiency of sunlight utilization,
- in the case of homogeneous reactions, it is difficult to separate photocatalyst from the solution and re-use is not possible in many cases,
- inefficient use of visible light, low adsorption capacity of hydrophobic pollutants, even distribution in the water suspension [65].

7.3. Photocatalytic (PC) experiments

7.3.1. Experimental apparatus

The photocatalytic experiments, combined with the photolysis, were performed during my internship at the Technical University in Dresden (Germany).

The MB solution, respectively without and with sample, was irradiated by means of 5 UV lamps (Philips, TL 8W BLB 1FM/10X25CC, $\lambda_{em,max}$ = 365 nm) with a measured irradiance at the level of ~ 1.86 mW/cm^2 at the surface of a sample.

During the experiments, the beaker with solution was put on magnetic stirrer. On a golden wire support, resembling a bridge, the nanostructured ZnO thin film sample horizontally was placed in such a way that it was always submerged in the dye solution. For the observation of the changes in the UV-Vis absorption spectrum of the irradiated solutions over time, spectrophotometric measurements by making use of a Cary 100 UV-Vis Spectrophotometer (Agilent, CA, USA) were carried out. At precisely selected time intervals, 1 ml aliquots were withdrawn and controlled in aforementioned apparatus. The experimental setup is presented in Fig. 7.5. and Fig. 7.6.

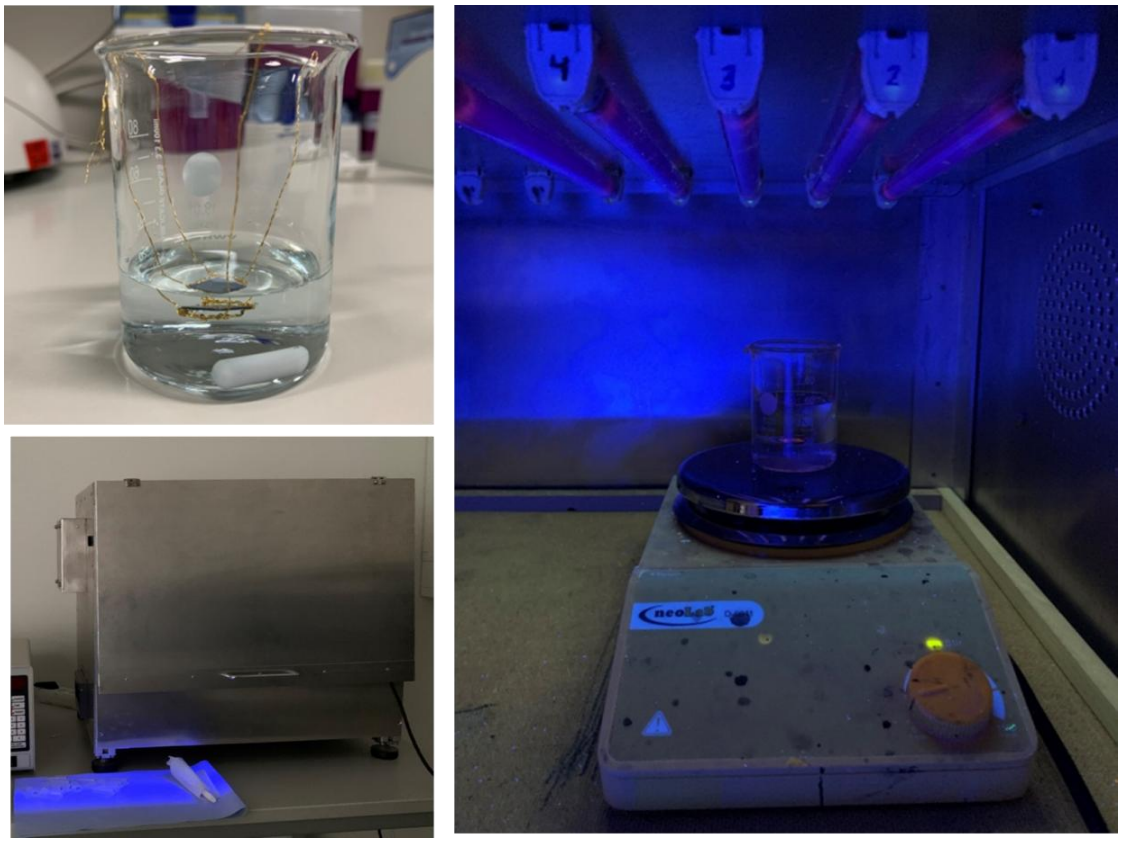

Fig. 7.5. Photolysis and photocatalysis experimental setup - Chair of Material Science and Nanotechnology, Technical University in Dresden, Germany.

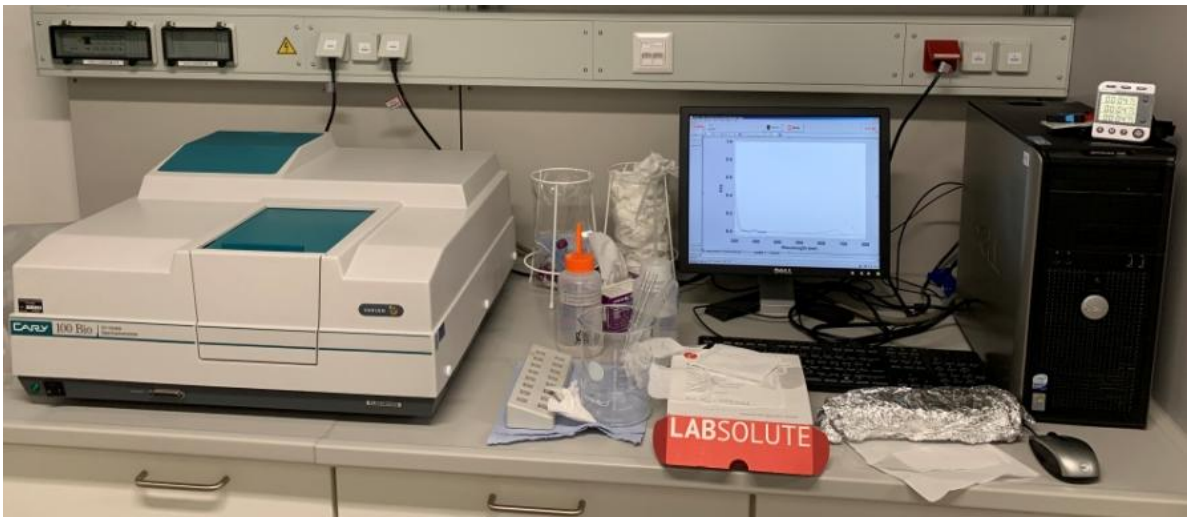

Fig. 7.6. Workstation with UV-Vis Spectrometer, Chair of Material Science and Nanotechnology, Technical University in Dresden, Germany.

What is crucial, before the specific photocatalytic experiments, the nanostructured ZnO thin films mentioned above submerged in the solution was put for 30 min in the dark conditions. The dark absorption goal is to reach the adsorption-desorption equilibrium and in our case when using the nanostructured ZnO thin film it resulted in ~10% over 4 cycles.

At the next step, before the specific photocatalytic experiments, the photolysis studies have been performed, for certainty that MB does not degrade under the exposure to UV light. As supposed, after specified period of time, the amount of a dye was almost identical as at the beginning.

Only after the above mentioned photolysis process, the specific photocatalytic experiments have been performed using the 60 ml aqueous solution (pH = 6.8) of the methylene blue (MB) dye with 0.3 mg/L concentration was used in the sequential time moment: 0 (before the irradiation) and after 5, 10, 20, 30, 50, 70, 90, 120, 150, 180, 210, 240, 270, 300, 330, 360, 390, 420, 450, 480, 510, 540 min, and 1 ml of aliquots were withdrawn and measured using UV-Vis Spectrometer. Then, after each specific experiments were completed, our samples were carefully cleaned with ultrapure water and dried with the compressed air.

7.3.2. Results on photocatalytic studies and their discussion

As was mentioned above, the photocatalysis experiments have been used mainly to check the photocatalytic activity of the low dimensional nanostructured ZnO thin films under ultraviolet (UV) light by analysis of degradation of methylene blue (MB) in aqueous solution. Moreover, the reusability of the above mentioned ZnO nanostructures was investigated.

In the Fig. 7.7. there is presented the UV-Vis spectrum of MB after 4th cycle of experiments with the same ZnO sample.

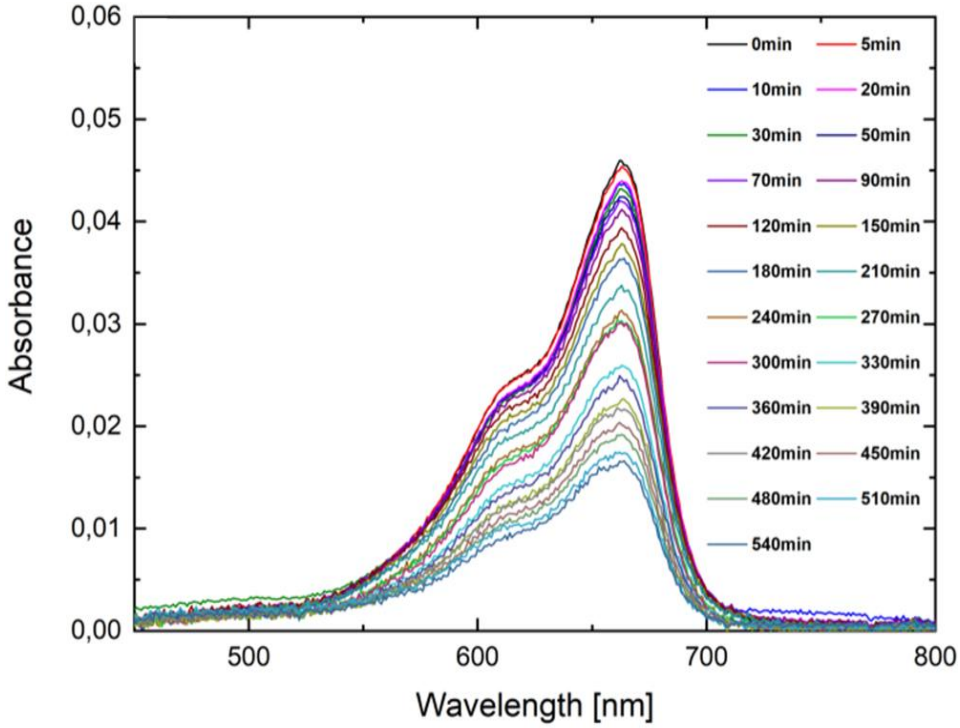

Fig. 7.7. Temporal evolution of the UV-Vis spectrum of MB under UV irradiation after 4th cycle of experiments using the nanostructured ZnO thin film as photocatalytic material [41].

For the calculation of degree of degradation well-known formula was used (7.8):

$$Degree\ of degradation\ (\%) = \frac{c_0 - c_t}{c_0} \cdot 100, \quad (7.8.)$$

where c_o is the MB concentration at t = 0, and c_t - the MB concentration at irradiation time t.

By analyzing the graphs (spectra) shown above, especially the absorption band centered at 663 nm (what is characteristic for MB), it can be seen that degradation of MB dye has occurred and achieved of ~64 % after 540 min.

Since the photolysis process caused practically no change and could be neglected (as confirmed by the respective variation of MB concentration shown in Fig. 7.8., it can be concluded that our nanostructured ZnO thin films were responsible for entire MB degradation.

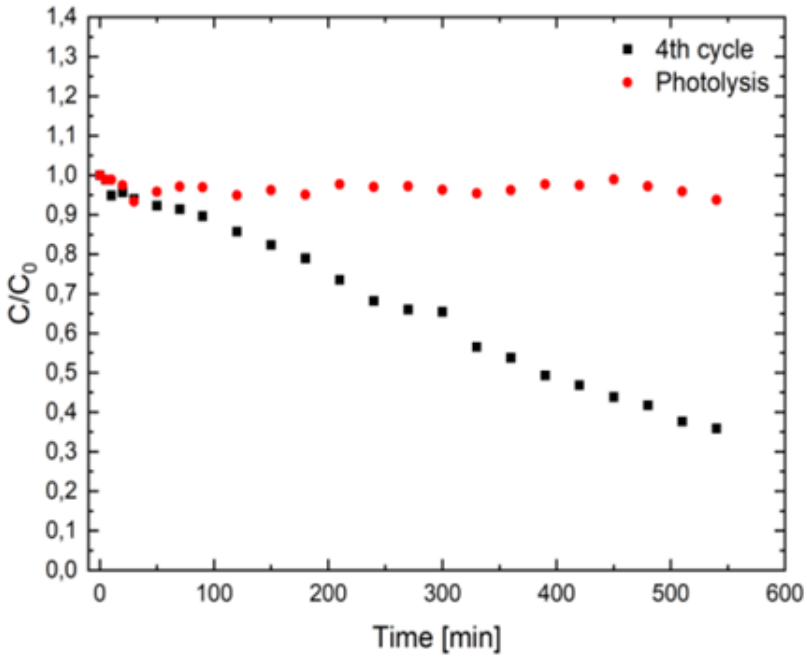

Fig. 7.8. Comparison of the variation of MB concentration over time during photocatalysis and photolysis [41].

As it was already underlined, to verify the reusability of our samples, the photocatalytic experiments were repeated four times. Each time, after every cycle, the sample was carefully washed and dried.

In addition, based on the degradation curves from Fig. 7.8., the kinetics of photocatalytic degradation with the usage of nanostructured ZnO thin film were evaluated.

For the fitting of obtained data, by using the following equation was used (7.9):

$$\sqrt{c_t = c_0 - k \cdot t} \quad (7.9)$$

where c_t is MB molar concentration at time t, c_0 - MB molar concentration at t = 0 and k - the zero-order kinetic constant in $mol \cdot L^{-1} \cdot min^{-1}$.

On the base of obtained fitted data it could be noticed, that the photocatalytic MB degradation at the surface of our nanostructured ZnO thin films one can conclude, that it can be interpreted on the base of pseudo-zero-order kinetic model, which is defined as „surface-reaction limited“ process because in our case, adsorption equilibrium was relatively fast and surface reactions were relatively slow.

Afterwards, the photocatalytic reaction rate constant for the all cycles was evaluated, what was summarized in Table 7.1.

Table 7.1. Photocatalytic rate constant values calculated for 4 cycles of 0.3 mg/L MB solution with usage of nanostructured ZnO thin films [41].

Cycle number	**1st**	**2nd**	**3rd**	**4th**
k [mol·L^{-1}·min^{-1}]	$1.54 \cdot 10^{-9}$	$1.60 \cdot 10^{-9}$	$0.77 \cdot 10^{-9}$	$0.78 \cdot 10^{-9}$

According to the above mentioned behaviour it could be concluded, that the surface of the nanostructured ZnO thin films was saturated with MB molecules and chemical reactions, which take place on the surface, determine its rate [66].

However, what is crucial, it is difficult to analyze our data in comparison to those in the available literature, as the experiments with such kind of sample are quite novel, and it is hard to find the work, which is characterized by similar conditions, operational parameters, etc. Nevertheless, the obtained values of kinetic constants of the pseudo-first order model based on the fitting of obtained experimental data are consistent with those found in the available literature (10^{-3} min^{-1}).

What is also crucial, after four cycles with the same sample it could be observed, that the rate constant decreased by 50%. It can be explained by decrease of the free active sites occupied by unreacted MB and/or by the degradation products or by changes in morphology of the sample. That is why the detailed analysis of surface morphology and chemistry, presented in subchapter 6.2., was performed, as crucial for the interpretation of photocatalytic data.

In Appendix A (Fig. A.1., Fig. A.2. and Fig. A.3.), as a supplementary material, partial results for the remaining studies of the first, second and third cycles are reported. In the presented graphs it can be seen that degradation occurs despite the same material being used several times, and what is more, the level does not change much.

Chapter 8.
Application of ZnO nanowires as material electrode in SPV gas sensor device

As it was already mentioned above in this thesis, the selected ZnO nanostructures has found wide application in different fields. The second one, i.e. the VPD ZnO nanowires have been used in our studies of gas sensing properties as the active electrode in our novel type gas sensor device based on the surface photovoltage effect (SPV) in the nitrogen dioxide NO_2 toxic gas atmosphere, what was in details described in this chapter.

8.1. Fundamentals of surface photovoltage (SPV) effect

In general, the surface photovoltage (SPV) effect appears as a result of variation of the surface potential barrier (band bending) at the semiconductor surface upon illumination of semiconductor surface by the photons of energy equal or higher than band gap E_{bg}, and the separation of subsequently generated electron-holes pairs and their redistribution within the space charge region (SCR) at the semiconductor surface and related variation of the band bending $e \cdot V_s$, [67], what can be directly measured as the additional variation of the contact potential difference (CPD) between the semiconductor surface and the reference metallic electrode. Both effects are schematically shown in Fig. 8.1.

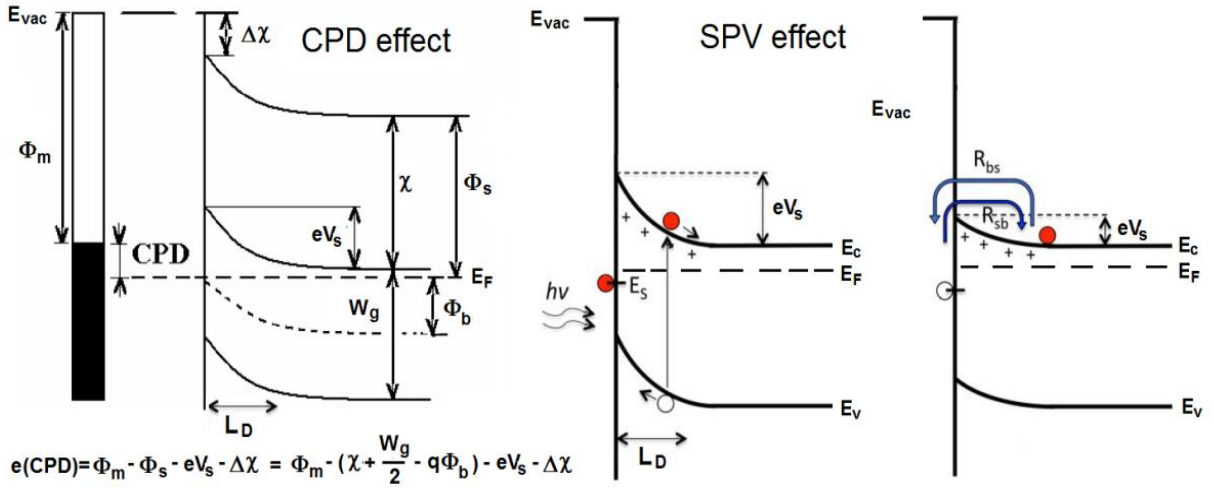

Fig. 8.1. General idea of contact potential difference (CPD) effect and the generation of surface photovoltage (SPV) effect at semiconductor surface after its illumination by photons of specific energy above the band gap.

8.2. Methodology of using of SPV effect in gas sensing studies

There are several methods of measuring the SPV effect as the results of variation of CPD at the semiconductor surface after illumination. However, the most common is based on the reverse Kelvin probe containing the capacitor with active electrode as well as the reference grid electrode on the specific vibrating cantilever after piezoelectric driving by using AC voltage generator. For the gas sensing studies a role of active electrode is playing by the active semiconductor gas sensor material, as shown schematically in Fig. 8.2.

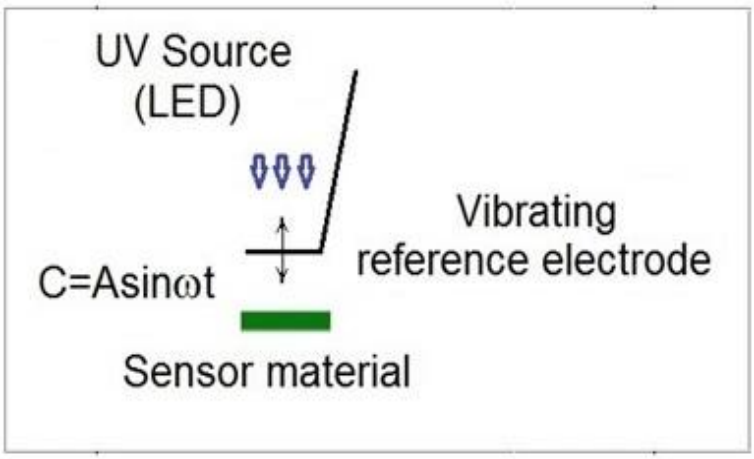

Fig. 8.2. Idea and simplified scheme of the reverse Kelvin probe for the SPV effect using in gas sesning studies.

Abilities

The basic analytical information that can be obtained with SPV method (approach) in the gas sensing studies are available in the forms of specific data – the time dependent gas sensor response/recovery dependences (curves) related to the variation of the band bending $e \cdot V_s$ at the surface of active semiconductor material electrode after its exposure to the specific gas atmosphere, and after its regeneration in the synthetic dry air.

Advantages

The main advantages of SPV method in gas sensing studies are related to the fact that it is the nondestructive method of outstanding surface sensitivity already at room temperature (RT), what is impossible for the typical resistive type MOX gas sensors, together with high versatility, i.e. the measurements can be performed in various media, especially in the various atmospheres including the specific various gases including toxic gases like NO_2.

Limitations

There is no evident limitation in using of SPV effect in gas sensing studies if the SPV signal is commonly measured using the lock-in detection unit, for which the amplitude of variation of SPV signal is at the level of single mV.

8.3. SPV gas sensing experiments

8.3.1. Experimental apparatus and measuring methodology

As was mentioned above, in studies of gas sensing properties of ZnO nanowires an own, original SPV gas sensor device lately elaborated in the laboratory in Department of Cybernetics, Nanotechnology and Data Processing, Silesian University of Technology, Gliwice, Poland, was used [58]. In general, it consists of three main parts, i.e., the SPV gas sensor detection system combined with microcontroller processing system and additionally equipped with gas flow system, what as schematically shown in Fig. 8.3.

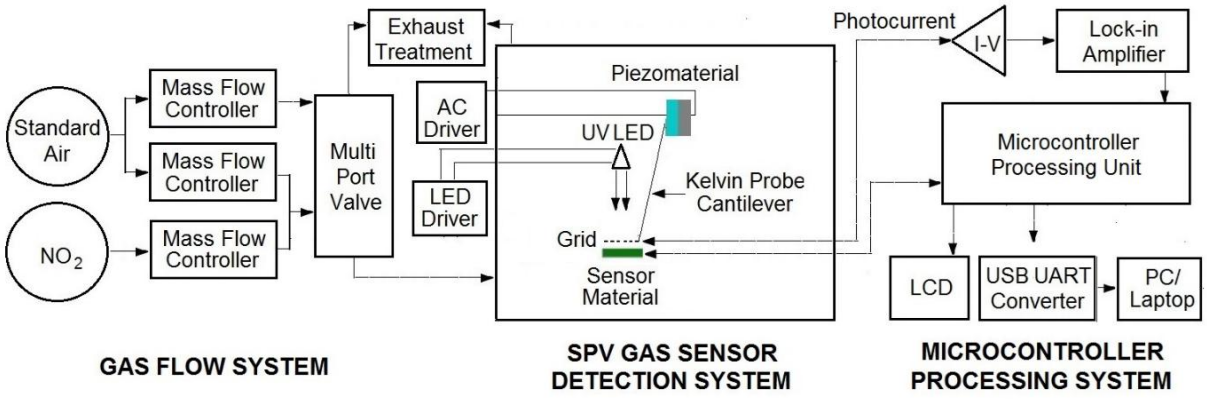

Fig. 8.3. General scheme of the gas sensor device based on the SPV effect [68].

The elaborated SPV gas detection system is based on the reverse Kelvin probe flat type vibrating capacitor system. The capacitor subsystem consists of our ZnO nanowires as a flat gas sensor material playing the role of active electrode, combined with the reference flat Cu metallic grid-type electrode on specific vibrating cantilever after piezoelectric driving using AC voltage generator controlled via the specific, own software.

The alternating SPV signal is measured as the variation of work function of the gas sensor material (with respect to the vibrating reference Cu electrode) as the result of variation of its surface band bending after UV illumination. For this purpose a UV5-400-30 type LED diode (Bivar Company) was used.

For the measuring of variation of SPV signal in the specific gas atmospheres and the data acquisition the microcontroller processing system is used containing the data processing control unit working with, among others, I/V photocurrent converter (amplifier), the respective DAC and ADC converters, and finally the zero self-compensating lock-in amplifier for the reverse Kelvin probe flat vibrating capacitor system. Moreover, microcontroller processing system is equipped with USB to UART converter for laptop connection, enabling the use of our SPV gas sensor system as a mobile device.

As was mentioned above, our SPV gas sensor device is equipped with the gas flow system containing the cylinders of selected toxic gases, including nitrogen dioxide NO_2, being a main toxic gas which has been used in our SPV experiments. Basing on our idea and own designed it was constructed by the MEDSON Company (Paczkowo, Poland). This gas flow dosing system for SPV gas sensing measurements is based on mass flow controllers (MFC) - Brooks SLA5850 model (Brooks Instruments, Hatfek, PA, USA). The generation of gas mixtures with a proper relative concentration of NO_2 in dry synthetic air is possible thanks to the mass flow regulators (MFR) - Brooks SLA5820 model (Brooks Instrument, Hatfek, PA, USA). The pressure regulator allows additionally to stabilize pressure in the measuring system in penultimate step of the process and venting of the excess of produced gas mixture via the additional toxic gas washing bottles (to avoid any undesired escape of NO_2 toxic gas mixture to the surrounding atmosphere). A precise control of the regulators is possible using the specific software MedsonFC.

What is crucial our SPV gas sensor device was more precisely described in in our group' previous publications [68,69]. Its photo is shown in Fig. 8.4.

Fig. 8.4. SPV gas sensor device at the Department of Cybernetics, Nanotechnology and Data Processing, Silesian University of Technology, Gliwice, Poland.

8.3.2. Results of SPV gas sensing studies and their discussion

As was mentioned above, the gas sensing experiments based on the own, original SPV gas sensor device has been mainly used to check the sensing characteristics of the ZnO nanowires in the one of most toxic gas like nitrogen dioxide (NO_2), as it is considered as on the major environmental pollutants caused by industrial development.

What is crucial, already the concentration of NO_2 equal to ~20 ppm is very dangerous to health or even life. Moreover, American Industrial Hygiene Association (AIHA) reports, that the emergency concentration limits are 35 ppm for 5 min and 10 ppm for 60 min of exposure [70]. Even concentrations greater than 1 ppm can lead to serious diseases or exacerbate existing respiratory or cardiovascular systems [71]. Therefore it is very important to detect the NO_2 gas in the lowest possible concentration in the surrounding environment.

What is crucial, having an experience in our previous above mentioned SPV gas sensing studies of the nanostructured ZnO porous thin films [68,69] these gas sensing measurements of ZnO nanowires were carried out at the total gas flow rate of 18 mL/min and the relative concentration of NO_2 in synthetic air in the range of 0.1 ÷ 1 ppm.

Fig. 8.5. shows the time dependent variation of amplitude of the surface photovoltage (SPV) signal - the response (gas on) and recovery (gas out) parts, respectively - of ZnO nanowires after exposure to sequential relative concentration of NO_2 in synthetic air at RT.

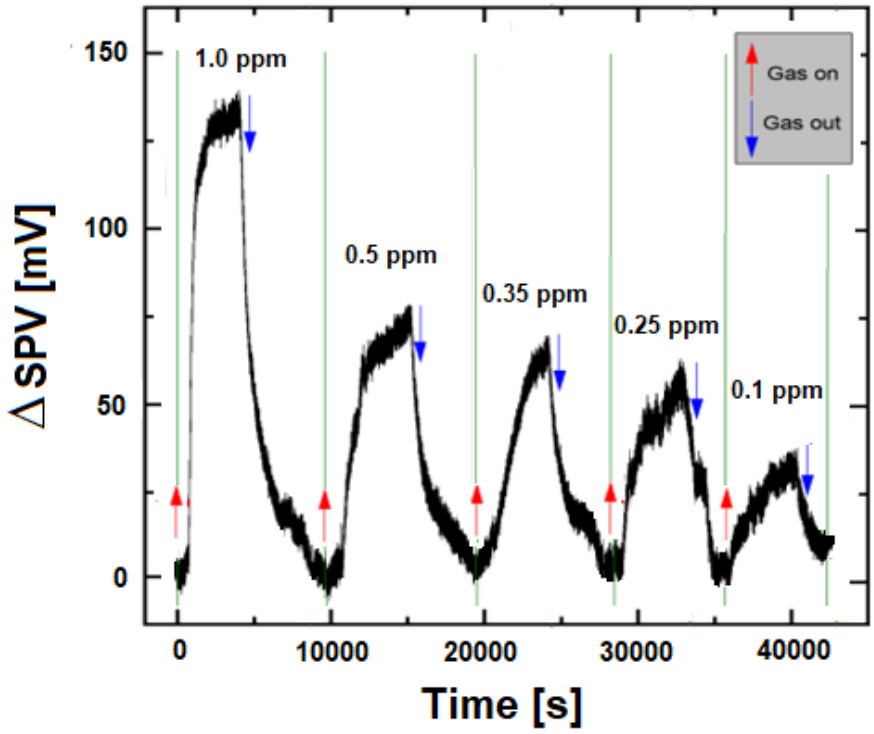

Fig. 8.5. Variation of amplitude of surface photovoltage (SPV) signal for the ZnO nanowires after their exposure to sequential relative concentration of NO_2 in synthetic air. Green areas on the graph indicate the time interval during which a spike in NO_2 concentration occurred [72].

As it can be visible in Fig. 8.5., the decreasing of relative NO_2 concentration in synthetic air results in the lowering SPV signal amplitude, up to reaching the certain extent the saturation effect (stable value of ΔSPV - the slope reached nearly horizontal level). What is crucial, in our studies we took into account that the International Union of Pure and Applied Chemistry, recommends that for a measurement to be reliable, the signal-to-noise ratio (S/N) must be greater than 3 [73]. After analysis of results it was verified, that this criterion has been maintained S/N ratio achieved proper level, in every case. Therefore, for the analysis of response at smallest amount of NO_2, such a ratio was taken into account. It is determined by an equation, which has already found its way into the literature [71,74,75] (8.1):

$$DL = 3 \cdot \frac{rms_{noise}}{slope} = 3 \cdot \frac{\sqrt{\frac{\sum(y_i - y)^2}{N}}}{slope}, \qquad (8.1)$$

where: rms_{noise} is the root mean square deviation between experimental data within baseline region, y_i, and values fitted using polynomial function, y, *slope* is the coefficient in linear

function: $y=ax+b$ used for fitting the gas sensor response of ΔSPV as a function of the gas concentration, and N denotes the number of data points taken into account for fitting - in this case it was equal to 10.

Firstly, based on the respective curves shown in Fig. 8.5., the variation of SPV signal amplitude for the sequential relative concentration of NO_2 in synthetic air was determined, and the obtained results are summarized in the histogram shown in Fig. 8.6.

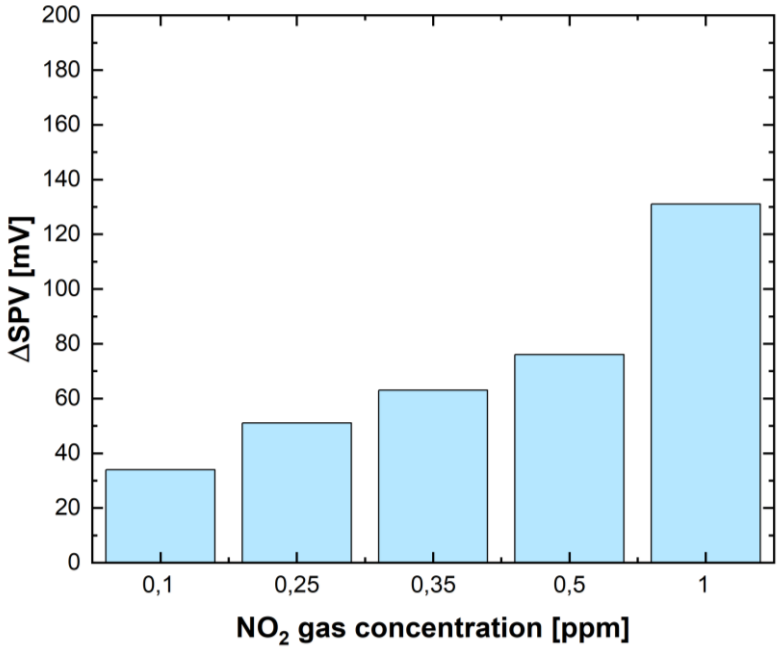

Fig. 8.6. Variation of the SPV amplitude for successive relative NO_2 gas concentrations in synthetic air [72].

As can observed already in Fig. 8.5. and in Fig. 8.6., our SPV gas sensor device using the ZnO nanowires as active electrode exhibits very high sensitivity because for the relative NO_2 gas concentration in synthetic air at the level of 1 ppm the relative variation of SPV amplitude was at the level of ~130 mV (with signal-to-noise ratio (S/N) greater than 30, what was evidently higher with respect to the above mentioned SPV gas sensing response of the nanostructured ZnO porous thin films [68,69] in a similar relative NO_2 gas concentration in synthetic air. Moreover, what is also crucial, for our ZnO nanowires, the relative variation of SPV amplitude was at the level of ~ 34 mV for 0.1 ppm relative NO_2 gas concentration, what was unattainable for the nanostructured ZnO porous thin films [68,69].

Secondly, based also on the respective curves of the variation of SPV signal shown in Fig. 8.5., the gas sensor dynamic parameters for our ZnO nanowires in the relative NO_2 gas concentration in synthetic air in the range of 1 ÷ 0.1 ppm, like the response and recovery time

for each relative NO_2 concentration in synthetic air were determined, which are presented (summarized) in Table 8.1.

Table 8.1. Basic SPV gas sensor dynamic parameters (response and recovery time, respectively) of ZnO nanowires as gas sensor material in our SPV device for the chosen relative concentration of NO_2 in synthetic air [72].

SPV gas sensor dynamic parameters	**NO_2 relative concentration (ppm)**				
	1	**0.5**	**0.35**	**0.25**	**0.1**
Response time (min)	~35.8	~40.0	~41.7	~43.3	~43.3
Recovery time (min)	~63.3	~58.3	~51.7	~50.0	~58.3

Based on the analysis of above mentioned gas sensor dynamics characteristics of ZnO nanowires for various NO_2 gas concentrations, it was possible to notice the certain kinds of phenomena.

What concerns the response time, with the increasing gas amount, it was decreasing, in other words, the sensor reacted fastest with the highest concentration of NO_2. The opposite situation appeared for recovery time, it was decreasing with the decreasing gas amount, i.e. the sensor returned to a stable, initial state in a shorter period of time with the decreasing set quantity of gas. These conclusions and above mentioned correlation can also be observed on the Fig. 8.5., for example, by the steeper rising slope of the graph and the longer time for the return for higher concentrations. It should be also underlined in the case of recovery process – the regeneration of our sensor was realized just by leaving the sample only in synthetic air, without any additional treatments. However it should be admitted, what is also visible in the Fig. 8.5., that it was hard to precisely determine the recovery time for the lowest NO_2 gas concentration (0.1 ppm). But certainly, a very important point is that, despite such a negligible amount of gas, we were able to detect such small amount of gas already in RT conditions, what is not reached by commonly used resistive type gas sensors based on ZnO nanowires.

In order to be able to take a closer look at what the gas detection process looked like and for better visibility, for example, as changes in response and recovery times occurred, enlarged diagrams with a description of when the gas was let in and out, for extreme gas concentrations (1 ppm and 0.1 ppm, respectively) were presented in Fig. 8.7.

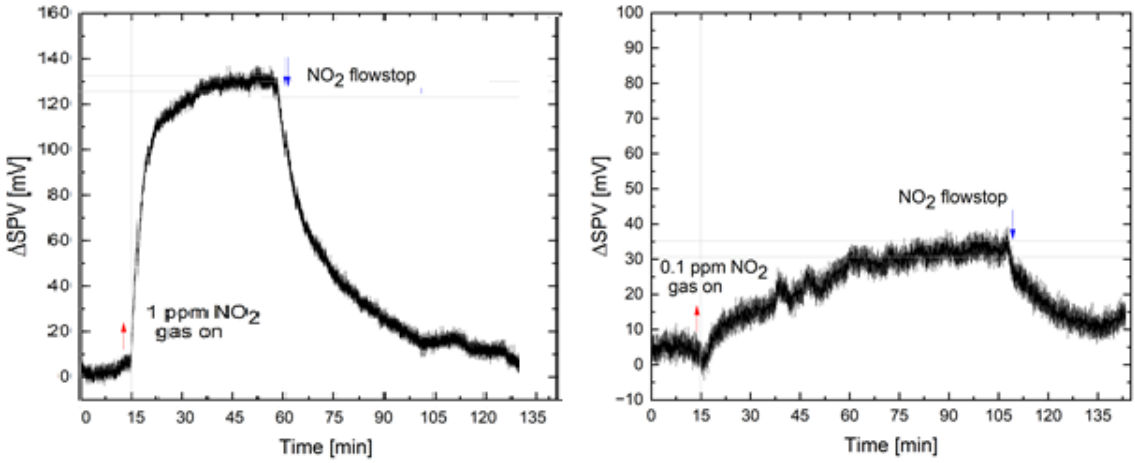

Fig. 8.7. Detailed, magnified graphs of gas detection process based on SPV effect for extreme NO_2 concentrations (0.1 and 1 ppm, respectively) [72].

As it was already mentioned and well highlighted in right graph above, for the 0.1 ppm relative NO_2 concentration it was not so simple to reach a saturation of SPV signal. However, the variation of SPV amplitude is still clearly visible, which demonstrates the ability of chosen ZnO NWs to detect even such small amounts of NO_2 toxic gas.

In the next part of our studies, based on the respective curves shown in Fig. 8.8., the further analysis of variation of SPV amplitude as a function of subsequent various relative NO_2 concentrations in synthetic air was done, and the adequate graph for this evaluation is demonstrated.

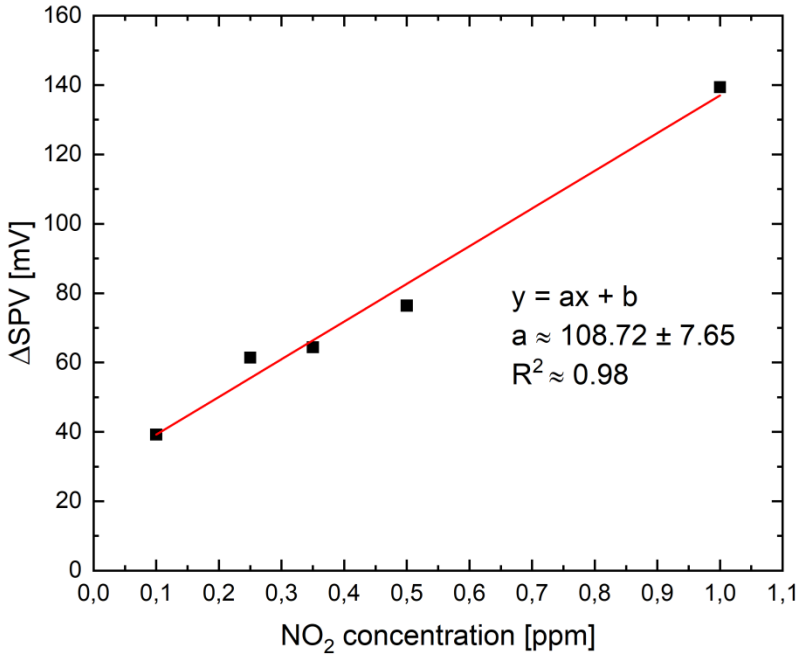

Fig. 8.8. The linear fitting of variation of SPV signal amplitude vs. relative NO_2 gas concentration in synthetic air in the range of 0.1 ÷ 1 ppm [72].

On the graph presented above, the red slope (trend line) corresponds to the coefficient in function $y = ax + b$. It allowed us to notice the relationship between the independent and depended variables, respectively. It is evident that the SPV signal amplitude variation for various relative NO_2 gas concentration in the synthetic air fitted well linear regression, what was additionally confirmed by a high value of *R*-squared parameter. This may suggest, that the sensing process and detected NO_2 toxic gas value could be predictable for chosen ZnO NWs in similar surrounding conditions.

Chapter 9.
Conclusions and final remarks

As was mentioned above, the aim of this PhD thesis was to determine the surface properties of chosen ZnO nanomaterials, related to their various chemistry and morphology, in aspects for the their potential possible further application in environmental engineering using the photocatalysis effect in degradation of methylene blue (MB), as well as in microelectronics using the own SPV based device for toxic gas sensing like NO_2.

In order to verify those assumptions, different types of samples were used, in combination with the selected analytical methods for their surface properties characterization, in aspect for the potential application, as listed above.

This is why the conclusions and final remarks have been separated for the specific information obtained in our subsequent parts of the performed studies.

❖ **Surface properties of nanostructured ZnO thin films**

As a short reminder, based on the comparative AFM, SEM and XPS studies the following basic own information related to their surface properties have been obtained:

- based on the AFM studies it was determined that for the various Ar/O_2 gas flow ratio during the deposition of DCMS nanostructured ZnO thin films, their surface morphology was noticeable different, and what is crucial, for the sample obtained at the gas highest flow ratio (30:3) the high porosity was observed with the well-recognizes grains with dimension of ~ 100 nm, unlike the smaller gas flow ratio (3:0.3),
- in turn, based on XPS studies it was confirmed that the relative concentration of main elements: Zn and O atoms was rather similar for all of the samples, and moreover, for all the samples mentioned above, the presence of C contaminations was detected, probably caused by the temporary exposure of the samples to the air, however in the case of deposition at highest gas flow ratio (Ar/O_2 = 30:3) it was evidently lower,
- in addition, based on independent SEM studies it was confirmed that DCMS nanostructured ZnO thin films after the additional annealing at 700 ºC exhibit the more flat morphology, what was crucial for their potential photocatalytic application,
- finally, based on the additional XPS studies it was confirmed that surface chemistry of above nanostructured ZnO thin films after additional annealing at 700 ºC exhibit a similar surface chemistry, without evident variation after photocatalytic experiments.

❖ **Surface properties of ZnO nanowires**

As a short reminder, based on the comparative SEM, XPS and TDS studies the following basic own information related to their surface properties have been obtained:

- based on the SEM studies it was confirmed that the ZnO nanowires (nanoribbons) are mostly isolated and irregular, with varying lengths exceeding one μm and varying in diameter (in the range of 10 ÷ 50 nm),
- in turn, based on the XPS studies, in combination with the TDS experiments, it was determined, that the relative concentration of main elements: Zn and O atoms at the surface of ZnO nanowires (nanoribbons) is close to the stoichiometry, moreover, it was similar before and after TPD process, with only slightly increased Zn atoms amount,
- finally, based on the XPS studies, in combination with the TDS experiments, it was observed that at the surface of ZnO nanowires (nanoribbons) an additional evident high relative concentration of the undesired C contamination and C-OH species was observed , which have been drastically decreased after TPD process.

❖ **Application of nanostructured ZnO thin films in photocatalysis and water purification**

As a short reminder, the nanostructured ZnO thin films have been used in photocatalysis for the degradation of methylene blue (MB), and the following basic own information have been obtained in this matter:

- using the above mentioned nanostructured ZnO thin films as the photocatalytic material of well-defined and controlled specific surface properties it was confirmed that they can be very effective in the procedure of degradation of methylene blue (MB) in the contaminated water, because after 540 min the degradation level of MB dye was ~ 64 %,
- in addition, based on the performed photocatalytic experiments, one can conclude, that the photocatalytic MB degradation at the surface of our nanostructured ZnO thin films can be interpreted on the base of pseudo-zero-order kinetic model, which is defined as „surface-reaction limited“ process because in our case, adsorption equilibrium was relatively fast and surface reactions were relatively slow.

❖ **Application of ZnO nanowires in SPV gas sensor device for NO_2 detection**

As a short reminder, the ZnO nanowires have been used in our novel, original gas sensor device based on the surface photovoltage (SPV) effect for the detection of NO_2 toxic gas, and the following basic own information have been obtained in this matter:

- using the above mentioned ZnO nanowires of well-defined and controlled specific surface properties it was confirmed that they can be very effective as the active electrode in the gas sensor device (system) based on the surface photovoltage (SPV) effect in

the detection of NO_2 toxic gas, because such system exhibits a quite good gas sensing characteristics, including high sensitivity because the detection level (threshold) was observed at the level of 0.1 ppm (at relative signal to noise to noise (S/N) ratio at the level of 3), as well as the quite good dynamic characteristics (parameters) such as response and recovery time, at the level of several minutes,

- in addition, what is crucial, in relation to the a above, it was obtained already in room temperature conditions, what is absolutely impossible, for the commonly used resistive type gas sensors, even using ZnO nanowires,
- Moreover, having in mind all the above, it should be additionaly underlined, that for our own and original SPV gas sensor device based on the ZnO nanowires the premature ageing effect is solved, what can be treated as an important improvement in the area of gas sensor devices for their and further new potential applications.

Finally, it can be concluded, that all the obtained novel forms of information being a result of the realization of this Doctoral Thesis can be treated as an evident novel contribution to the State-of-the-Art related to the application of novel forms of selected low dimensional ZnO nanostructures for the their potential possible further application in microelectronics and related environmental engineering.

Appendix A

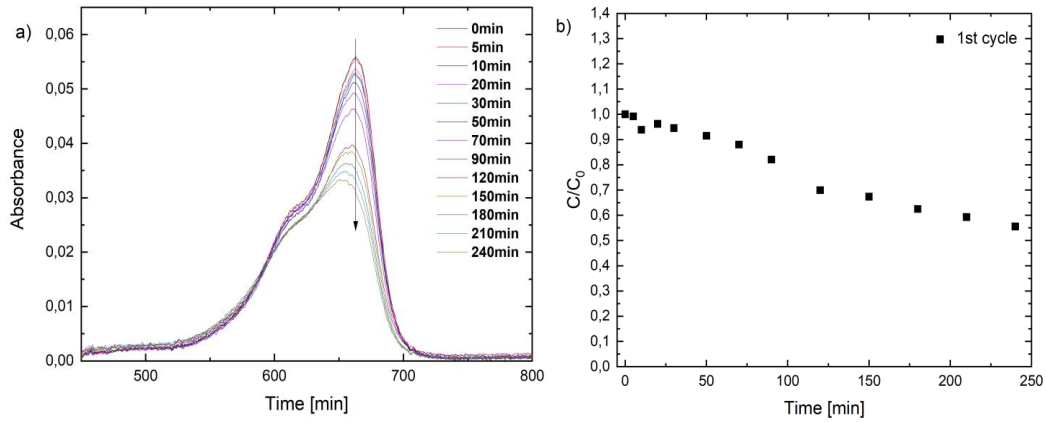

Fig. A.1. Temporal evolution of the UV-Vis spectrum of MB (0.3 mg/L) under UV irradiation using the nanostructured ZnO porous thin films: a) first cycle of experiments, b) variation of MB concentration over time during photocatalytic experiments.

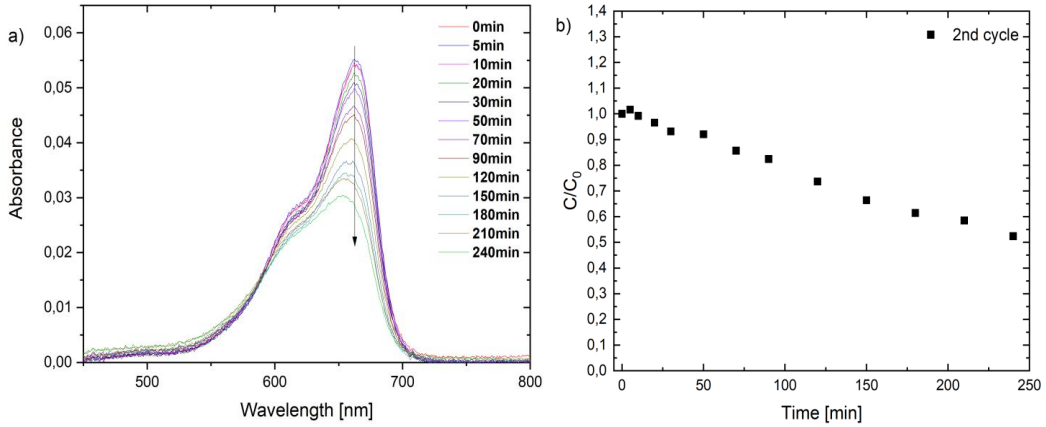

Fig. A.2. Temporal evolution of the UV-Vis spectrum of MB (0.3 mg/L) under UV irradiation using the nanostructured ZnO porous thin films: a) second cycle of experiments, b) variation of MB concentration over time during photocatalytic experiments.

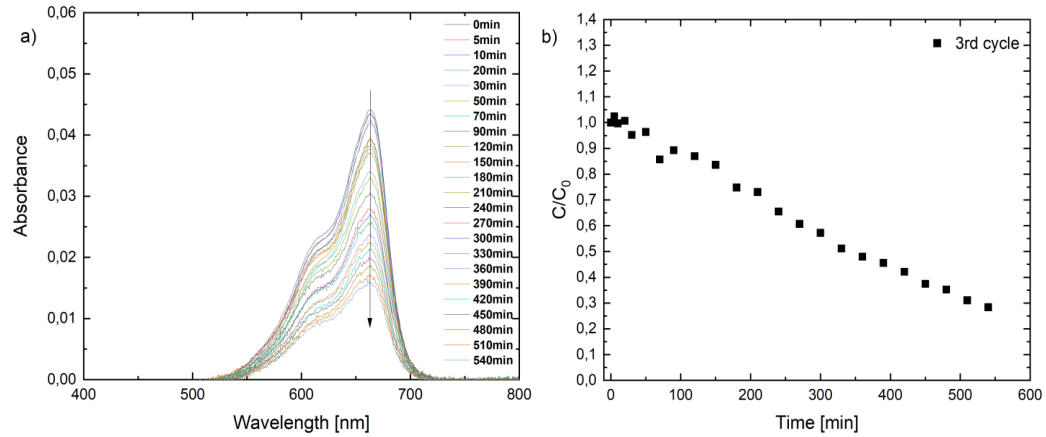

Fig. A.3. Temporal evolution of the UV-Vis spectrum of MB (0.3mg/L) under UV irradiation using the nanostructured ZnO porous thin films: a) third cycle of experiments, b) variation of MB concentration over time during photocatalytic experiments.

Bibliography

[1] G. Pandey, D. Rawtani, Y.K. Agrawal, Aspects of Nanoelectronics in Materials Development, in: Nanoelectron. Mater. Dev., InTech, 2016. https://doi.org/10.5772/64414.

[2] A. Stadler, Transparent Conducting Oxides—An Up-To-Date Overview, Materials (Basel). 5 (2012) 661–683. https://doi.org/10.3390/ma5040661.

[3] C.F. Klingshirn, B.K. Meyer, A. Waag, A. Hoffmann, J. Geurts, Zinc Oxide, Springer Berlin Heidelberg, Berlin, Heidelberg, 2010. https://doi.org/10.1007/978-3-642-10577-7.

[4] N.H. Nickel, E. Terukov, eds., Zinc Oxide — A Material for Micro- and Optoelectronic Applications, Springer Netherlands, Dordrecht, 2005. https://doi.org/10.1007/1-4020-3475-X.

[5] V. Parihar, M. Raja, R. Paulose, A Brief Review of Structural, Electrical and Electrochemical Properties of Zinc Oxide Nanoparticles, Rev. Adv. Mater. Sci. 53 (2018) 119–130. https://doi.org/10.1515/rams-2018-0009.

[6] M.A. Borysiewicz, ZnO as a Functional Material, a Review, Crystals. 9 (2019) 505. https://doi.org/10.3390/cryst9100505.

[7] AZoM, (2011). https://www.azom.com/article.aspx?ArticleID=5818 (accessed May 20, 2022).

[8] H. Morcoc, U. Ozgur, Zinc Oxide: Fundamentals, Materials and Device Technology, Wiley, 2009.

[9] M. Henini, Molecular Beam Epitaxy (MBE): From Research to Mass Production, Second Edition, Elsevier, 2018.

[10] A. Singh, D.H.L. Vishwakarma, An Existential Study on Structural, Optical and Electronic Properties of ZnO Nanoparticles and Nanorods, J. Appl. Phys. 6 (2014) 28–32. https://www.iosrjournals.org/iosr-jap/papers/Vol6-issue2/Version-2/E06222832.pdf.

[11] J. Miao, B. Liu, II–VI semiconductor nanowires, in: Semicond. Nanowires, Elsevier, 2015: pp. 3–28. https://doi.org/10.1016/B978-1-78242-253-2.00001-3.

[12] R.W. Siegel, Nanostructured Materials, in: Adv. Top. Mater. Sci. Eng., Springer US, Boston, MA, 1993: pp. 273–288. https://doi.org/10.1007/978-1-4615-2842-5_17.

[13] Z. Sun, T. Liao, L. Kou, Strategies for designing metal oxide nanostructures, Sci. China Mater. 60 (2017) 1–24. https://doi.org/10.1007/s40843-016-5117-0.

[14] H. Hu, L. Onyebueke, A. Abatan, Characterizing and Modeling Mechanical Properties of Nanocomposites-Review and Evaluation, J. Miner. Mater. Charact. Eng. 09 (2010) 275–319. https://doi.org/10.4236/jmmce.2010.94022.

[15] M. Hughes, What is DC Sputtering, (2016). http://www.semicore.com/images/photos/diagram-dc-magnatron.png (accessed July 8, 2020).

[16] S. Bhattacharya, A.K. Agarwal, N. Chanda, A. Pandey, A.K. Sen, eds., Environmental, Chemical and Medical Sensors, Springer Singapore, Singapore, 2018. https://doi.org/10.1007/978-981-10-7751-7.

[17] L. Otilia Cinteză, M. Antonia Tănase, Multifunctional ZnO Nanoparticle: Based Coatings for Cultural Heritage Preventive Conservation, in: Thin Film., IntechOpen, 2021. https://doi.org/10.5772/intechopen.94070.

[18] A.B. Djurišić, X. Chen, Y.H. Leung, A. Man Ching Ng, ZnO nanostructures: growth, properties and applications, J. Mater. Chem. 22 (2012) 6526. https://doi.org/10.1039/c2jm15548f.

[19] J. Jiang, J. Pi, J. Cai, The Advancing of Zinc Oxide Nanoparticles for Biomedical Applications, Bioinorg. Chem. Appl. 2018 (2018) 1–18. https://doi.org/10.1155/2018/1062562.

[20] J.-H. Ou, C.-J. Wang, F.-H. Ko, The Electrical Enhancement in Dielectric Layer by Gold Nanoparticles Incorporation for Zinc-oxide based Thin Film Transistors, Seoul, 2017.

[21] M. Kwoka, A. Kulis-Kapuscinska, D. Zappa, E. Comini, J. Szuber, Novel insight on the local surface properties of ZnO nanowires, Nanotechnology. 31 (2020) 465705. https://doi.org/10.1088/1361-6528/ab8dec.

[22] E. Dilonardo, M. Penza, M. Alvisi, C. Di Franco, F. Palmisano, L. Torsi, N. Cioffi, Evaluation of gas-sensing properties of ZnO nanostructures electrochemically doped with Au nanophases, Beilstein J. Nanotechnol. 7 (2016) 22–31. https://doi.org/10.3762/bjnano.7.3.

[23] R. Shahbazian-Yassar, Atomic Force Microscopy (AFM), in: Encycl. Tribol., Springer US, Boston, MA, 2013. https://doi.org/10.1007/978-0-387-92897-5_1213.

[24] E. Meyer, H.J. Hug, R. Bennewitz, Scanning Probe Microscopy, Springer Berlin Heidelberg, Berlin, Heidelberg, 2004. https://doi.org/10.1007/978-3-662-09801-1.

[25] S. Morita, F.J. Giessibl, R. Wiesendanger, eds., Noncontact Atomic Force Microscopy, Springer Berlin Heidelberg, Berlin, Heidelberg, 2009. https://doi.org/10.1007/978-3-642-01495-6.

[26] M. Kwoka, Studies of surface properties of L-CVD SnO2 thin films, Silesian University of Technology, Gliwice, 2007.

[27] A. Aliano, G. Cicero, H. Nili, N.G. Green, P. García-Sánchez, A. Ramos, A. Lenshof, T. Laurell, A. Qi, P. Chan, L. Yeo, J. Friend, M. Evander, T. Laurell, A. Lenshof, T. Laurell, J. Chen, J.C. Lacroix, P. Martin, H. Randriamahazaka, W.J.P. Barnes, B.W. Hoogenboom, K. Fukuzawa, H. Hölscher, H. Hölscher, A. Bottos, E. Astanina, L. Primo, F. Bussolino, X. Gao, V.-N. Phan, N.-T. Nguyen, C. Yang, P. Abgrall, F.G. Barth, P. Gurman, Y. Rosen, O. Auciello, C.J. Kähler, C. Cierpka, M. Rossi, B. Bhushan, M.L.B. Palacio, C.L. Dezelah, AFM, Tapping Mode, in: Encycl. Nanotechnol., Springer Netherlands, Dordrecht, 2012. https://doi.org/10.1007/978-90-481-9751-4_33.

[28] NanoAndMore GmbH, The World of Scanning Probes and More, Https://Www.Nanoandmore.Com/Search/Products. (2020).

[29] L. Reimer, Scanning Electron Microscopy, Springer Berlin Heidelberg, Berlin, Heidelberg, 1998. https://doi.org/10.1007/978-3-540-38967-5.

[30] A. Ul-Hamid, A Beginners' Guide to Scanning Electron Microscopy, Springer International Publishing, Cham, 2018. https://doi.org/10.1007/978-3-319-98482-7.

[31] W.E. Spicer, Photoemissive, Photoconductive, and Optical Absorption Studies of Alkali-Antimony Compounds, Phys. Rev. 112 (1958). https://doi.org/10.1103/PhysRev.112.114.

[32] H. Neddermeyer, B. Feuerbacher, B. Fitton und R. F. Willis (Eds.): Photoemission and the Electronic Properties of Surfaces. John Wiley & Sons Ltd, Chichester, New York, Brisbane, Toronto 1978. 540 Seiten, Preis: £ 19,50., Berichte Der Bunsengesellschaft Für Phys. Chemie. 83 (1979). https://doi.org/10.1002/bbpc.19790830215.

[33] M.P. Seah, W.A. Dench, Quantitative electron spectroscopy of surfaces: A standard data base for electron inelastic mean free paths in solids, Surf. Interface Anal. 1 (1979). https://doi.org/10.1002/sia.740010103.

[34] Thermo Fisher Scientific, Angle Resolved XPS, Https://Assets.Thermofisher.Com/TFS-Assets/CAD/Application-Notes/D16069~.Pdf. (2008).

[35] J.H. Scofield, ., J. Electron Spectros. Relat. Phenomena. 8 (1976). https://doi.org/10.1016/0368-2048(76)80015-1.

[36] J. Zhang, ed., PEM Fuel Cell Electrocatalysts and Catalyst Layers, Springer London, London, 2008. https://doi.org/10.1007/978-1-84800-936-3.

[37] J.F. Moulder, W.F. Stickle, P.E. Sobol, K.D. Bomben, Handbook of X-ray Photoelectron

Spectroscopy: AReference Book of Standard Spectra for Identification and Interpretation of XPS Data, Perkin-Elmer Corporation, Physical Electronics Division, Minnesota, 1992.

[38] S. Ogura, K. Fukutani, Thermal Desorption Spectroscopy, in: Compend. Surf. Interface Anal., Springer Singapore, Singapore, 2018. https://doi.org/10.1007/978-981-10-6156-1_116.

[39] M. Masłyk, M.A. Borysiewicz, M. Wzorek, T. Wojciechowski, M. Kwoka, E. Kamińska, Influence of absolute argon and oxygen flow values at a constant ratio on the growth of Zn/ZnO nanostructures obtained by DC reactive magnetron sputtering, Appl. Surf. Sci. 389 (2016) 287–293. https://doi.org/10.1016/j.apsusc.2016.07.098.

[40] M. Kwoka, B. Lyson-Sypien, A. Kulis, M. Maslyk, M. Borysiewicz, E. Kaminska, J. Szuber, Surface Properties of Nanostructured, Porous ZnO Thin Films Prepared by Direct Current Reactive Magnetron Sputtering, Materials (Basel). 11 (2018). https://doi.org/10.3390/ma11010131.

[41] A. Kulis-Kapuscinska, M. Kwoka, M.A. Borysiewicz, T. Wojciechowski, N. Licciardello, M. Sgarzi, G. Cuniberti, Photocatalytic degradation of methylene blue at nanostructured ZnO thin films, Nanotechnology. (2022). https://doi.org/10.1088/1361-6528/aca910.

[42] Y. Lin, H. Hu, Y.H. Hu, Role of ZnO morphology in its reduction and photocatalysis, Appl. Surf. Sci. 502 (2020). https://doi.org/10.1016/j.apsusc.2019.144202.

[43] M.Y. Guo, M.K. Fung, F. Fang, X.Y. Chen, A.M.C. Ng, A.B. Djurišić, W.K. Chan, ZnO and TiO2 1D nanostructures for photocatalytic applications, J. Alloys Compd. 509 (2011). https://doi.org/10.1016/j.jallcom.2010.10.028.

[44] A.M. Ali, E.A.C. Emanuelsson, D.A. Patterson, Conventional versus lattice photocatalysed reactions: Implications of the lattice oxygen participation in the liquid phase photocatalytic oxidation with nanostructured ZnO thin films on reaction products and mechanism at both 254nm and 340nm, Appl. Catal. B Environ. 106 (2011). https://doi.org/10.1016/j.apcatb.2011.05.033.

[45] Y. Hong, C. Tian, B. Jiang, A. Wu, Q. Zhang, G. Tian, H. Fu, Facile synthesis of sheet-like ZnO assembly composed of small ZnO particles for highly efficient photocatalysis, J. Mater. Chem. A. 1 (2013). https://doi.org/10.1039/c3ta10218a.

[46] N. Horzum, M.E. Hilal, T. Isık, Enhanced bactericidal and photocatalytic activities of ZnO nanostructures by changing the cooling route, New J. Chem. 42 (2018). https://doi.org/10.1039/C8NJ01849A.

[47] D. Smazna, S. Shree, O. Polonskyi, S. Lamaka, M. Baum, M. Zheludkevich, F. Faupel, R. Adelung, Y.K. Mishra, Mutual interplay of ZnO micro- and nanowires and methylene blue during cyclic photocatalysis process, J. Environ. Chem. Eng. 7 (2019). https://doi.org/10.1016/j.jece.2019.103016.

[48] A. Azam, S. Babkair, Low-temperature growth of well-aligned zinc oxide nanorod arrays on silicon substrate and their photocatalytic application, Int. J. Nanomedicine. (2014). https://doi.org/10.2147/IJN.S60839.

[49] F. Bourfaa, A. Boutelala, M.S. Aida, N. Attaf, Y.S. Ocak, Influence of Seed Layer Surface Position on Morphology and Photocatalysis Efficiency of ZnO Nanorods and Nanoflowers, J. Nanomater. 2020 (2020). https://doi.org/10.1155/2020/4072351.

[50] A.P.P. da Rosa, R.P. Cavalcante, T.F. da Silva, F. Gozzi, C. Byrne, E. McGlynn, G.A. Casagrande, S.C. de Oliveira, A.M. Junior, Photoelectrocatalytic Degradation of Methylene Blue Using ZnO Nanorods Fabricated on Silicon Substrates, J. Nanosci. Nanotechnol. 20 (2020). https://doi.org/10.1166/jnn.2020.16961.

[51] S. Kuriakose, N. Bhardwaj, J. Singh, B. Satpati, S. Mohapatra, Structural, optical and photocatalytic properties of flower-like ZnO nanostructures prepared by a facile wet chemical method, Beilstein J. Nanotechnol. 4 (2013). https://doi.org/10.3762/bjnano.4.87.

[52] S. Kuriakose, Effects Of Solvent On Structural, Optical And Photocatalytic Properties Of ZnO Nanostructures, Adv. Mater. Lett. 6 (2015). https://doi.org/10.5185/amlett.2015.6088.

[53] M. Lucic Lavcevic, A. Penava, ZnO nanostructured photocatalysts for water treatment applications, Croat. J. Food Sci. Technol. 9 (2017). https://doi.org/10.17508/CJFST.2017.9.2.17.

[54] R.S. Zeferino, J.A.R. Ramón, M.E. de A. Reyes, R.S. González, U. Pal, Large Scale Synthesis of ZnO Nanostructures of Different Morphologies through Solvent-free Mechanochemical Synthesis and their Application in Photocatalytic Dye Degradation, Am. J. Eng. Appl. Sci. 9 (2016). https://doi.org/10.3844/ajeassp.2016.41.52.

[55] C.D. Wagner, W.M. Riggs, L.E. Davis, J.F. Moulder, G.E. Muilenberg, Handbook of X-ray Photoelectron Spectroscopy, Perkin-Elmer: Eden Prairie, MN, 1979.

[56] A. Thompson, D. Vauhan, X-Ray Data Booklet-Center for X-Ray Optics and Advanced Light Source, 2nd ed., Berkeley, California, 2001.

[57] N. Ikeo, Y. Iijima, N. Nimura, M. Sigematsu, T. Tazawa, S. Matsumoto, K. Kojima, Y. Nagasawa, Handbook of X-ray Photoelectron Spectroscopy, JEOL, 1991.

[58] L. Guo, S. Yang, C. Yang, P. Yu, J. Wang, W. Ge, G.K.L. Wong, Highly monodisperse polymer-capped ZnO nanoparticles: Preparation and optical properties, Appl. Phys. Lett. 76 (2000) 2901–2903. https://doi.org/10.1063/1.126511.

[59] L. Armelao, Sol–gel synthesis and characterisation of ZnO-based nanosystems, Thin Solid Films. 394 (2001) 89–95. https://doi.org/10.1016/S0040-6090(01)01158-0.

[60] N. Kaneva, I. Stambolova, V. Blaskov, Y. Dimitriev, A. Bojinova, C. Dushkin, A comparative study on the photocatalytic efficiency of ZnO thin films prepared by spray pyrolysis and sol–gel method, Surf. Coatings Technol. 207 (2012) 5–10. https://doi.org/10.1016/j.surfcoat.2011.10.020.

[61] M. Chen, X. Wang, Y.. Yu, Z.. Pei, X.. Bai, C. Sun, R.. Huang, L.. Wen, X-ray photoelectron spectroscopy and auger electron spectroscopy studies of Al-doped ZnO films, Appl. Surf. Sci. 158 (2000) 134–140. https://doi.org/10.1016/S0169-4332(99)00601-7.

[62] J.F. Moulder, J. Chastain, Handbook of X-ray photoelectron spectroscopy: a reference book of standard spectra for identification and interpretation of XPS data., Perkin-Elmer Corp., UK, 1995.

[63] Ministerstwo Zdrowia, Farmakopea Polska IV, IV, Państwowy Zakład Wydawnictw Lekarskich, Warszawa, 1965.

[64] National Library of Medicine, Https://Chem.Nlm.Nih.Gov/Chemidplus/Rn/61-73-4. (n.d.).

[65] H. Dong, G. Zeng, L. Tang, C. Fan, C. Zhang, X. He, Y. He, An overview on limitations of TiO2-based particles for photocatalytic degradation of organic pollutants and the corresponding countermeasures, Water Res. 79 (2015). https://doi.org/10.1016/j.watres.2015.04.038.

[66] B. Ohtani, Photocatalysis A to Z—What we know and what we do not know in a scientific sense, J. Photochem. Photobiol. C Photochem. Rev. 11 (2010). https://doi.org/10.1016/j.jphotochemrev.2011.02.001.

[67] L. Kronik, Surface photovoltage phenomena: theory, experiment, and applications, Surf. Sci. Rep. 37 (1999) 1–206. https://doi.org/10.1016/S0167-5729(99)00002-3.

[68] M. Kwoka, M. Borysiewicz, P. Tomkiewicz, A. Piotrowska, J. Szuber, A Novel Type Room Temperature Surface Photovoltage Gas Sensor Device, Sensors. 18 (2018) 2919. https://doi.org/10.3390/s18092919.

[69] M. Kwoka, J. Szuber, Studies of NO2 Gas-Sensing Characteristics of a Novel Room-Temperature Surface-Photovoltage Gas Sensor Device, Sensors. 20 (2020) 408.

https://doi.org/10.3390/s20020408.

[70] V.V. Ganbavle, S.I. Inamdar, G.L. Agawane, J.H. Kim, K.Y. Rajpure, Synthesis of fast response, highly sensitive and selective Ni:ZnO based NO 2 sensor, Chem. Eng. J. 286 (2016) 36–47. https://doi.org/10.1016/j.cej.2015.10.052.

[71] B. Lyson-Sypien, M. Kwoka, Rheotaxially Grown and Vacuum Oxidized SnOx Nanolayers for NO2 Sensing Characteristics at ppb Level and Room Temperature, Sensors. 20 (2020) 1323. https://doi.org/10.3390/s20051323.

[72] A. Kulis-Kapuscinska, M. Kwoka, J. Szuber, E. Comini, D. Zappa, SPV gas sensing studies of ZnO nanowires in NO2 atmosphere, (during submission). (2023).

[73] L.A. Currie, Nomenclature in evaluation of analytical methods including detection and quantification capabilities (IUPAC Recommendations 1995), Pure Appl. Chem. 67 (1995) 1699–1723. https://doi.org/10.1351/pac199567101699.

[74] X. Zhu, Y. Guo, H. Ren, C. Gao, Y. Zhou, Enhancing the NO2 gas sensing properties of rGO/SnO2 nanocomposite films by using microporous substrates, Sensors Actuators B Chem. 248 (2017) 560–570. https://doi.org/10.1016/j.snb.2017.04.030.

[75] M.G. Chung, D.H. Kim, H.M. Lee, T. Kim, J.H. Choi, D. kyun Seo, J.-B. Yoo, S.-H. Hong, T.J. Kang, Y.H. Kim, Highly sensitive NO2 gas sensor based on ozone treated graphene, Sensors Actuators B Chem. 166–167 (2012) 172–176. https://doi.org/10.1016/j.snb.2012.02.036.

List of Figures

List of Tables